Title
Studies of Precambrian microfossils and the search for ancient biosignatures on Earth and Mars

Author
Osterhout, Jeffrey Thomas

Publication Date
2021

Peer reviewed|Thesis/dissertation

UNIVERSITY OF CALIFORNIA

Los Angeles

Studies of Precambrian microfossils and the search for ancient biosignatures on Earth and Mars

A dissertation submitted in partial satisfaction of the requirements for the degree Doctor of Philosophy in Geochemistry

by

Jeffrey Thomas Osterhout

2021

ABSTRACT OF THE DISSERTATION

Studies of Precambrian microfossils and the search for

ancient biosignatures on Earth and Mars

by

Jeffrey Thomas Osterhout

Doctor of Philosophy in Geochemistry

University of California, Los Angeles, 2021

Professor James William Schopf, Chair

Fossilized microorganisms (microfossils) preserved within Precambrian sedimentary rocks represent a vital source of evidence for early life on Earth, and studies of such microfossils and the organic matter (kerogen) of which they are typically composed have helped guide the modern search for past life on Mars. Investigations into the morphology, molecular structure, and stable isotopic composition of such cellular kerogenous microfossils have revealed significant insights into the preservation of these ancient biosignatures, including the reconstruction of early microbial metabolisms (e.g., carbon-fixation pathways). However, significant questions remain unresolved, such as the potential consistency of carbon isotope values ($\delta^{13}C_{org}$) preserved between similar morphological fossils from different Precambrian units, the effects of increasing thermal alteration on the $\delta^{13}C_{org}$ of fossil kerogen, and the expected observations for detections of putative kerogen biosignatures on Mars by the *Perseverance* rover. To address these issues, the research presented

here utilizes a combination of optical microscopy, Raman spectroscopy using visible and deep-UV laser wavelengths, and secondary ion mass spectrometry (SIMS) in an effort to characterize the morphological, molecular-structural, and carbon isotopic composition of numerous Precambrian microfossils and associated particulate (detrital) kerogen from a collection of shallow-marine cherts ranging in thermal maturity from unmetamorphosed to greenschist facies, and spanning more than ~1 billion years of Earth history (~400 Ma to ~2,100 Ma). Raman geothermometry calculations were performed on measured Raman spectra of kerogenous microfossils using a relative numerical metric, the Raman Index of Preservation, with values ranging values from ~9.0 to ~1.0, and correlated temperature estimates from ~200–400 °C. SIMS carbon isotope measurements of individual microfossils yielded $\delta^{13}C_{org}$ values ranging from approximately –33‰ to –17‰ between the multiple geologic units investigated, and exhibit a similar trend with higher (i.e., less negative) $\delta^{13}C_{org}$ values associated with the more thermally altered units, though relatively low values were also observed at high temperatures (>350 °C), suggesting that carbon isotopic biosignatures may be potentially retained within cherts that have experienced greenschist facies metamorphism. In addition, deep-UV Raman spectra of such Precambrian microfossils have revealed notable Raman resonance features reflecting changes in the thermal alteration of biogenic kerogen, which may help guide the detection of well-preserved organic matter on the surface of Mars.

The dissertation of Jeffrey Thomas Osterhout is approved.

Kevin D. McKeegan

Tina Treude

David K. Jacobs

Kenneth H. Williford

James William Schopf, Committee Chair

University of California, Los Angeles

2021

Dedication Page

This dissertation is dedicated to my family, the bedrock upon which all of my foundations are built. To my mother Terry, my father Adrian, my brother Marcus, and my sister Megan, this is for you, and would not have been possible without your love, which I will cherish forever.

Table of Contents

List of Figures

List of Tables

List of Acronyms

2-D – Two-dimensional

3-D – Three-dimensional

abcLab – Astrobiogeochemistry Laboratory

BSE – Backscattered electrons

C – Carbon

CCD – Charge-coupled device

CLSM – Confocal laser scanning microscopy

cm – Centimeter(s)

cps – Counts per second

Cs – Cesium

DI – Deionized

DIC – Dissolved inorganic carbon

DNA – Deoxyribonucleic acid

DUV – Deep-ultraviolet

EPS – Extracellular polymeric substances

Fm. – Formation

FTS – Fig Tree Standard

FWHM – Full width at half maximum

g – Gram(s)

Ga – Gigaannum; one billion (10^9) years

GOE – Great Oxidation Event

H – Hydrogen

HCl – Hydrochloric acid

HOPG – Highly oriented (ordered) pyrolytic graphite

IMF – Instrumental mass fractionation

JPL – Jet Propulsion Laboratory

kb – Kilobar(s)

keV – Kiloelectron volt(s)

kg – Kilogram(s)

km – Kilometer(s)

LA-MC-ICPMS – Laser Ablation Inductively Coupled Plasma Mass Spectrometry

m – Meter(s)

Ma – Megaannum; one million (10^6) years

mg – Milligram(s)

μm – Micrometer(s)

mm – Millimeter(s)

mW – Milliwatt(s)

n – Sample size

nA – Nanoampere(s)

NASA – The National Aeronautics and Space Administration

nm – Nanometer(s)

ns – Nanosecond(s)

PAH – Polycyclic aromatic hydrocarbon

Pb – Lead

PDB – Pee Dee Belemnite

PPRG – Preambrian Paleobiology Research Group

Pt – Platinum

RIP – Raman Index of Preservation

RuBisCO – Ribulose-1,5-bisphosphate carboxylase/oxygenase

s – Second(s)

SD – Standard deviation(s)

SE – Standard error(s)

SEM – Scanning electron microscopy

SHERLOC – Scanning Habitable Environments with Raman and Luminescence for Organics and Chemicals

SHRIMP – Sensitive high-resolution ion microprobe

Si – Silicon

SIMS – Secondary ion mass spectrometry

sp. – Species

TOC – Total organic carbon

U – Uranium

UCLA – University of California, Los Angeles

U.S.A. – United States of America

UV – Ultraviolet

VPDB – Vienna Pee Dee Belemnite

W – Watts

Acknowledgements

This work could not have been completed without the help, support, mentorship, and friendship of many other people in my life. For this, I would like to first acknowledge my Ph.D. advisor and mentor, Prof. J. William (Bill) Schopf, the cornerstone of my doctoral degree. I would also like to acknowledge my Ph.D. committee, Prof. Kevin McKeegan, Prof. Tina Treude, and Prof. David Jacobs of UCLA, and Dr. Ken Williford of JPL, all of whom gave their time and support throughout the course of my degree program for which I am deeply grateful. I believe I have become a better scientist and person as a result of my interactions with them, and have learned valuable lessons that will remain with me for the rest of my scientific career and personal life.

I would like to acknowledge those who also helped advise or mentor me over the last several years, or assisted in the technical aspects of this research: Dr. Anatoliy Kudryavtsev, Dr. Ming-Chang Liu, Prof. Mackenzie Day, Dr. Jane Shen-Miller, Dr. Andreas Hertwig, Dr. Elizabeth Bell, Dr. Michael Tuite, Dr. Matthew Koehler, my Masters advisor Prof. Andy Czaja, and Prof. Yanan Shen who hosted my visit to China. I want to thank my past advisors, Prof. Andrew Czaja and Prof. Gregory Retallack, and also the UCLA and Earth, Planetary, and Spaces Sciences staff, especially Lauri Holbrook, Carlene Brown, Richard Fort, Rod O'Connor, Bill Harris, Eric Wessenauer, and Kerry Schutt Nason, as well as my own students and instructors.

Many of my friends, both old and new, have also been essential to the completion of my dissertation and degree. To my girlfriend, Anastasia Fries, who has been the keystone enduring with me over the years and bearing much of the weight of my aspirations. To all of the close friends I have made at UCLA, beyond the scope of this list, but I want to especially acknowledge Sebastian Krause, Amanda Garcia, Emily Hawkins, Mojghan Haghnegahdar, Alex Sedlak, Ashley Schoenfeld, Ashna Aggarwal, Heather Kirkpatrick, Ellen Alexander, Rob Ulrich, David

Yousavich, Jonathan Sneed, Demarcus Robinson, Taylor Dorn, Akash Gupta, Jiarui Liu, Tyler Powell, Abijah Simon, Erik Weidner, Fik Beyene, Sourav Saha, and my friend Andrew Parisi for all they have done and all of the memories we have made. To some of my best friends growing up who believed in me when becoming a Ph.D. was still just a dream, Julian Carrera-Harris, Jose Rodriguez, Arli Rizo, Brian Dogoldogol, and Ryan Bickler. And lastly to my good friends who gave me a place to sleep when I first arrived in Los Angeles and had nowhere to go when my original plan of residence was unsuccessful, thanks to Jesse Scott, Garrett Braun, Cameron Filer, and my roommate Cole Trotter.

Finally, I would like to acknowledge the funding sources for my research and professional organizations with which I have been involved over the years: The Geological Society of America, Paleontological Society, NASA, American Philosophical Society, Geochemical Society, Sigma Xi, as well as the Bruin Geological Society and Sigma Gamma Epsilon.

Vita/Biographical Sketch

Jeffrey Thomas Osterhout

EDUCATION

University of Cincinnati 2016

M.S., Geology

University of Oregon 2012–2013

Post-Bac., Geological Sciences

Oregon State University 2011

B.S., General Science

Minor: Chemistry

PUBLICATIONS

Osterhout, J.T., Czaja, A.D., Bartley, J.K. and Fralick, P.W. (2019). Preservation of carbon isotopes in kerogen from thermally altered Mesoproterozoic lacustrine microbialites. *Canadian Journal of Earth Sciences* **56**(10), 1017–1026.

Schopf, J.W., Kudryavtsev, A.B., **Osterhout, J.T.**, Williford, K.H., Kitajima, K., Valley, J.W. and Sugitani, K. (2017). An anaerobic ~3400 Ma shallow-water microbial consortium: Presumptive evidence of Earth's Paleoarchean anoxic atmosphere. *Precambrian Research* **299**, 309–318.

Czaja, A.D., Beukes, N.J. and **Osterhout, J.T.** (2016). Sulfur-oxidizing bacteria prior to the Great Oxidation Event from the 2.52 Ga Gamohaan Formation of South Africa. *Geology* **44**(12), 983–986.

Retallack, G.J., Gose, B.N. and **Osterhout, J.T.** (2015). Periglacial paleosols and Cryogenian paleoclimate near Adelaide, South Australia. *Precambrian Research* **263**, 1–18.

Retallack, G.J., Marconato, A., **Osterhout, J.T.**, Watts, K.E. and Bindeman, I.N. (2014). Revised Wonoka isotopic anomaly in South Australia and Late Ediacaran mass extinction. *Journal of the Geological Society, London* **171**, 709–722.

SELECTED RESEARCH AWARDS & FUNDING

American Philosophical Society 2019

Lewis & Clark Fund for Exploration and Field Research in Astrobiology

Sigma Xi, The Scientific Research Honor Society 2018

National Grants-in-Aid of Research (GIAR) Award

Sigma Xi, University of Cincinnati Chapter 2016

Grants-in-Aid of Research (GIAR) Award

Department of Geology, University of Cincinnati 2016

Kenneth E. Caster Award (for research in paleobiology)

NASA Astrobiology Institute 2015

Early Career Collaboration Award

Chapter 1

Introduction

The origin of life on Earth and the search for past microbial life on Mars are subjects which have become increasingly connected over time. Today, modern exploration strategies for detecting evidence of ancient life on Mars are based almost entirely on knowledge of Precambrian life (>541 million years ago (Ma)) and of its preservation in Earth's early rock record. However, several challenges remain in the pursuit of such knowledge. Burial, diagenesis, and metamorphism of fossilized biological signatures (biosignatures) may all contribute to the potential geochemical and geothermal alteration of ancient microbial fossils (microfossils) and the metabolic information that might be preserved within their chemical composition. This dissertation research presents paleobiological and geochemical findings from multiple geologic units ranging in age from ~400 Ma to more than 2 billion years ago (Ga), and documents the molecular and carbon isotopic changes associated with increasing thermal alteration of organic-walled microfossils permineralized in several shallow-marine chert deposits.

As prior studies of the Precambrian fossil record have amply illustrated, demonstration of a biological origin (biogenicity) for putative biosignatures typically requires a cascade of mutually reinforcing morphological, geochemical (molecular-structural), and isotopic evidence (Cady et al., 2003; Summons et al., 2011; Oehler and Cady, 2014). Combined with optical microscopy, data obtained from Raman spectroscopy and stable carbon isotope geochemistry can provide interrelated lines of evidence that have proven particularly effective for establishing the existence and diversity of Earth's early biosphere (Schopf et al., 2002; Schopf and Kudryavtsev, 2009; Summons and Hallmann, 2014). Carbon isotope measurements of reduced carbon in sedimentary rocks have therefore been used to document the metabolic characteristics of Precambrian life,

including the evolution of microbial carbon-fixation pathways (e.g., Schidlowski, 2001; Williford et al., 2013; Schopf et al., 2018). Macromolecular carbonaceous matter (kerogen) is appreciably more abundant and less subject to contamination than molecular biomarkers (e.g., soluble fossils such as lipids, proteins, and nucleic acids), and the abundance and isotopic composition of the carbon in such kerogen is less prone to post-depositional alteration than that of its more labile elements (e.g., sulfur or nitrogen) (Oehler et al., 1972; Schidlowski et al., 1983). Like the dispersed particulate organic matter of ancient sediments, cellular Precambrian fossils are composed of kerogen for which secondary ion mass spectrometry (SIMS) provides a means to analyze the carbon isotope composition of individual microscopic specimens (e.g., House et al., 2000; 2013; Williford et al., 2013; Oehler et al., 2017; Schopf et al., 2018). Raman and SIMS together, combined with morphological studies, can provide evidence of the biogenicity and fidelity of geochemical preservation for putative biosignatures – whether of bulk carbonaceous matter or kerogenous microfossils, and whether present in Earth rocks or those to be studied and sampled on the surface of Mars.

Several studies have shown that detectable carbon isotopic differences may exist between fossils of different geologic units and among co-occurring morphologically distinct taxa, interpreted to reflect differences in their depositional and metabolic characteristics, respectively (e.g., Oehler et al., 2009; House et al., 2013; Williford et al., 2013; Schopf et al., 2018), and to ultimately support their biogenicity. To date, however, such studies have encompassed relatively few specimens from a limited number of Precambrian deposits, namely unmetamorphosed shallow-marine cherts in which permineralized microfossils most commonly occur. As a result, the relationship between kerogen biosignature preservation and thermal alteration remains poorly constrained (Des Marais, 2001). Thermal alteration is commonly assumed to increase $\delta^{13}C$ values

(making them "heavier") as a result of kinetic isotope effects associated with hydrocarbon degradation – namely, the preferential breakage of ^{12}C-^{12}C bonds relative to ^{13}C-^{12}C bonds (Hayes et al., 1983; Des Marais, 2001; Galimov, 2006), and carbon isotope values of organic matter ($\delta^{13}C_{org}$) can be increased by over 10‰ from their presumed original value in highly metamorphosed rocks (Schidlowski et al., 1979; 1983). The research presented here aims to add to the growing number of SIMS-analyzed Precambrian microfossils and utilizes a collection of samples from various geologic units spanning more than ~1 billion years of Earth history. Additionally, these studies seek to further expand the range of thermal (i.e., metamorphic) maturities investigated from "unmetamorphosed" up to greenschist facies (~400 °C), and to document the geochemical and isotopic changes resulting from thermal alteration of kerogenous microfossils.

Previous studies that combined Raman and SIMS analyses of individual microfossils have included several Proterozoic (740- to 1,880-Ma) (House et al., 2000; Williford et al., 2013; Peng et al., 2016) and Archean units (3,000 to 3,500 Ma) (Ueno et al., 2001; House et al., 2013; Lepot et al., 2013; Schopf et al., 2018). In general, the Proterozoic units experienced lower levels of thermal alteration and contain relatively better-preserved fossils than those of the Archean. Moreover, the few SIMS data from studies of microfossils have in some instances revealed significant differences between the carbon isotopes in microfossils and the values of background kerogen (e.g., Ueno et al., 2001; House et al., 2013; Schopf et al., 2018), suggesting that the original isotopic composition of most kerogen has been geochemically altered and biosignatures may be lost or masked in bulk measurements (Orphan and House, 2009). Although these studies have yielded significant insight, the data they provide are limited, and the complex relationship between thermal maturity and isotopic preservation remains unsettled.

Raman spectroscopy and imagery are routinely performed on Precambrian microfossils to establish their organic composition, degree of thermal maturity, and to help evaluate potential biogenicity. The carbonaceous composition of such objects can be readily identified by the characteristic kerogen peaks in their Raman spectrum (e.g., Kudryavtsev et al., 2001; Schopf et al., 2002; Schopf et al., 2005). In addition to providing diagnostic molecular information, Raman spectroscopy is also useful for measuring the thermal maturity of ancient organic matter (Beyssac et al., 2002; Pasteris and Wopenka, 2003; Schopf et al., 2005; Kouketsu et al., 2014). Based on analyses of Raman spectra for microfossils from 22 Precambrian units, Schopf et al. (2005) developed a metric for quantifying their relative degree of thermal alteration (the Raman Index of Preservation, RIP) that ranges from less altered kerogen to graphitized specimens.

Raman spectroscopy is also an essential tool for astrobiology (Ellery and Wynn-Williams, 2003; Pasteris and Wopenka, 2003; Foucher et al., 2015) and is included in the Mars 2020 rover payload. The Scanning Habitable Environments with Raman and Luminescence for Organics and Chemicals (SHERLOC) instrument will feature a deep-UV (248.6 nm) Raman spectrometer to map and characterize minerals, organic molecules, and potential biosignatures in Martian rocks and regolith (Beegle et al., 2014; 2015; Beegle and Bhartia, 2016; Abbey et al., 2017). Raman spectra of microbial fossils have been studied in detail for visible laser wavelengths, however, the use of deep-UV has been largely limited to studies of simple organic compounds (Eshelman et al., 2014; Abbey et al., 2017) and, in paleobiology, to studies of Eocene fossil ferns (Czaja et al., 2009) and a few thermally altered Precambrian kerogens (Beegle et al., 2014; Osterhout et al., 2016). These findings have helped stimulate further investigation of ancient organic matter using deep-UV Raman spectroscopy, as kerogen constitutes more than 95% of all organic matter on Earth (Durand, 1980), and is likely to occur in any organic-rich deposits discovered on Mars (Farmer

and Des Marais, 1999). With the Mars 2020 mission now beginning surface operations with the *Perseverance* rover, it is imperative that this biosignature be documented by analyses of organic-walled microscopic fossils on Earth to provide a basis for interpretation of potentially biogenic kerogen detected in sedimentary rocks on Mars. Deep-UV Raman spectra of SIMS-analyzed biogenic microfossils, as measured here, have not yet been reported to my knowledge. Future interpretations regarding the biogenicity and paleoecology of organic microstructures – both those on the early Earth and Mars – will be improved by this research incorporating in situ carbon isotope measurements with those of visible and deep-UV Raman spectra.

This dissertation is presented as three separate manuscripts following an introductory chapter. These manuscripts represent three individual research papers in preparation for submission to scientific journals for publication. The studies presented here include one to be submitted to *Geomicrobiology Journal* dealing with SIMS $\delta^{13}C_{org}$ analyses of morphologically similar fossils from two separate unmetamorphosed Precambrian units (Chapter 2), a second study to be submitted to *Precambrian Research* that describes the relationship between SIMS $\delta^{13}C_{org}$ values and thermal maturity of kerogenous microfossils based on Raman spectroscopy (Chapter 3), and a third study to be submitted to *Astrobiology* characterizing the deep-UV Raman spectra of microfossils through a range of thermally altered cherts. The final chapter of this dissertation serves to summarize the findings and conclusions of this research, and to place the results and interpretations in the broader context of the fields of paleobiology, geochemistry, and astrobiology.

REFERENCES

Cady, S. L., Farmer, J. D., Grotzinger, J. P., Schopf, J. W., & Steele, A. (2003). Morphological biosignatures and the search for life on Mars. *Astrobiology*, *3*(2), 351–368.

Des Marais, D. J. (2001). Isotopic evolution of the biogeochemical carbon cycle during the Precambrian. *Reviews in Mineralogy and Geochemistry*, *43*(1), 555–578.

Farmer, J. D., & Des Marais, D. J. (1999). Exploring for a record of ancient Martian life. *Journal of Geophysical Research E: Planets*, *104*(E11), 26977–26995.

Galimov, E. M. (2006). Isotope organic geochemistry. *Organic Geochemistry*, *37*(10), 1200–126.

Hayes, J. M., Kaplan, I. R., & Wedeking, K. W. (1983). Precambrian organic geochemistry: Preservation of the record. In *Earth's Earliest Biosphere: Its Origin and Evolution* (ed. J. W. Schopf). Princeton University Press, Princeton, NJ, pp. 93–134.

House, C. H., Oehler, D. Z., Sugitani, K., & Mimura, K. (2013). Carbon isotopic analyses of ca. 3.0 Ga microstructures imply planktonic autotrophs inhabited Earth's early oceans. *Geology*, *41*(6), 651–654.

House, C. H., Schopf, J. W., McKeegan, K. D., Coath, C. D., Harrison, T. M., & Stetter, K. O. (2000). Carbon isotopic composition of individual Precambrian microfossils. *Geology*, *28*(8), 707–710.

Lepot, K., Williford, K. H., Ushikubo, T., Sugitani, K., Mimura, K., Spicuzza, M. J., & Valley, J. W. (2013). Texture-specific isotopic compositions in 3.4 Gyr old organic matter support selective preservation in cell-like structures. *Geochimica et Cosmochimica Acta*, *112*, 66– 86.

Oehler, D. Z., & Cady, S. L. (2014). Biogenicity and syngeneity of organic matter in ancient sedimentary rocks: recent advances in the search for evidence of past life. *Challenges*, *5*(2), 260–283.

Oehler, D. Z., Schopf, J. W., & Kvenvolden, K. A. (1972). Carbon isotopic studies of organic matter in Precambrian rocks. *Science*, *175*(4027), 1246–1248.

Oehler, D. Z., Robert, F., Walter, M. R., Sugitani, K., Allwood, A., Meibom, A., Mostefaoui, S., Selo, M., Thomen, A., & Gibson, E. K. (2009). NanoSIMS: Insights to biogenicity and syngeneity of Archaean carbonaceous structures. *Precambrian Research*, *173*(1), 70–78.

Oehler, D. Z., Walsh, M. M., Sugitani, K., Liu, M. C., & House, C. H. (2017). Large and robust lenticular microorganisms on the young Earth. *Precambrian Research*, *296*, 112–119.

Orphan, V. J., & House, C. H. (2009). Geobiological investigations using secondary ion mass spectrometry: microanalysis of extant and paleo-microbial processes. *Geobiology*, *7*(3), 360–372.

Peng, X., Guo, Z., House, C. H., Chen, S., & Ta, K. (2016). SIMS and NanoSIMS analyses of well-preserved microfossils imply oxygen-producing photosynthesis in the Mesoproterozoic anoxic ocean. *Chemical Geology*, *441*, 24–34.

Schidlowski, M. (2001). Carbon isotopes as biogeochemical recorders of life over 3.8 Ga of Earth history: evolution of a concept. *Precambrian Research*, *106*(1), 117–134.

Schidlowski, M., Appel, P. W. U., Eichmann, R., & Junge, C. E. (1979). Carbon isotope geochemistry of the $3.7x10^9$ yr. old Isua sediments, West Greenland: Implications for the Archaean carbon and oxygen cycles. *Geochimica et Cosmochimica Acta*, *43*, 189–199.

Schidlowski, M., Hayes, J. M., & Kaplan, I. R. (1983). Isotopic inferences of ancient biochemistries-Carbon, sulfur, hydrogen, and nitrogen. In *The Proterozoic Biosphere: A Multidisciplinary Study* (eds. J. W. Schopf and C. Klein). Cambridge University Press, Cambridge, pp. 149–186.

Schopf, J. W., & Kudryavtsev, A. B. (2009). Confocal laser scanning microscopy and Raman imagery of ancient microscopic fossils. *Precambrian Research*, *173*(1), 39–49.

Schopf, J. W., Kudryavtsev, A. B., Agresti, D. G., Wdowiak, T. J., & Czaja, A. D. (2002). Laser–Raman imagery of Earth's earliest fossils. *Nature*, *416*(6876), 73–76.

Schopf, J. W., Kitajima, K., Spicuzza, M. J., Kudryavtsev, A. B., & Valley, J. W. (2018). SIMS analyses of the oldest known assemblage of microfossils document their taxon-correlated carbon isotope compositions. *Proceedings of the National Academy of Sciences*, *115*(1), 53–58.

Summons, R. E., & Hallman, C. (2014). Organic geochemical signatures of early life on Earth. *Treatise on Geochemistry*, 33–46.

Summons, R. E., Amend, J. P., Bish, D., Buick, R., Cody, G. D., Des Marais, D. J., Dromart, G., Eigenbrode, J. L., Knoll, A. H., & Sumner, D. Y. (2011). Preservation of Martian organic and environmental records: final report of the Mars Biosignature Working Group. *Astrobiology*, *11*(2), 157–181.

Ueno, Y., Isozaki, Y., Yurimoto, H., & Maruyama, S. (2001). Carbon isotopic signatures of individual Archean microfossils (?) from Western Australia. *International Geology Review*, *43*(3), 196–212.

Williford, K. H., Ushikubo, T., Schopf, J. W., Lepot, K., Kitajima, K., & Valley, J. W. (2013). Preservation and detection of microstructural and taxonomic correlations in the carbon isotopic compositions of individual Precambrian microfossils. *Geochimica et Cosmochimica Acta*, *104*, 165–182.

Chapter 2

Carbon isotopes of Proterozoic filamentous microfossils: SIMS analyses of ancient cyanobacteria from two disparate shallow-marine cherts

Jeffrey T. Osterhout, J. William Schopf, Kenneth H. Williford, Kevin D. McKeegan, Anatoliy B. Kudryavtsev, Ming-Chang Liu

1. INTRODUCTION

Prior to the ~541 Ma "Cambrian explosion of animal life," microorganisms prevalent in aquatic environments dominated Earth's biosphere. Such Precambrian, mostly prokaryotic microbes, contained carbonaceous cell walls commonly well-preserved by permineralization (i.e., "petrifaction") and exhibit relatively simple morphologies – spheroids, both solitary and aggregated in sheath-enclosed colonies, and unbranched many-celled filaments along with their vacated enclosing cylindrical sheaths (e.g., Schopf, 1968, 1992; Schopf et al., 2007; Javaux and Lepot, 2018). Paleobiological interpretations of such taxa have traditionally been based on detailed morphological comparison with similar extant microorganisms, their metabolism usually inferred from these comparisons and their environmental setting (Schopf, 1968; Knoll, 1985, 2012; Schopf et al., 2015). Relatively recent developments in ion microprobe analyses of individual carbonaceous microfossils (e.g., House et al., 2000; Ueno et al., 2001; Williford et al., 2013; Oehler et al., 2017) now permit in situ comparisons of morphological, geochemical, and carbon isotopic data to more definitively guide interpretations of ancient Precambrian ecosystems.

Many formally described Precambrian microfossils have been classified as cyanobacteria, oxygen-producing photosynthesizers, evidently extant millions of years into the Archean and well preceding the ~2.2–2.4 Ga Great Oxidation Event (GOE) (e.g., Anbar et al., 2007; Awramik et al., 1992; Buick 1992, 2008; Bosak et al., 2009; Kaufman et al., 2007). Some such taxa exhibit distinctively diagnostic cyanobacterial characteristics, such as many of those described from cherts of the ~850 Ma Bitter Springs Formation of central Australia which can be compared in cell-by-cell detail with genera and even species of extant Oscillatoriaceans, Nostocaceans, and Chroococcaceans (Schopf, 1968), whereas others, particularly those reported from Archean deposits, are less informative (e.g., Awramik et al., 1983; Walsh and Lowe, 1985; Klein et al., 1987; Ueno et al., 2001). Whereas oscillatoriacean cyanobacteria represent the most commonly reported group of photosynthetic prokaryotes in the fossil record, their diversity and evolutionary origin prior to the GOE remains uncertain (Golubic and Seong-Joo, 1999; Schopf, 2011; Sergeev et al., 2012; Butterfield, 2015). This seeming disparity between the Proterozoic and Archean fossil records is not surprising. Sediments surviving to the present from the Proterozoic are vastly more abundant than those of the older Archean and, with but few exceptions, are decidedly less geologically and geochemically altered. Thus, the more voluminous and better preserved Proterozoic fossil record is considered to be a useful reference for interpretation of putative Archean microfossil-like structures (e.g., Schopf et al., 2007).

In the Proterozoic – as in modern microbial mat communities – photoautotrophic cyanobacteria were prime contributors to the formation of such shallow-marine sedimentary structures as stromatolites (e.g., Grotzinger and Knoll, 1999), and their role in localized mineral precipitation has been implicated as well in the generation of pisolites, oncolites (e.g., Knoll et al., 1989; Swett and Knoll, 1989), and cherty and carbonate chemical sediments (e.g., Kremer et al.,

2012). Diverse types of cyanobacteria have also been recorded actively photosynthesizing within extant stromatolitic microbial mat communities (e.g., Reid et al., 2000; Burns et al., 2004).

The geochemical composition of individual Precambrian microfossils has recently been used both to verify and revise initial taxonomic classifications, and secondary ion mass spectrometry (SIMS) analyses of their stable carbon isotope ($\delta^{13}C$) compositions have revealed differences among Proterozoic and Archean microbial assemblages (e.g., House et al., 2000, 2013; Schopf et al., 2018), and between morphologically distinct microfossils (Williford et al., 2013) that previously had been masked in bulk (~25 g) analyses of whole-rock samples (see Strauss and Moore, 1992; Strauss et al., 1992a; Strauss et al., 1992b). These bulk mixtures are necessarily dominated by the prime organic carbon source, which consists of particulate detrital kerogen in addition to the preserved microbiota.

In the Precambrian, secular changes in the global carbon cycle are controlled by long-term variations in the fractional burial of organic carbon, most being recycled into the biosphere (Hayes et al., 1999; Des Marais, 2001). Nevertheless, the 25 ± 10‰ offset between $\delta^{13}C_{org}$ and $\delta^{13}C_{carb}$ has remained essentially constant throughout most of geologic history (Hayes et al., 1983; Hayes et al., 1999; Schidlowski, 2001). This robust isotopic difference between organic and inorganic carbon in Precambrian sedimentary rocks is primarily due to the preferential uptake of ^{12}C relative to ^{13}C during biological carbon fixation by primary producers. In photoautotrophs such as cyanobacteria (and higher plants), the ribulose-1,5-bisphosphate carboxylase/oxygenase (RuBisCO) enzyme is the biological molecule primarily responsible for the kinetic isotope effect that discriminates between ^{12}C and ^{13}C (e.g., Farquhar et al., 1989; Hayes, 1993). Thus, organic biomass becomes ^{13}C-depleted relative to the ^{13}C-enriched inorganic carbon (atmospheric CO_2 and

its dissolved carbonate rock-generating derivative, HCO_3^-), both signatures frequently preserved within minimally altered sedimentary rock units (Hayes et al., 1999; Schidlowski, 2001).

Despite the great inroads in deciphering the Precambrian fossil record since the inception of the modern field in the mid-1960s (Schopf, 2019), it has been difficult to reliably assess the physiological similarities (or differences) of morphologically comparable microfossils separated both spatially and temporally in the rock record. The fossils of the ~1,560 Ma Gaoyuzhuang Formation of Jixian, China and the ~850 Ma Kwagunt Formation of Arizona, U.S.A., meet this need – the deposits are geographically and temporally distinct, both contain microbial assemblages preserved by permineralization in shallow marine cherts, and many of their biotic components are morphologically virtually identical.

Studied samples of the Gaoyuzhuang Formation microbiota are preserved in finely laminated stromatolites, indicative of a relatively quiescent setting, whereas the fossiliferous Kwagunt cherts are pisolitic, deposited in a more agitated shallow-marine environment. In both deposits filamentous microfossils are abundant, widespread and three-dimensionally preserved. In the petrographic thin sections studied, small portions and occasionally longer parts of whole filaments are exposed at a thin section surface, in some instances free from background detrital kerogen making them particularly suitable for in situ SIMS carbon isotope analyses. SIMS-based comparison of fossil filaments in the two deposits thus provides a current state-of-the-art method to assess the physiological similarities, or lack thereof, of comparably preserved morphologically similar microfossils widely separated both in space and time.

2. MATERIALS AND METHODS

2.1. Geologic units studied

The Mesoproterozoic ~1,560 Ma Gaoyuzhuang Formation (Jixian Group of northern China) is a shallow-marine subtidal deposit containing abundant silicified conical stromatolites. Permineralized within the stromatolitic chert layers are unbranched, cylindrical, 2-4 μm-broad filamentous microfossils referred to *Eomycetopsis* sp. and interpreted to represent extracellular originally mucilaginous sheaths of oscillatoriacean cyanobacteria preserved as a result of early diagenetic silicification (Zhang, 1981; Schopf et al., 1984). In addition, here analyzed from the Gaoyuzhuang cherts are larger-diameter (30–40 μm-wide) tubules similar to the originally trichome-encompassing sheaths of *Lyngbya*-like oscillatoriaceans (e.g., Schopf and Sovietov, 1976; Schopf et al., 1984).

Carbonate rocks of the Gaoyuzhuang Formation evidence physically stable marine conditions and have carbon isotope ($\delta^{13}C_{carb}$) values that average –0.5 ± 0.5‰ and range from approximately –3‰ to +1‰ (Chu et al., 2004, 2007; Hongwei et al., 2011; Guo et al., 2013). Of numerous carbonates analyzed from the five formations of the Jixian Group (Guo et al., 2013) – in total having an average $\delta^{13}C_{carb}$ of –0.3‰ and ranging between –1‰ and +1‰ (with the exception of a 50-m interval that records a negative excursion to –2.5‰) – those of the Gaoyuzhuang Formation exhibit the least $\delta^{13}C_{carb}$ variability.

Bulk (25-g sample) $\delta^{13}C_{org}$ values for carbonaceous matter in Gaoyuzhuang chert and carbonate lithologies range from –32.0‰ to –26.4‰, and average –30.9‰ for total organic carbon (n = 8) and –31.2‰ for extracted kerogens (n = 2) (Strauss and Moore, 1992; Strauss et al., 1992b), values a few per mil lower than the average of –27.4 ± 1.2‰ for total organic carbon (n = 5) earlier reported by Schopf et al. (1984).

The minimum age of the Gaoyuzhuang Formation is constrained by U-Pb determinations of 1,559 ± 12 Ma measured by SIMS (SHRIMP) and 1,560 ± 5 Ma (LA-MC-ICPMS) in zircons from a tuff bed in the upper Gaoyuzhuang Formation (Li et al., 2010), refined from an earlier reported Pb-Pb age of 1,435 ± 50 Ma (Schopf et al., 1984) and assumed age of ~1,425 Ma (e.g., Moore and Schopf, 1992). Additional U-Pb age data from volcanics of the underlying Dahongyu Formation provide a maximum age of 1,625 ± 6.2 Ma (Lu and Li, 1991; Meng et al., 2011) for the fossiliferous cherts studied here.

The other geological unit here investigated, the Neoproterozoic Kwagunt Formation of the upper Chuar Supergroup in the Grand Canyon, Arizona (U.S.A.) is a shallow-marine peritidal deposit, the pisolitic cherts of the Walcott Member containing permineralized filamentous microfossils. The fossiliferous pisolites formed in a mildly agitated, tidally influenced setting through the sequential accretion of thin siliceous rinds that were repeatedly colonized by microbial communities (Schopf et al., 1973). The 2-4 μm-broad filamentous "*Eomycetopsis*-like" Kwagunt microfossils reported by Schopf et al. (1973) are morphologically closely similar to the *Eomycetopsis* specimens analyzed from the Gaoyuzhuang cherts (Fig. 2-1).

Most of the $\delta^{13}C_{carb}$ values measured for carbonates from the Walcott Member of the upper Kwagunt Formation fall within a wide range extending from –6‰ to +5‰, with an average of –1.1 ± 3.5‰; however, the least geochemically altered samples have values close to zero (Summons et al., 1988; Karlstrom et al., 2000). Bulk (~25 g) $\delta^{13}C_{org}$ values for carbonaceous matter extracted from shales, carbonates and cherts of the Kwagunt Formation range from –27.7‰ to –26.1‰ and average approximately –26.7‰ (n = 8) (Strauss and Moore, 1992), a value similar to earlier reported $\delta^{13}C_{org}$ values of –25.7 ± 0.13‰ (n = 4) for bulk kerogens and acid-macerated *Melanocyrillium* vase-shaped microfossils extracted from Kwagunt shales (Bloeser,

1985). Notably, all of these values fall within the broader range of –28‰ to –22‰ (average = –25.6 ± 1.3‰) measured throughout the Chuar Group strata (Karlstrom et al., 2000) and are similar to the average $\delta^{13}C_{org}$ value of –25.9‰ of carbonaceous matter analyzed in two additional Chuar Group carbonates (Summons et al., 1988).

The age of the Kwagunt Formation is estimated for the Walcott Member to be ~850 Ma (~830 to ~1,090 Ma) (Ford and Breed, 1973; Moore and Schopf, 1992) and is also constrained by a U-Pb age of 742 ± 6 Ma from an ash bed at the top of the Walcott Member (Karlstrom et al., 2000).

Bulk analyses of the $\delta^{13}C_{carb}$ and $\delta^{13}C_{org}$ compositions of the fossiliferous Gaoyuzhuang and Kwagunt Formations provide important reference points for evaluation of the SIMS analyses of individual microscopic fossils reported here from the two units. The $\delta^{13}C_{carb}$ and $\delta^{13}C_{org}$ values of the Gaoyuzhuang and Kwagunt Formations are similar (average $\delta^{13}C_{carb}$ values of –0.5 ± 0.5‰ and –1.1 ± 3.5‰, and average $\delta^{13}C_{org}$ values of –30.9‰ and –26.7‰, respectively), and they are typical of most other marine carbonate-dominated deposits analyzed from the Proterozoic rock record (Schidlowski, 2001).

2.2. Sample preparation

Polished ~50–150 μm-thick petrographic thin sections of cherts from the Gaoyuzhuang and Kwagunt Formations were surveyed using transmitted light optical microscopy to locate surface-exposed microfossils and associated detrital kerogen appropriate for SIMS analysis. Fossiliferous areas of thin sections containing surface-exposed filaments were cut into ~1” round mounts suitable for the SIMS sample holder, the fossils being positioned as close to the center of the mount as possible to avoid unwanted effects from measurements near the sample edge. The

samples and epoxy-mounted standards were cleaned and sonicated in deionized (DI) water three times for 1 min., rinsed in DI water after each treatment and then sonicated in ethanol for 30 s and again rinsed in DI water and sonicated for 1 min. The cleaned samples were then dried overnight in a vacuum oven at 50 °C. After cleaning, the target microfossils and associated kerogenous detritus in each mount were photographed using transmitted and reflected light at multiple magnifications (Fig. 2-1) using a Leica DM6000 housed at the NASA Jet Propulsion Laboratory (JPL) Astrobiogeochemistry Laboratory (abcLab), and their stage coordinates were documented relative to diamond scribe-inserted fiducial marks near the section edges.

Scanning electron microscopy (SEM) of the analyzed specimens was then performed at the JPL abcLab using a Hitachi SU-3500 SEM to acquire images in secondary and backscattered electron modes. After applying a 3-nm-thick platinum (Pt) veneer to the sample surface, SEM images were acquired under high vacuum using an accelerating voltage of 15 keV at a working distance of ~7 mm.

Prior to subsequent SIMS analyses at UCLA's W.M. Keck Foundation Center for Isotope Geochemistry, the mounts were covered with a thicker (~30 nm) gold coat required for conductivity, and were degassed overnight in the SIMS sample storage chamber. After each SIMS analysis session, the gold coat was removed with a 0.1-µm aluminum oxide polishing solution, and each specimen was re-imaged with the SEM in order to confirm the accuracy of the positioning of analytical SIMS pits.

2.3. Standards

Due to the scarcity of appropriate reference standards for calibrating the carbon isotopic compositions of chert-permineralized carbonaceous microfossils, this study began with analyses

of three new potential standard mounts prepared from carbonaceous chert samples of the ~3,350 Ma Fig Tree Group collected near Lows Creek in eastern Transvaal, South Africa and housed in the Precambrian Paleobiology Research Group (PPRG) collections at UCLA (Walter et al., 1983). Standards made from the Fig Tree chert include mount PPRG-215-1/2, as well as two others (FTS-1 and FTS-2) from a sample collected approximately 30 km south of Lows Creek on the southeastern side of the Barberton Greenstone Belt (25°55'S, 31°16'E) and provided to K. H. Williford by M. Van Kranendonk. To establish the suitability of new chert-kerogen standards from natural samples, it is desirable for them to contain carbonaceous matter of a known – and ideally homogenous – carbon isotope composition, yield a carbon secondary ion signal intensity within the same dynamic range as that found within fossiliferous cherts, and come from a geologic unit with a well-characterized depositional context and thermal maturity. The newly prepared standards each contain three or four rock chips of organic-rich chert centered within a ~1" round epoxy mount and polished to a <1-μm finish. Multiple $\delta^{13}C_{org}$ measurements were made on the individual rock chips to determine their isotopic homogeneity and thereby establish their suitability for use as SIMS standards. These "rock chip measurements" were then compared to preexisting Fig Tree chert standard PPRG-215-2a from the original rock collection (Hayes et al., 1983; Walter et al., 1983; House et al., 2000), previously used in SIMS studies of similarly preserved Precambrian microfossils (e.g., House et al., 2000, 2013; Williford et al., 2013) and having an established $\delta^{13}C_{org}$ value of –31.5‰ (Hayes et al., 1983; House et al., 2000).

2.4. Raman spectroscopy

Raman spectroscopy was used to document the kerogenous composition and geochemical maturity of each analyzed microfossil as well as those of the associated particulate detrital kerogen

(Fig. 2-2). Raman point spectra and 2-D geochemical maps were acquired and used to characterize the spatial relationships between fossil and associated kerogen and the enclosing microcrystalline quartz chert matrix (Figs. 2-2B and 2-2E). These Raman data were acquired at the Raman Laboratory of UCLA's Center for the Study of Evolution and the Origin of Life using a T64000 triple-stage confocal laser-Raman system equipped with an argon ion laser having an excitation wavelength of 457.9 nm, a spectral window centered at ~1700 cm^{-1} and a ~1 μm spot size. Two-dimensional Raman geochemical maps were acquired across a ~20×20-μm area at 0.5–2.0 μm depth. Spectra here shown (Figs. 2-2C and 2-2F) are normalized to the intensity of the G-band of kerogen.

Raman geothermometry calculations were performed to provide an estimate of peak metamorphic temperatures. Processed Raman spectra of kerogen were deconvoluted using the method described by Kouketsu et al. (2014) with the software package PeakFit (v.4.12; SeaSolve Software Inc., Massachusetts, U.S.A.) using their "fitting G" for low-grade carbonaceous matter of the Gaoyuzhuang and Kwagunt Formations, and "fitting D" and "fitting B" for the PPRG-215-1 and FTS-1 standards, respectively. From these deconvoluted spectra, approximate peak metamorphic temperatures were calculated using the equation

(1) $$T\ (°C) = -2.15(\text{FWHM-D1}) + 478$$

where FWHM-D1 (cm^{-1}) represents the full width at half maximum for the D1 Raman band of carbonaceous matter (i.e., kerogen) centered at 1350 cm^{-1}. This calculation is reliable for temperature measurements in the range of 150–400 °C with an error of ±30 °C (Kouketsu et al. 2014).

2.5. Carbon isotope measurements

2.5.1. Bulk carbon isotope analysis

Samples from the Gaoyuzhuang and Kwagunt cherts used in this study had been previously analyzed to determine their "whole rock" (bulk, 25-g sample) carbon isotope compositions (Strauss and Moore, 1992; Strauss et al., 1992b). In the Astrobiogeochemistry Lab at the NASA Jet Propulsion Laboratory (JPL), multiple new $\delta^{13}C$ measurements were made of the carbonaceous residues from hydrochloric acid-dissolved rock chips of the Fig Tree chert used to prepare the new reference mounts (FTS-1, FTS-2), the same geologic unit from which the original PPRG-215-1 standard was initially obtained (Hayes et al., 1983; House et al., 2000). Rock chip samples of black chert (~5 g) were powdered and treated in 6N HCl for 72 hours at 60°C, with the acid being replaced twice after 24 hours. The carbon abundances of the resulting residues were prepared for analysis via combustion and automated, preparative chemistry using a Costech 4010 Elemental Analyzer, and their total organic carbon (TOC) and $\delta^{13}C_{org}$ values measured by a coupled Thermo Delta V Plus isotope-ratio mass spectrometer. TOC was calculated by comparing the integrated area under peaks for m/z 44, 45, and 46 ions in the samples with those from multiple analyses of acetanilide reference material (having a known total carbon abundance) acquired during the same sequence.

2.5.2. SIMS carbon isotope analysis

SIMS carbon isotope measurements were performed during two analytical sessions (5/25/2018 and 1/9–1/14/2019) on the CAMECA IMS-1290 at UCLA using multicollection mode with $^{12}C_2^-$ detected on a Faraday cup and $^{12}C^{13}C^-$ detected using an electron multiplier at a mass resolution of ~6,000 that resulted in the separation of molecular hydride interferences. A 20 keV,

~1–2 nA $^{133}Cs^{+}$ primary ion beam was focused to a 10 μm spot size; a 5×5 μm raster in combination with 100% dynamic transfer was used during the measurements to reduce the down-pit isotope fractionation. Each analysis included 45 s of presputtering and a total counting time of 240 s over 20 measurement cycles. Count rates determined with the electron multiplier were corrected for deadtime (65 ns) and Faraday cup signals were corrected for background levels determined for each analysis by deflecting the secondary ion beam out of the Faraday cup during presputtering. Internal precision was determined as two standard errors (2SE) of $^{12}C^{13}C/^{12}C^{12}C$ ratios from the 20 cycles.

Multiple measurements of the chert-kerogen standard were used to bracket groups of 15–20 analyzed specimens. The small size of the analyzed fossil filaments (many ~2–4 μm in diameter) compared to the diameter of the analytical spot (~10 μm) yielded low ion count rates and lower precision compared to larger and/or better exposed fossils and more carbon-rich areas of the chert matrix. Microfossil analyses having low relative count rates ($^{12}C_2^-_{rel}$, %) below ~7%, were noted although there was no observed correlation between $\delta^{13}C_{org}$ and $^{12}C_2^-_{rel}$ values for accepted sample analyses, with the exception of some kerogen-poor background measurements (Table 2-1; Figs. 2-6 and 2-7). Analyses of associated detrital kerogen typically had low relative count rates due to the sparse distribution of particulate organic matter in the analyzed cherts, and thus the $\delta^{13}C_{org}$ values for background kerogen are here included in the data presented despite having relatively low internal precision.

Instrumental bias (α_{SIMS}) was determined by calculating the average "raw" value ($\delta^{13}C_{raw} = [(^{12}C^{13}C/^{12}C^{12}C)_{measured}/(0.01118 \times 2) - 1] \times 1000$) using the revised $^{13}C/^{12}C$ ratio of 0.01118 for VPDB (Chang and Li, 1990; Farquhar and Lloyd, 1993; Beerling, 2001), for 5 to 8 bracketing analyses of the working standard (PPRG-215-1/2 or FTS-1) compared to its average carbon

isotopic ($\delta^{13}C_{bulk}$) value (PPRG-215-1/2 = –31.5‰, Hayes et al., 1983; FTS-1 = –13.5‰, this study), following the method described by Kita et al. (2009) and Williford et al. (2013):

(2) $$\alpha_{SIMS} = (\delta^{13}C_{raw} + 1000)/(\delta^{13}C_{bulk} + 1000).$$

The α_{SIMS} value thus obtained permits the correction of raw $\delta^{13}C$ values for unknown sample analyses using a second equation (Williford et al., 2013):

(3) $$\delta^{13}C_{VPDB}(sample) = [(1 + \delta^{13}C_{raw}(sample)/1000/\alpha_{SIMS} - 1] \times 1000.$$

Following the methods established by previous SIMS studies of kerogenous microfossils (e.g., House et al., 2013; Williford et al., 2013; Schopf et al., 2018), external precision (i.e., reproducibility) was calculated as two standard deviations (±2SD) of the $\delta^{13}C_{raw}$ values obtained for the bracketing measurements of the standard. Internal precision was calculated as two standard errors (±2SE) of $\delta^{13}C_{raw}$ values measured over 20 individual cycles for each SIMS analysis, results largely influenced by the heterogeneity in abundance of organic carbon at depth within the target area affecting counting statistics.

3. RESULTS

Over the course of the two SIMS analytical sessions, a total of 307 analyses were made including 241 measurements of the chert-kerogen reference standards and 66 measurements of target-sample microfossils and associated particulate kerogen. In general, the standards exhibited greater secondary ion intensities (>1.5×10^6 cps, counts per second for $^{12}C^{12}C^-$) and more isotopic homogeneity (± ~1.5–3.5‰; 2SD) than the samples. The large number of measurements performed in this study enabled detailed evaluation of the newly prepared reference standards for their suitability as chert-kerogen standards in SIMS $\delta^{13}C_{org}$ analyses, and for comparison of the

variation among carbon isotope signatures preserved in carbonaceous microfossils chert-permineralized in two temporally and spatially disparate Proterozoic marine ecosystems. Raman spectra of quartz and kerogen in the samples and standards demonstrate the similarities in their geochemical composition. The FTS-1 mount was used as the primary working standard during SIMS sample analyses, and the instrumental mass fractionation (IMF, ‰) for this standard averaged –15.2‰ during the first session (n = 18) and –14.3‰ for the second session (n = 81). The IMF determined for the other chert-kerogen standards measured during the second session are within ~2‰ of the average value for FTS-1. These data indicate that any matrix effects arising from chemical and/or mineralogical differences between the samples and standards during SIMS analysis are minimal. Raman geothermometry calculations for kerogen show a large difference in estimated peak metamorphic temperatures between the samples and the standards, and between the two isotopically distinct standards. Kerogen in the Gaoyuzhuang Formation cherts has an approximate peak temperature of ~230 ± 30 °C, and the Kwagunt Formation samples have a similar estimated value of ~190 ± 30 °C. Peak temperatures for the standards are estimated to be much higher, with the PPRG-215 sample producing an average of ~375 ± 30 °C, and the FTS-1 sample reaching temperatures greater than 400 °C (Table 2-2; Fig. 2-8).

3.1. Chert-kerogen standards

The original Fig Tree chert standard (PPRG-215-2a) and the newly prepared mount from the same rock (PPRG-215-1/2) analyzed in this study (n = 114) had consistent $^{12}C^{13}C/^{12}C^{12}C$ ratios (±1.5–3.5‰; 2SD) and an experimental bias (i.e., instrumental mass fractionation) of roughly –14 to –16‰ with an average $^{12}C_2^-$ count rate of 1.8×10^6 cps. The two additional newly prepared Fig Tree chert standards (FTS-1, FTS-2; n = 127) are isotopically distinct from the PPRG-215

standards (PPRG-215-2a, PPRG-215-1/2), offset by ~18‰, a difference consistent with $\delta^{13}C_{org}$ data obtained from bulk measurements of the FTS standards which yielded an average of –13.52‰ ± 0.03 (n = 4). SIMS analyses of the FTS standards yielded similarly consistent $\delta^{13}C$ values (±1.4–2.3‰; 2SD) with an experimental bias ranging from ~14–16‰ and an average $^{12}C_2^-$ count rate of 2.3×10^6 cps. External precision (2SD) averaged ~2.7‰ and ~2.0‰ for all accepted analyses of the PPRG-215 and FTS mounts, respectively, and external precision for bracketing measurements ranged from ~1.1‰ to ~1.5‰ with minimal instrument drift and consistent α_{SIMS} values ranging from ~0.984–0.986 (Table 2-1). Average internal precision (2SE) was ~1.3‰ for the PPRG standards and ~1.2‰ for the FTS standards. To avoid overestimation of errors and better reflect variations in isotopic compositions and $^{12}C_2^-$ count rates within one spot, total uncertainty (i.e., final error) is expressed as the square root of the sum of the squares for the standard error of the mean for the bracketing measurements and the internal precision of each sample analysis (Table 2-1). SIMS measurements having $^{12}C_2^-$ count rates below 2.0×10^5 cps were discarded from the data, with the exception of background particulate kerogen analyses of the samples. As shown in Table 2-2, the new bulk measurements showed that the total organic carbon (TOC) values for the FTS samples were consistently ~0.45 mg/g, compared to ~1.40 mg/g from previous measurements of the whole-rock PPRG-215 samples (Hayes et al., 1983).

3.2. Microfossil samples

The $\delta^{13}C_{org}$ values of the SIMS target samples, fossils and associated background kerogen, ranged from –33.8‰ to –22.4‰, with an average count rate of 8.5×10^5 (cps) (Table 2-1, Fig. 2-3). Gaoyuzhuang microfossils (n = 34; Fig. 2-4) had an average $\delta^{13}C_{org}$ of –29.4 ± 2.5‰, the associated particulate kerogen measuring on average –30.3 ± 2.9‰ (n = 15). Values for 2–4 μm-

wide Gaoyuzhuang *Eomycetopsis* fossils averaged –28.9 ± 2.2‰ whereas the broader, 30–40 µm-diameter *Lyngbya*-like tubules from the unit had an average $\delta^{13}C_{org}$ value of –31.2 ± 2.9‰ (n = 5). Average internal precision (2SE) for all measurements of the Gaoyuzhuang samples was ~1.9‰, and the average $^{12}C_2^-$ count rate was ~7.5×10^5 cps. *Eomycetopsis* microfossils from the Kwagunt Formation (n = 17; Fig. 2-5) yielded an average $\delta^{13}C_{org}$ of –29.0 ± 1.8‰, and the average for background kerogen was –24.3 ± 1.9‰ (n = 5); however, the background measurements yielded notably low count rates ($^{12}C_2^-{}_{rel}$ below 7%). Average internal precision for all measurements of the Kwagunt samples was 2.1‰, and the average $^{12}C_2^-$ count rate was ~1.0×10^6 cps.

4. DISCUSSION

Filamentous microfossils permineralized in carbonaceous cherts of the ~1,560 Ma Gaoyuzhuang Formation of northern China and ~850 Ma Kwagunt Formation of Arizona, U.S.A. share very similar morphological and preservational characteristics despite being widely separated in both space and time, the comparability of their microbial components attributable to the hypobradytely characteristic of Precambrian cyanobacteria (Schopf, 1994). Although previous paleobiological studies and bulk carbon isotope analyses of organic matter from these deposits firmly implicated the photoautotrophic composition of the two communities, it has been only recently that the combination of morphological, geochemical, and isotopic analyses of individual microfossils has been available to confirm these interpretations. Using optical microscopy, Raman spectroscopy, and SIMS to analyze, respectively, the morphological, geochemical, and isotopic

composition of the fossils, the data here presented substantiate their earlier proposed taxonomic assignments and provide new means to verify their metabolic characteristics.

4.1. Chert-kerogen standards

Despite having been collected from the same geological unit, rock chip measurements of two of the newly prepared Fig Tree chert-kerogen reference standards for SIMS carbon isotope studies (FTS-1, FTS-2) differ significantly from those of the originally used PPRG-215 sample (PPRG-215-2a) and the second mount prepared from the same collection (PPRG-215-1/2). Whereas the two PPRG samples yielded bulk $\delta^{13}C_{org}$ values of approximately –31.5‰, the new FTS standards – collected at a more metamorphosed locality than that originally sampled – were relatively enriched in ^{13}C by ~18‰, having an average value of –13.5‰. Raman spectroscopy analyses of the kerogen in the two sets of standards similarly showed a difference in the geochemical maturity of their kerogenous components consistent with their geologic settings, those in the FTS samples being appreciably more heated and geochemically altered (Fig. 2-8). These results are supported by previously reported Raman data from thermally altered kerogens within the variably metamorphosed Barberton Greenstone Belt (Tice et al., 2004).

It should be noted, however, that despite the marked differences between the two sets of standards, in SIMS analyses of Precambrian microfossils the use of two isotopically (and geothermally) distinct standards is potentially valuable, the combination of the differing data sets providing two-point calibration, a technique that has been suggested to improve the reliability of stable isotope measurements and their subsequent interpretation (Jardine and Cunjak, 2005). For this study, a simple calibration using all of the accepted standard analyses from the second analytical session (n = 218) can be applied to the raw $\delta^{13}C$ SIMS values measured for unknown

sample analyses during that session ($\delta^{13}C_{VPDB}$(calibrated) = 0.9561 × $\delta^{13}C_{raw}$ + 13.069), which yields comparable $\delta^{13}C_{org}$ values ~1–2‰ higher than those calculated from equation 3 described above, and a similar internal precision of ~2.3‰ (2SE; standard error of the regression).

4.2. SIMS carbon isotope analyses

The $\delta^{13}C_{org}$ values of *Eomycetopsis* sp. specimens from the Gaoyuzhuang (average = –28.9‰) and Kwagunt cherts (average = –29.0‰) are indistinguishable despite their notable separation in space and time, a similarity consistent with the marked comparability of their filamentous morphologies, shallow-marine depositional settings, and with the known evolutionary history of oscillatoriacean cyanobacteria. The $\delta^{13}C_{org}$ values of the Gaoyuzhuang *Lyngbya*-like sheaths (–31.2‰) are also within the range of the smaller *Eomycetopsis* filaments in both units, albeit some 2‰ lower on average, with the measured values and calculated fractionations of all specimens falling within the range determined for modern microbial phototrophs (e.g., Schidlowski, 2001; Zerkle et al., 2005; Orphan and House, 2009) as well as within the ranges reported for other SIMS-analyzed Precambrian cyanobacterial fossils (e.g., House et al., 2000, 2013; Williford et al., 2013). Such carbon isotope fractionations are consistent with autotrophic carbon fixation through the Calvin cycle using RuBisCO (cf., House et al., 2000). Many earlier SIMS studies appropriately stressed the importance of interpreting stable carbon isotope values (and fractionations) from Precambrian fossils and host rocks in their proper geological, paleobiological, and preservational context. These factors, which largely control the final isotopic composition of fossil kerogens, are discussed below.

4.3. Carbon isotopes of Proterozoic microfossils

The $\delta^{13}C_{org}$ composition of Precambrian sedimentary kerogen is primarily determined by the biosynthetic processes involved in its formation; however, modern microorganisms kinetically fractionate carbon isotopes to differing extents depending on the type of metabolism (e.g., Hayes, 2001; Schidlowski, 2001; Zerkle et al., 2005). Given this, the sedimentary $\delta^{13}C_{org}$ record has been used to infer ancient carbon fixation pathways and explore the biogeochemical carbon cycle of the early Earth (Des Marais, 1997; Hayes et al., 1999; Schidlowski, 2001), including physiological interpretations of silicified Precambrian microfossils (e.g., House et al., 2000, 2013; Williford et al., 2013) similar to those investigated here.

In addition to metabolism, the $\delta^{13}C_{org}$ value of modern microorganisms and preserved microfossils is affected by the isotopic composition of their inorganic carbon source (e.g., $CO_{2(aq)}$ or HCO_3^-), including deposits within the relatively inconstant shallow-marine photic zone such as those here studied. It has also been shown that extant cyanobacteria are capable of using either dissolved CO_2 or HCO_3^- (Badger and Price, 2003), processes that would presumably result in differing isotopic compositions for biomass. Although it is generally assumed that the ocean–atmosphere and inorganic pools of CO_2 and HCO_3^- were in thermodynamic equilibrium (with equilibrium isotopic fractionation) throughout the Proterozoic (e.g., Schidlowski, 2001; Kaufman and Xiao, 2003), the concentration of CO_2 has been highlighted for its simplicity in interpreting isotopic fractionations (e.g., House et al., 2000; Williford et al., 2013) and the capability of cyanobacteria to use HCO_3^- is thought to be a more recent development and/or rare occurrence – perhaps evolved as a response to lower atmospheric CO_2 concentrations (Badger and Price, 2003; Nisbet et al., 2014). The $\delta^{13}C_{carb}$ composition of most sedimentary carbonates therefore likely records the $\delta^{13}C$ of dissolved inorganic carbon (DIC) available to ancient microorganisms and thus

the difference between $\delta^{13}C_{carb}$ and $\delta^{13}C_{org}$ values can be used to estimate total metabolic fractionations ($\Delta^{13}C = \delta^{13}C_{DIC} - \delta^{13}C_{org}$) (Williford et al., 2013). This relationship is further expanded using the following equation (Hayes et al., 1999):

(4) $$\Delta^{13}C_{carb-org} = \Delta_{carb} + \varepsilon_p - \Delta_2$$

in which Δ_{carb} represents the equilibrium isotope fractionation between sedimentary carbonate and dissolved $CO_{2(aq)}$, which is temperature-dependent and ranges from ~7‰ at 30 °C to 10.4‰ at 0 °C, assuming an isotopic composition of calcium carbonate minerals (e.g., calcite, $CaCO_3$) relative to DIC (e.g., bicarbonate, HCO_3^-) that is lower by ~1.2‰ (Hayes et al., 1999). The value for kinetic isotope fractionation associated with autotrophic biosynthesis (ε_p) is the greatest contributing factor affecting the primary $\delta^{13}C_{org}$ composition of recently deposited organic matter and the later formation of fossil kerogen. Secondary alteration (Δ_2) represents the isotope effect(s) due to post-depositional processes that alter the initial carbon isotope signature, including decomposition, heterotrophic degradation and thermal alteration due to burial and metamorphism.

For extant photoautotrophic microbes, isotope fractionation due to carbon fixation ($\varepsilon_p = \delta^{13}C_{substrate} - \delta^{13}C_{fixed\ carbon}$) is dependent on environmental and physiological factors not only including dissolved CO_2 concentrations but also nutrient availability, cell geometry and growth rate (e.g., Guy et al., 1993; Laws et al., 1995; Laws et al., 1997; Popp et al., 1998; Cassar et al., 2006). Laboratory studies show that ε_p for the carboxylation of RuBisCO by cyanobacteria has a typical range of ~16–22‰ (e.g., Guy et al., 1993; Popp et al., 1998) and a potential maximum fractionation of ~25‰ (e.g., Kaufman and Xiao, 2003), compared to phototrophic eukaryotes which have ε_p values up to 32‰ (Roeske and O'Leary, 1985; Hayes et al., 1999). Given these considerations, the $\delta^{13}C_{org}$ values measured for the *Eomycetopsis* specimens of the Gaoyuzhuang and Kwagunt cherts approach the maximum estimated ε_p for cyanobacteria, considering most of

the $\delta^{13}C_{carb}$ values for these units are between –1‰ and +1‰ and assuming the surface ocean temperatures were 15–30 °C (e.g., Knauth, 2005; Garcia et al., 2017). This suggests the shallow-marine *Eomycetopsis* populations were not limited by low $CO_{2(aq)}$ concentrations or high growth rates, conditions which tend to lower ε_p values in laboratory studies (e.g., Laws et al., 1995, 1997).

In the two deposits studied here, a significant role of secondary alteration affecting preserved isotopic ratios is ruled out by the Raman spectra obtained both for the microfossil-comprising kerogen and the kerogen of the associated background organic matter. Comparing the Raman spectra of the Gaoyuzhuang and Kwagunt microfossils (Fig. 2-2) with previously reported data (e.g., Schopf et al., 2005; Kouketsu et al., 2014), it is apparent that the microfossils are composed of thermally immature kerogen – below greenschist facies – and that geochemical thermal alteration can be essentially excluded for the specimens studied here (Schidlowski, 2001; Schiffbauer et al., 2012).

The role of heterotrophic recycling by post-depositional biodegradation might also be considered as a possible factor affecting the isotopic composition of fossil kerogen. Measurements of background associated detrital kerogen in the Gaoyuzhuang samples, yielding $\delta^{13}C_{org}$ values (–30.3 ± 2.9‰) similar to previous bulk measurements (ca. –28 to –31‰) for this unit, are well within the range of values for the microfossils (–29.4 ± 2.5‰), suggesting that the fossils and associated organic matter probably share a common biosynthetic origin. In contrast, although the Kwagunt $\delta^{13}C_{org}$ analyses for such subsidiary kerogen (–24.3 ± 1.9‰) suffer from relatively low count rates, they are more similar to bulk measurements of whole-rock specimens (ca. –24 to –26‰), which are ~3–5‰ higher than the values measured for the *Eomycetopsis* fossils (–29.0 ± 1.8‰). This difference, though relatively small, could represent deposition of recycled exogenous organic matter (Johnston et al., 2012) or it may reflect the occurrence of degradation by co-existing

heterotrophs, perhaps marine protozoans or early-evolved soft-bodied metazoans (the Kwagunt dating from ~850 Ma) as the cyanobacterial sheaths were selectively preserved (Bartley, 1996). DeNiro and Epstein (1978) classically stated, "You are what you eat (plus a few ‰)," describing the isotopic effects of heterotrophic alteration on the primary biomass or food source. Whereas thermal alteration can potentially increase $\delta^{13}C_{org}$ values >10‰ in highly metamorphosed rocks (Schidlowski, 2001) – as shown here by the 18‰ offset between the two sets of SIMS standards – the effects of heterotrophic recycling are unlikely to exceed ~5‰ in marine settings (Hayes, 1993) and would require a much larger sample size to properly establish in the Proterozoic rock record.

4.4. Biological affinities of microfossils

Analyses of ^{13}C-depleted carbon in kerogenous organic matter, even for specific microfossils, may not be directly indicative of biological affinities. Like carbon fixation within the Calvin cycle, other cellular metabolisms, such as the acetyl-CoA pathway (Fuchs et al., 1979; Schidlowski et al., 1983; Preuβ et al., 1989) have been shown to kinetically fractionate carbon isotopes to comparable magnitudes. Nevertheless, the combination of shared morphological features and similar $\delta^{13}C_{org}$ values among the filamentous microfossils studied here, and their notable similarity to extant and other fossil microbial phototrophs, as well as their demonstrable occurrence in the photic zone of shallow-marine environments, all firmly support their classification as oxygen-producing cyanobacteria, photoautotrophs utilizing the Calvin cycle responsible for their characteristic $\delta^{13}C_{org}$ values. The available data thus support and corroborate the previous taxonomic oscillatoriacean cyanobacterial assignment of the *Eomycetopsis* and

Lyngbya-like microfossils of the Gaoyuzhuang and Kwagunt Formations (e.g., Schopf et al., 1973; Schopf et al., 1984).

An alternative explanation for the similar $\delta^{13}C_{org}$ values – and interpretation of the microfossil physiologies – is that they may represent facultative oxygenic–anoxygenic cyanobacteria (e.g., Cohen et al., 1975; 1986). Among extant oscillatoriaceans this is a relatively widespread capability (e.g., Padan, 1979) that reflects the derivation of the cyanobacterial lineage from anoxygenic photosynthetic bacteria, which should have remained prevalent in the Proterozoic oceans (Johnston et al., 2009). Affinities with other early-evolved lineages, particularly methanogens, methanotrophs, and sulfur- or sulfate-reducing microbes can be effectively ruled out due to a combination of differences in morphology, metabolisms, isotopic signatures and/or depositional setting.

The findings of this study contribute to the increase in data obtained for SIMS $\delta^{13}C_{org}$ analyses of carbonaceous Precambrian microfossils and illustrates the potential for indistinguishable carbon isotope values to be preserved within samples sharing distinct morphological and depositional similarities, despite being widely separated in both space and time. Using additional data from carbon isotope measurements of inorganic carbon ($\delta^{13}C_{carb}$) and Raman spectroscopy, the possibility of reconstructing ancient carbon fixation pathways for these filamentous microfossils has become further constrained by in situ SIMS analyses, and in conclusion documents the ubiquity, persistence, and extremely slow evolution of oxygen-producing oscillatoriacean cyanobacteria, dominant components of shallow water photic zone environments throughout much of Earth's Precambrian history.

TABLES

Date	Analysis	Sample-Specimen	Thin section	Description	$\delta^{13}C_{VPDB}$ (‰ VPDB)	Error (±)	$\delta^{13}C_{raw}$ (‰ VPDB)	±2 SE* (‰)	$^{12}C_2^-$ (cps)	$^{12}C_2^-$ rel (%)	$^{133}Cs^+$ intensity (nA)	α_{SIMS}	±2 SD** (‰)	IMF (‰)	SEM
Gaoyuzhuang Formation															
05/25/18	15	GAO-18	UCLA-1A-2	*Eomycetopsis* sp.	-31.0	0.50	-46.0	0.86	1.3E+06	45%	1.1	0.985	1.46	-15.3	0.25836
05/25/18	16	GAO-20	UCLA-1A-2	*Eomycetopsis* sp.	-31.0	1.15	-46.0	2.24	5.5E+05	19%	1.1	0.985	1.46	-15.3	0.25836
05/25/18	17	GAO-11-1	UCLA-1C-1	*Eomycetopsis* sp.	-30.2	0.74	-45.3	1.39	1.1E+06	37%	1.1	0.985	1.46	-15.3	0.25836
05/25/18	18	GAO-11-2	UCLA-1C-1	*Eomycetopsis* sp.	-30.0	1.38	-45.0	2.70	7.8E+05	27%	1.1	0.985	1.46	-15.3	0.25836
05/25/18	20	GAO-7-2	UCLA-1C-1	*Eomycetopsis* sp.	-32.6	0.69	-47.6	1.28	8.3E+05	28%	2.1	0.985	1.46	-15.3	0.25836
05/25/18	21	GAO-7-1	UCLA-1C-1	*Eomycetopsis* sp.	-26.0	1.30	-41.1	2.56	5.3E+05	18%	2.1	0.985	1.46	-15.3	0.25836
05/25/18	22	GAO-6	UCLA-1C-1	*Eomycetopsis* sp.	-27.7	0.95	-42.8	1.84	7.5E+05	26%	2.1	0.985	1.46	-15.3	0.25836
01/14/19	221	GAO-12-1	UCLA-1A-1	*Eomycetopsis* sp.	-28.3	1.54	-41.9	3.05	2.4E+05	8%	0.9	0.986	1.15	-13.9	0.20248
01/14/19	222	GAO-12-2	UCLA-1A-1	*Eomycetopsis* sp.	-25.7	0.77	-39.4	1.49	6.6E+05	21%	0.9	0.986	1.15	-13.9	0.20248
01/14/19	223	GAO-13A-1	UCLA-1A-1	*Lyngbya* -like sheath	-33.5	1.31	-47.1	2.58	2.8E+05	9%	0.9	0.986	1.15	-13.9	0.20248
01/14/19	224	GAO-13A-2	UCLA-1A-1	*Lyngbya* -like sheath	-26.3	1.48	-40.0	2.94	2.3E+05	7%	0.9	0.986	1.15	-13.9	0.20248
01/14/19	225	GAO-13B	UCLA-1A-1	*Lyngbya* -like sheath	-31.2	1.03	-44.8	2.02	3.8E+05	12%	0.9	0.986	1.15	-13.9	0.20248
01/14/19	226	GAO-13C-1	UCLA-1A-1	*Lyngbya* -like sheath	-32.8	1.03	-46.5	2.02	4.5E+05	14%	0.9	0.986	1.15	-13.9	0.20248
01/14/19	227	GAO-13C-2	UCLA-1A-1	*Lyngbya* -like sheath	-32.3	0.75	-46.0	1.45	5.1E+05	16%	0.9	0.986	1.15	-13.9	0.20248
01/14/19	228	GAO-14-1	UCLA-1A-1	*Eomycetopsis* sp.	-30.2	0.95	-43.9	1.85	3.7E+05	12%	0.9	0.986	1.15	-13.9	0.20248
01/14/19	229	GAO-14-2	UCLA-1A-1	*Eomycetopsis* sp.	-28.2	0.96	-41.9	1.88	3.0E+05	9%	0.9	0.986	1.15	-13.9	0.20248
01/14/19	230	GAO-21	UCLA-1A-1	Background kerogen	-30.7	0.54	-44.4	1.01	8.6E+05	27%	0.9	0.986	1.15	-13.9	0.20248
01/14/19	231	GAO-22	UCLA-1A-1	*Eomycetopsis* sp.	-32.2	1.22	-45.9	2.40	2.7E+05	9%	0.9	0.986	1.15	-13.9	0.20248
01/14/19	232	GAO-23	UCLA-1A-1	*Eomycetopsis* sp.	-27.6	0.79	-41.3	1.53	5.0E+05	16%	0.9	0.986	1.15	-13.9	0.20248
01/14/19	233	GAO-24-1	UCLA-1A-1	*Eomycetopsis* sp.	-25.1	0.60	-38.8	1.14	1.1E+06	35%	0.9	0.986	1.15	-13.9	0.20248
01/14/19	234	GAO-24-2	UCLA-1A-1	*Eomycetopsis* sp.	-27.7	1.22	-41.4	2.40	7.5E+05	24%	0.9	0.986	1.15	-13.9	0.20248
01/14/19	235	GAO-25	UCLA-1A-1	Background kerogen	-29.2	1.69	-42.8	3.35	2.2E+05	7%	0.9	0.986	1.15	-13.9	0.20248
01/14/19	236	GAO-25-2	UCLA-1A-1	Background kerogen	-30.7	0.79	-44.3	1.53	5.8E+05	18%	0.8	0.986	1.15	-13.9	0.20248
01/14/19	237	GAO-25-3	UCLA-1A-1	Background kerogen	-29.4	0.64	-43.1	1.22	6.2E+05	19%	0.8	0.986	1.15	-13.9	0.20248
01/14/19	238	GAO-26-1	UCLA-1A-1	Background kerogen	-24.8	0.99	-38.5	1.94	4.2E+05	13%	0.9	0.986	1.15	-13.9	0.20248
01/14/19	239	GAO-26-2	UCLA-1A-1	Background kerogen	-27.4	0.63	-41.1	1.20	4.9E+05	16%	0.9	0.986	1.15	-13.9	0.20248
01/14/19	244	GAO-26-3	UCLA-1A-1	Background kerogen	-27.5	0.96	-41.1	1.88	6.1E+05	27%	0.9	0.986	1.10	-13.8	0.20718
01/14/19	245	GAO-27-1	UCLA-1A-1	Background kerogen	-33.6	1.36	-47.1	2.68	2.2E+05	10%	0.9	0.986	1.10	-13.8	0.20718
01/14/19	246	GAO-27-2	UCLA-1A-1	Background kerogen	-33.2	1.41	-46.7	2.79	2.5E+05	11%	0.9	0.986	1.10	-13.8	0.20718
01/14/19	247	GAO-28-1	UCLA-1A-1	Background kerogen	-33.8	0.40	-47.3	0.69	4.0E+06	182%	0.9	0.986	1.10	-13.8	0.20718
01/14/19	248	GAO-28-2	UCLA-1A-1	Background kerogen	-33.2	0.48	-46.6	0.86	1.5E+06	66%	0.9	0.986	1.10	-13.8	0.20718
01/14/19	249	GAO-28-3	UCLA-1A-1	Background kerogen	-32.8	0.67	-46.3	1.27	1.2E+06	53%	0.9	0.986	1.10	-13.8	0.20718
01/14/19	250	GAO-29-1	UCLA-1A-1	Background kerogen	-30.7	0.66	-44.3	1.26	1.7E+06	78%	0.9	0.986	1.10	-13.8	0.20718
01/14/19	251	GAO-29-2	UCLA-1A-1	Background kerogen	-31.6	0.43	-45.2	0.75	2.0E+06	92%	0.9	0.986	1.10	-13.8	0.20718
01/14/19	252	GAO-30	UCLA-1A-1	Background kerogen	-25.5	1.16	-39.1	2.29	3.0E+05	14%	0.9	0.986	1.10	-13.8	0.20718
01/14/19	253	GAO-31	UCLA-1A-1	*Eomycetopsis* sp.	-29.3	0.60	-42.8	1.13	1.0E+06	45%	0.9	0.986	1.10	-13.8	0.20718
01/14/19	254	GAO-32	UCLA-1A-1	*Eomycetopsis* sp.	-31.6	0.94	-45.1	1.84	4.8E+05	22%	0.9	0.986	1.10	-13.8	0.20718
01/14/19	255	GAO-33A	UCLA-1A-1	*Eomycetopsis* sp.	-26.8	0.96	-40.3	1.87	6.6E+05	30%	0.9	0.986	1.10	-13.8	0.20718
01/14/19	256	GAO-33B	UCLA-1A-1	*Eomycetopsis* sp.	-29.2	0.98	-42.8	1.91	7.0E+05	31%	0.9	0.986	1.10	-13.8	0.20718
01/14/19	257	GAO-35	UCLA-1A-1	*Eomycetopsis* sp.	-28.3	1.39	-41.9	2.74	2.4E+05	11%	0.9	0.986	1.10	-13.8	0.20718
AVERAGE					-29.7	0.95	-43.6	1.85	7.5E+05	27%	1.0	0.986	1.18	-14.1	0.21391
Kwagunt Formation															
05/25/18	29	KWAG-1A-1	C-W-1-B	*Eomycetopsis* sp.	-27.3	0.83	-43.1	1.58	6.6E+05	25%	1.1	0.984	1.08	-16.1	0.24212
05/25/18	30	KWAG-1B-1	C-W-1-B	*Eomycetopsis* sp.	-27.4	0.38	-43.3	0.59	5.0E+06	192%	1.1	0.984	1.08	-16.1	0.24212
05/25/18	32	KWAG-1B-3	C-W-1-B	*Eomycetopsis* sp.	-29.8	0.90	-45.7	1.74	5.0E+05	19%	1.1	0.984	1.08	-16.1	0.24212
05/25/18	33	KWAG-1C	C-W-1-B	*Eomycetopsis* sp.	-27.3	0.48	-43.1	0.83	1.7E+06	64%	1.1	0.984	1.08	-16.1	0.24212
05/25/18	34	KWAG-1C-2	C-W-1-B	*Eomycetopsis* sp.	-27.0	0.50	-42.8	0.88	1.6E+06	61%	1.1	0.984	1.08	-16.1	0.24212
05/25/18	35	KWAG-1D-2	C-W-1-B	*Eomycetopsis* sp.	-28.5	0.71	-44.4	1.33	1.6E+06	59%	1.1	0.984	1.08	-16.1	0.24212
05/25/18	36	KWAG-1D-3	C-W-1-B	*Eomycetopsis* sp.	-28.0	0.91	-43.8	1.74	3.5E+06	135%	1.1	0.984	1.08	-16.1	0.24212
05/25/18	37	KWAG-4	C-W-1-B	*Eomycetopsis* sp.	-27.1	0.90	-43.0	1.73	4.3E+05	16%	1.1	0.984	1.08	-16.1	0.24212
01/11/19	171	KWAG-1A-2	C-W-1-B	*Eomycetopsis* sp.	-31.6	0.70	-45.5	1.35	6.6E+05	17%	0.9	0.986	1.11	-14.2	0.19696
01/11/19	172	KWAG-1A-3	C-W-1-B	*Eomycetopsis* sp.	-32.3	1.10	-46.3	2.17	3.0E+05	8%	0.9	0.986	1.11	-14.2	0.19696
01/11/19	173	KWAG-1A-4	C-W-1-B	*Eomycetopsis* sp.	-30.5	0.92	-44.4	1.79	6.1E+05	16%	0.9	0.986	1.11	-14.2	0.19696
01/11/19	174	KWAG-1B-4	C-W-1-B	*Eomycetopsis* sp.	-30.8	1.14	-44.8	2.24	3.4E+05	9%	0.9	0.986	1.11	-14.2	0.19696
01/11/19	175	KWAG-1B-5	C-W-1-B	*Eomycetopsis* sp.	-30.1	0.85	-44.0	1.64	6.2E+05	16%	0.9	0.986	1.11	-14.2	0.19696
01/11/19	176	KWAG-1B-6	C-W-1-B	*Eomycetopsis* sp.	-30.4	0.51	-44.4	0.93	2.3E+06	58%	0.9	0.986	1.11	-14.2	0.19696
01/11/19	177	KWAG-1B-7	C-W-1-B	*Eomycetopsis* sp.	-30.0	0.76	-43.9	1.46	7.8E+05	20%	0.9	0.986	1.11	-14.2	0.19696
01/11/19	179	KWAG-2-1	C-W-1-B	*Eomycetopsis* sp.	-26.7	0.70	-40.7	1.35	6.9E+05	18%	0.9	0.986	1.11	-14.2	0.19696
01/11/19	181	KWAG-3	C-W-1-B	*Eomycetopsis* sp.	-28.2	0.72	-42.2	1.38	4.9E+05	13%	0.9	0.986	1.11	-14.2	0.19696
01/11/19	182	KWAG-BG2-1	C-W-1-B	Background kerogen	-26.4	1.71	-40.4	3.40	2.2E+05	6%	0.9	0.986	1.11	-14.2	0.19696
01/11/19	183	KWAG-BG2-2	C-W-1-B	Background kerogen	-22.4	1.04	-36.5	2.03	2.3E+05	6%	0.9	0.986	1.11	-14.2	0.19696
01/11/19	184	KWAG-BG2-3	C-W-1-B	Background kerogen	-26.1	2.50	-40.1	4.98	1.2E+05	3%	0.9	0.986	1.11	-14.2	0.19696
01/11/19	185	KWAG-BG1-1	C-W-1-B	Background kerogen	-23.5	3.08	-37.6	6.14	1.4E+05	4%	0.9	0.986	1.11	-14.2	0.19696
01/11/19	186	KWAG-BG1-2	C-W-1-B	Background kerogen	-22.9	2.28	-36.9	4.54	8.8E+04	2%	0.9	0.986	1.11	-14.2	0.19696
AVERAGE					-27.9	1.07	-42.6	2.08	1.0E+06	32%	1.0	0.985	1.10	-14.9	0.21338

Table 2-1. Data from SIMS carbon isotope analyses of filamentous microfossils and associated background kerogen from the Kwagunt Formation and Gaoyuzhuang Formation.

* Internal precision is determined by calculating two standard errors (2SE) of the $\delta^{13}C$ values measured from 20 cycles for each analysis.

** External precision is determined by calculating two standard deviations (2SD) of the $\delta^{13}C$ values for bracketing standard analyses.

IMF – Instrumental mass fractionation

SEM – Standard error of the mean

Sample ID	$\delta^{13}C_{org}$ (VPDB, ‰)	Total organic carbon (TOC, mg/g)	Estimated Temperature (±30°C)[b]
PPRG-215	-31.5[a]	1.40[a]	375
FTS-1	-13.5	0.45	> 400

[a] Hayes et al. (1983)

[b] Kouketsu et al. (2014)

Table 2-2. Bulk geochemical data and estimated temperature for the two analytical standards used. The two PPRG-215 standards (PPRG-215-2a, PPRG-215-1/2) were made from the same sample as that used in previous SIMS studies of Precambrian microfossils (e.g., House et al., 2000, 2013; Williford et al., 2013). The new Fig Tree standards (FTS-1, FTS-2) were prepared from a recently collected sample of Fig Tree chert (see text for details).

FIGURES

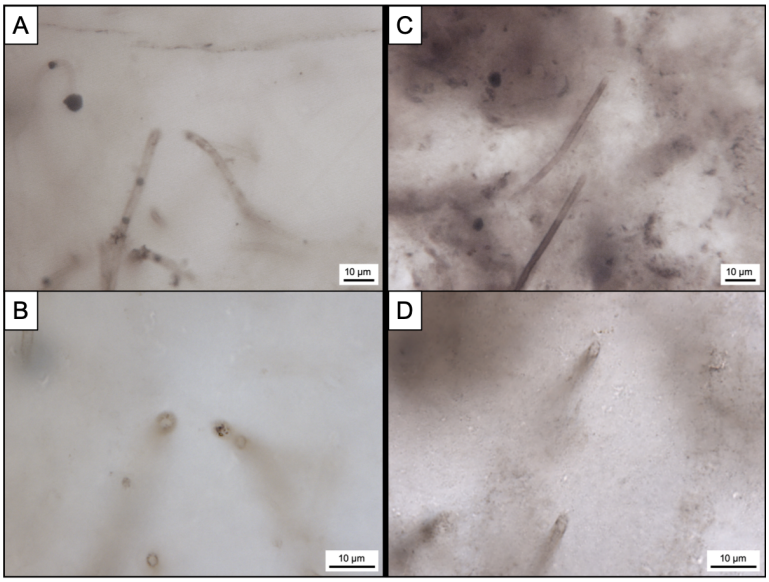

Figure 2-1. Transmitted light photomicrographs of permineralized kerogenous microfossil filaments (*Eomycetopsis* sp.) in petrographic thin sections of cherts from the Kwagunt Formation (A, B) and Gaoyuzhuang Formation (C, D). The photomicrographs in B and D illustrate the three-dimensional preservation of the fossils exposed at thin section surfaces, whereas the composite photomontages of stacked images (A, C) illustrate the filamentous morphology of multiple microfossils within the field of view.

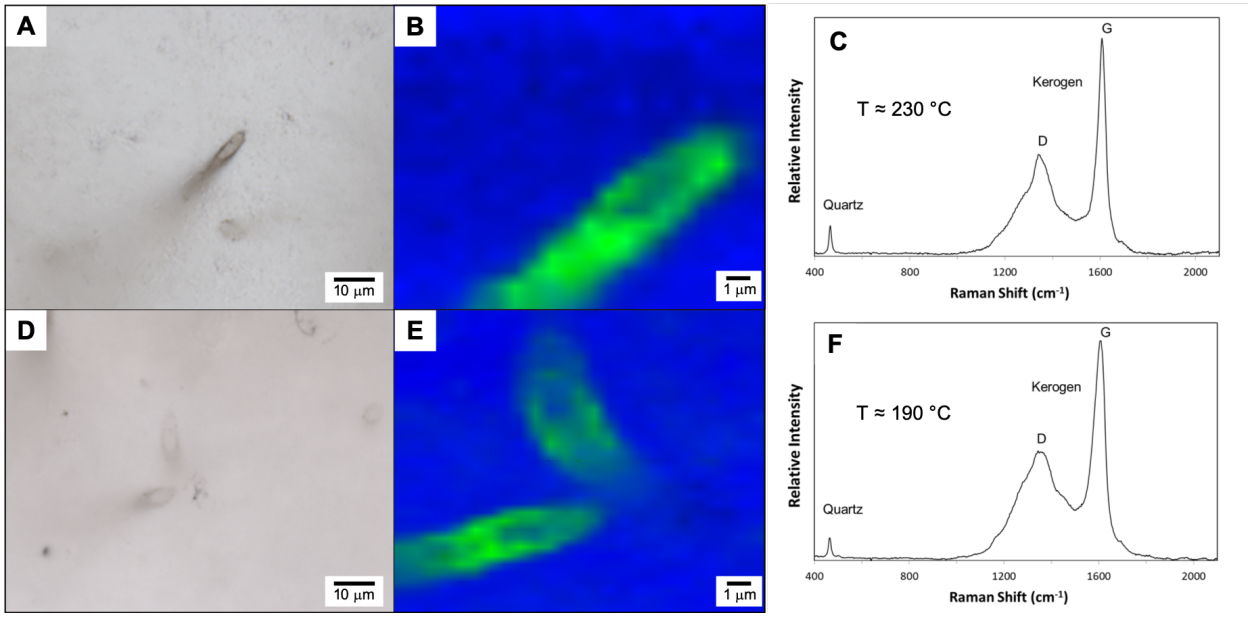

Figure 2-2. Representative transmitted light photomicrographs (A, D), 2-D Raman images (B, E), and Raman spectra (C, F; normalized to the kerogen G-band) of typical fossil filaments from the Gaoyuzhuang (A, B, C) and Kwagunt (D, E, F) cherts. The 2-D Raman geochemical images (B, E) show the distribution of kerogen comprising the walls of the permineralized fossils (green) relative to the filament-infilling and background quartz matrix (blue). The kerogen Raman spectra (C, F) consist of two bands, the "disordered" D-band (~1,350 cm^{-1}) and the "graphitic" G-band (~1,600 cm^{-1}), and showing estimated peak metamorphic temperatures; the quartz peak in each spectrum (465 cm^{-1}) is derived from the fossil-encompassing and -infilling chert matrix.

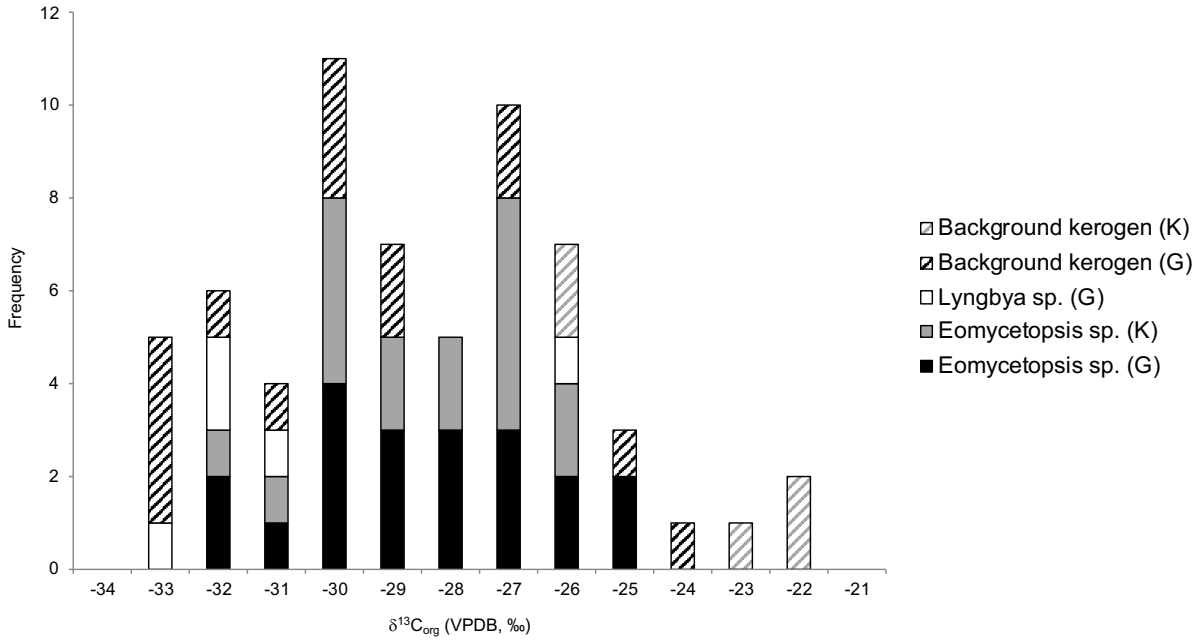

Figure 2-3. Histogram of SIMS carbon isotope data for samples from the Gaoyuzhuang (G) and Kwagunt (K) Formations, with $\delta^{13}C_{org}$ values placed into 1‰ bins. Solid bars (black, grey, white) represent microfossil analyses, and dashed bars (black, grey) show distribution of SIMS data for associated background kerogen.

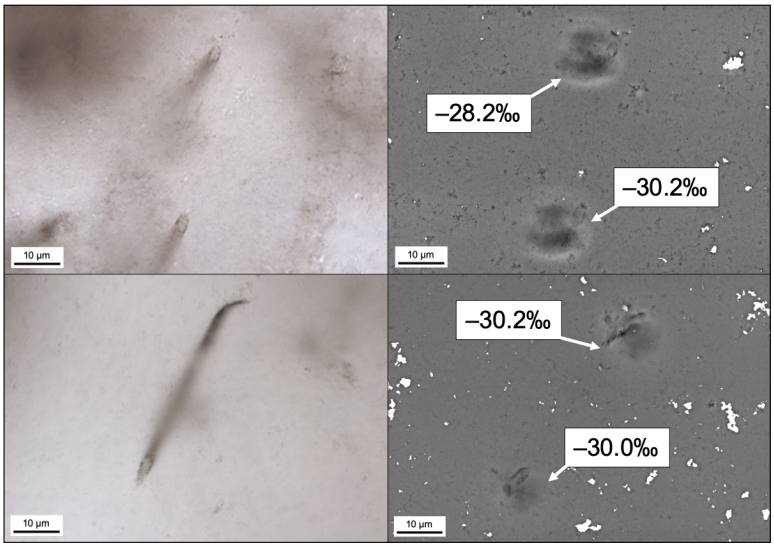

Figure 2-4. Transmitted light (left) and backscattered electron (right) images of representative *Eomycetopsis* specimens from the Gaoyuzhuang chert analyzed with SIMS at the thin section surface showing the $\delta^{13}C_{org}$ values (‰) measured in the ~10 µm-diameter analytical pits.

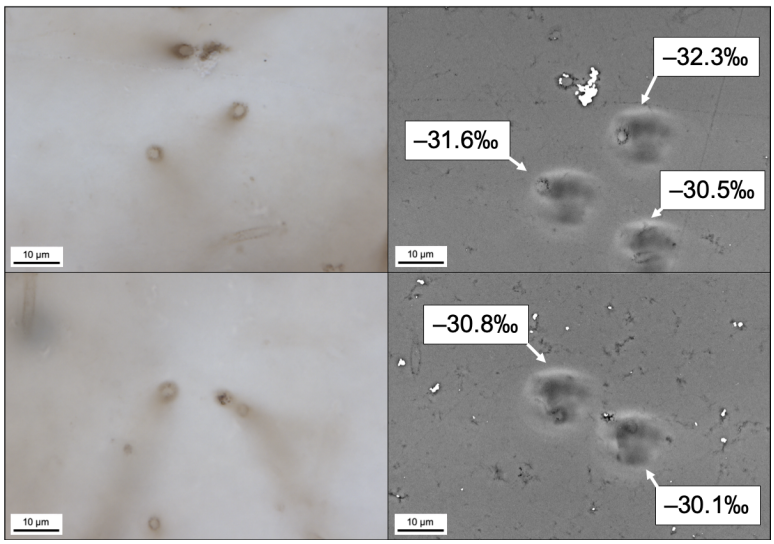

Figure 2-5. Transmitted light (left) and backscattered electron (right) images of representative *Eomycetopsis* specimens from the Kwagunt chert analyzed with SIMS at the thin section surface showing the $\delta^{13}C_{org}$ values (‰) measured in the ~10 µm-diameter analytical pits.

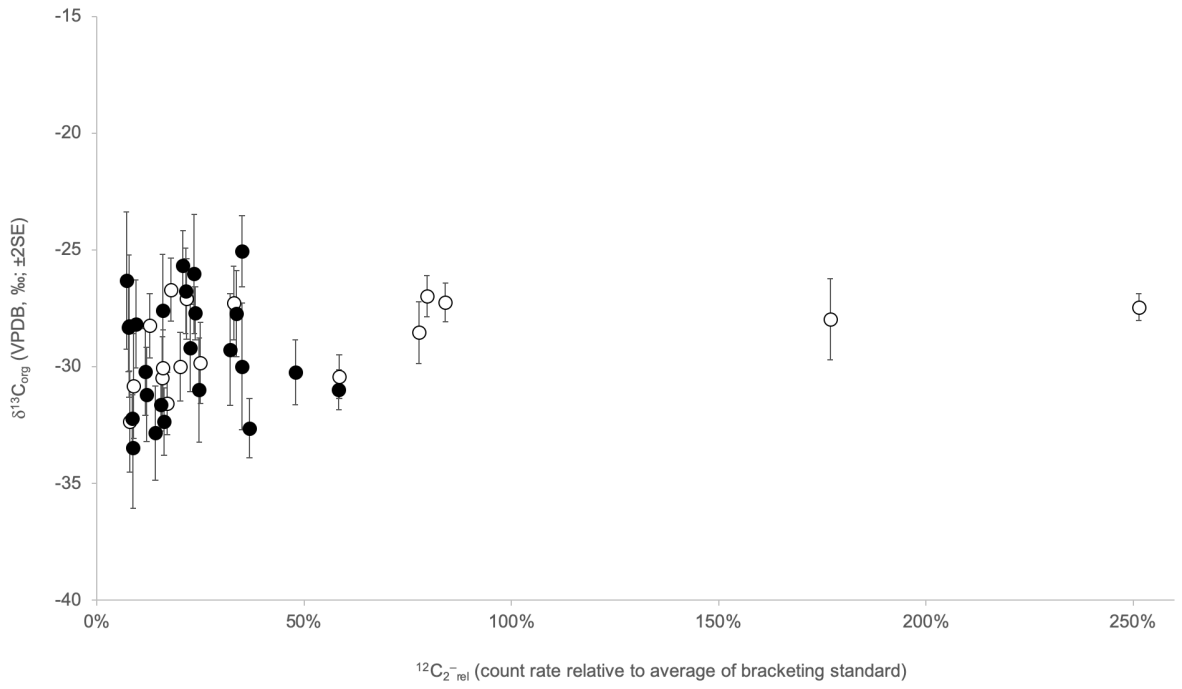

Figure 2-6. SIMS carbon isotope ($\delta^{13}C_{org}$) data for analyses of *Eomycetopsis* and *Lyngbya*-like filamentous microfossils from the Gaoyuzhuang Formation (closed circles) and *Eomycetopsis* fossils of the Kwagunt Formation (open circles) versus $^{12}C_2^-$ count rate relative to the average count rate for the bracketing standards ($^{12}C_2^-{}_{rel}$, %). Error bars represent internal precision (±2SE).

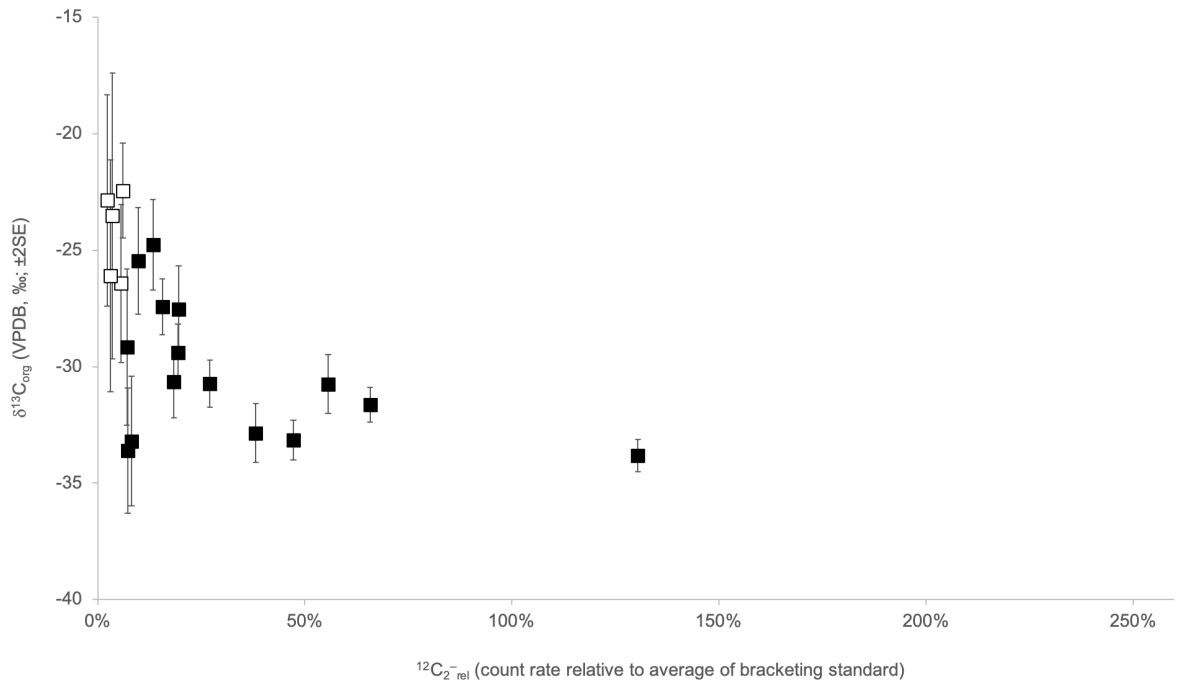

Figure 2-7. SIMS carbon isotope ($\delta^{13}C_{org}$) data for background kerogen analyses from the Gaoyuzhuang Formation (closed squares) and Kwagunt Formation (open squares) versus $^{12}C_2^-$ count rate relative to the average count rate for the bracketing standards ($^{12}C_{2\,rel}^-$, %). Error bars represent internal precision (±2SE).

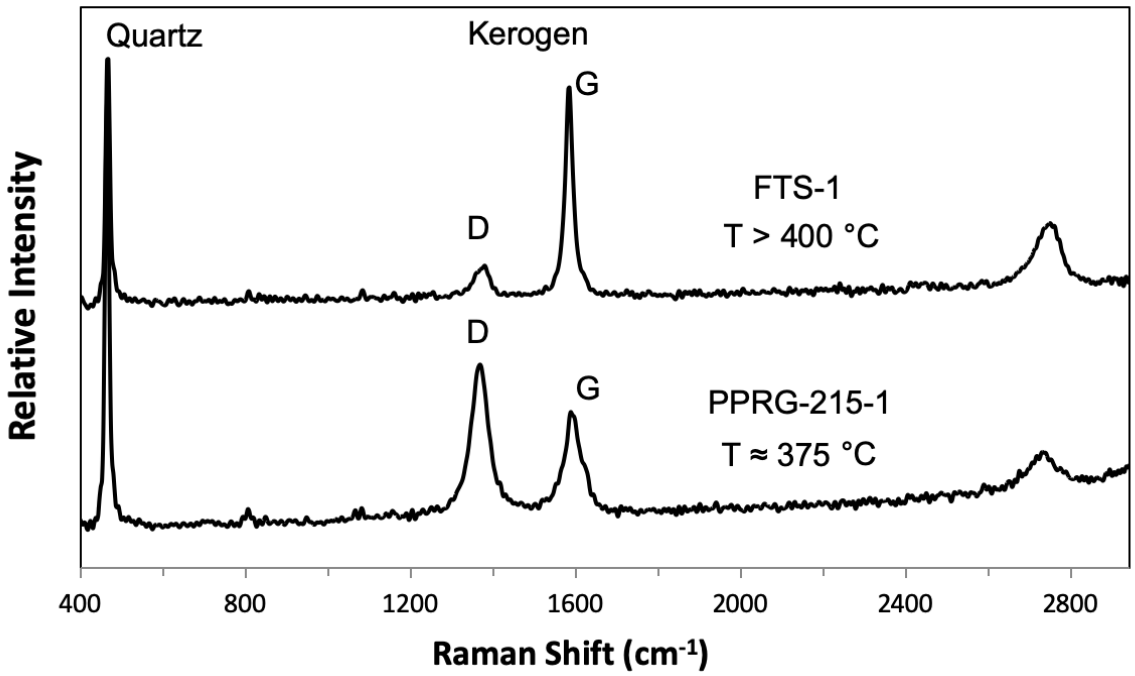

Figure 2-8. Raman spectra of particulate kerogen from the newly prepared standards FTS-1 (top) and PPRG-215-1/2 (bottom) from carbonaceous cherts of the 3,350-Ma-old Fig Tree Group, South Africa. The spectra are shown along with estimated peak metamorphic temperatures and consist of two first-order kerogen bands, the "disordered" D-band (~1,350 cm^{-1}) and the "graphitic" G-band (~1,600 cm^{-1}); a second-order band (~2,700 cm^{-1}) typical of mature kerogen; the quartz peak in each spectrum (465 cm^{-1}) is derived from the chert matrix.

REFERENCES

Anbar, A. D., Duan, Y., Lyons, T. W., Arnold, G. L., Kendall, B., Creaser, R. A., Kaufman, A. J., Gordon, G. W., Scott, C., Garvin, J., & Buick, R. (2007). A whiff of oxygen before the Great Oxidation Event? *Science*, *317*, 1903–1906.

Awramik, S. M. (1992). The oldest records of photosynthesis. *Photosynthesis Research*, *33*, 75–89.

Awramik, S. M., Schopf, J. W., & Walter, M. R. (1983). Filamentous fossil bacteria from the Archean of Western Australia. In B. Nagy, R. Weber, J. C. Guerrero, & M. Schidlowski (Eds.) *Developments in Precambrian Geology,* Vol. 7 (pp. 249-266). USA: Elsevier.

Badger, M. R., & Price, G. D. (2003). CO_2 concentrating mechanisms in cyanobacteria: molecular components, their diversity and evolution. *Journal of Experimental Botany*, *54*, 609–622.

Bartley, J. K. (1996). Actualistic taphonomy of cyanobacteria: implications for the Precambrian fossil record. *Palaios, 11*, 571–586.

Beerling, D. J. (2001). Carbon isotopes in plants. In D. E. Briggs, & P. R. Crowther (Eds.), *Palaeobiology II* (pp. 473–475). USA: Blackwell Publishing.

Bloeser, B. (1985). *Melanocyrillium*, a new genus of structurally complex late Proterozoic microfossils from the Kwagunt Formation (Chuar Group), Grand Canyon, Arizona. *Journal of Paleontology*, *59,* 741–765.

Bosak, T., Liang, B., Sim, M. S., & Petroff, A. P. (2009). Morphological record of oxygenic photosynthesis in conical stromatolites. *Proceedings of the National Academy of Sciences USA, 106*, 10939–10943.

Buick, R. (1992). The antiquity of oxygenic photosynthesis: evidence from stromatolites in sulphate-deficient Archaean lakes. *Science*, *255*, 74–77.

Buick, R. (2008). When did oxygenic photosynthesis evolve? *Philosophical Transactions of the Royal Society of London, Series B*, *Biological Sciences*, *363*, 2731–2743.

Burns, B. P., Goh, F., Allen, M., & Neilan, B. A. (2004). Microbial diversity of extant stromatolites in the hypersaline marine environment of Shark Bay, Australia. *Environmental Microbiology*, *6*, 1096–1101.

Butterfield, N. J. (2015). Proterozoic photosynthesis–a critical review. *Palaeontology*, *58*, 953–972.

Cassar, N., Laws, E. A., & Popp, B. N. (2006). Carbon isotopic fractionation by the marine diatom *Phaeodactylum tricornutum* under nutrient- and light-limited growth conditions. *Geochimica et Cosmochimica Acta*, *70,* 5323–5335.

Chang, T., & Li, W. (1990). A calibrated measurement of the atomic weight of carbon. *Chinese Science Bulletin*, *35*, 290–296.

Chu, X., Zhang, T., Zhang, Q., Feng, L., & Zhang, F. (2004). Carbon isotopic variations of Proterozoic carbonates in Jixian, Tianjin, China. *Science in China Series D: Earth Sciences*, *47*, 160–170.

Chu, X., Zhang, T., Zhang, Q., & Lyons, T. W. (2007). Sulfur and carbon isotope records from 1700 to 800 Ma carbonates of the Jixian section, northern China: Implications for secular isotope variations in Proterozoic seawater and relationships to global supercontinental events. *Geochimica et Cosmochimica Acta*, *71*, 4668–4692.

Cohen, Y., Padan, E., & Shilo, M. (1975). Sulfide-dependent anoxygenic photosynthesis in the cyanbacterium *Oscillatoria limnetica*. *Nature*, *257*, 489–492.

Cohen, Y., Jorgensen, B. B., Revsbech, N. P., & Poplawski, R. (1986). Adaptation to hydrogen sulfide of oxygenic and anoxygenic photosynthesis among cyanobacteria. *Applied and Environmental Microbiology*, *51*, 398–407.

DeNiro, M. J., & Epstein, S. (1978). Influence of diet on the distribution of carbon isotopes in animals. *Geochimica et Cosmochimica Acta*, *42*, 495–506.

Des Marais, D. J. (1997). Isotopic evolution of the biogeochemical carbon cycle during the Proterozoic Eon. *Organic Geochemistry*, *27*, 185–193.

Des Marais, D. J. (2001). Isotopic evolution of the biogeochemical carbon cycle during the Precambrian. *Reviews in Mineralogy and Geochemistry*, *43*, 555–578.

Farquhar, G. D., & Lloyd, J. (1993). Carbon and oxygen isotope effects in the exchange of carbon dioxide between terrestrial plants and the atmosphere. In J. R. Ehleringer, A. E. Hall, & G. D. Farquhar (Eds.), *Stable isotopes and plant carbon-water relations* (pp. 47–70). USA: Academic Press.

Farquhar, G. D., Ehleringer, J. R., & Hubick, K. T. (1989). Carbon isotope discrimination and photosynthesis. *Annual Review of Plant Physiology and Plant Molecular Biology*, *40*, 503–537.

Ford, T. D., & Breed, W. J. (1973). Late Precambrian Chuar Group, Grand Canyon, Arizona. *Geological Society of America Bulletin*, *84*, 1243–1260.

Freeman, K. H., & Hayes, J. M. (1992). Fractionation of carbon isotopes by phytoplankton and estimates of ancient CO_2 levels. *Global Biogeochemical Cycles*, *6*, 185–198.

Fuchs, G., Thauer, R., Ziegler, H., & Stichler, W. (1979). Carbon isotope fractionation by *Methanobacterium thermoautotrophicum*. *Archives of Microbiology*, *120*, 135–139.

Garcia, A. K., Schopf, J. W., Yokobori, S. I., Akanuma, S., & Yamagishi, A. (2017). Reconstructed ancestral enzymes suggest long-term cooling of Earth's photic zone since the Archean. *Proceedings of the National Academy of Sciences USA*, *114*, 4619–4624.

Golubic, S., & Seong-Joo, L. (1999). Early cyanobacterial fossil record: preservation, palaeoenvironments and identification. *European Journal of Phycology*, *34*, 339–348.

Grotzinger, J. P., & Knoll, A. H. (1999). Stromatolites in Precambrian carbonates: evolutionary mileposts or environmental dipsticks? *Annual Review of Earth and Planetary Sciences*, *27*, 313–358.

Guo, H., Du, Y., Kah, L. C., Huang, J., Hu, C., Huang, H., & Yu, W. (2013). Isotopic composition of organic and inorganic carbon from the Mesoproterozoic Jixian Group, North China: Implications for biological and oceanic evolution. *Precambrian Research*, *224*, 169–183.

Guy, R. D., Fogel, M. L., & Berry, J. A. (1993). Photosynthetic fractionation of the stable isotopes of oxygen and carbon. *Plant Physiology*, *101*, 37–47.

Hayes, J. M. (1993). Factors controlling ^{13}C contents of sedimentary organic compounds: principles and evidence. *Marine Geology*, *113*, 111–125.

Hayes, J. M. (2001). Fractionation of carbon and hydrogen isotopes in biosynthetic processes. *Reviews in Mineralogy and Geochemistry*, *43*, 225–277.

Hayes, J. M., Kaplan, I. R., & Wedeking, K. W. (1983). Precambrian organic geochemistry, preservation of the record. In J. W. Schopf (Ed.), *The Earth's Earliest Biosphere: Its Origin and Evolution* (pp. 93–134). USA: Princeton University Press.

Hayes, J. M., Strauss, H., & Kaufman, A. J. (1999). The abundance of ^{13}C in marine organic matter and isotopic fractionation in the global biogeochemical cycle of carbon during the past 800 Ma. *Chemical Geology*, *161*, 103–125.

Hongwei, K., Yongqing, L., Jiahua, L., Nan, P., Shunshe, L., & Chao, C. (2011). Carbon and oxygen isotopic stratigraphy of Mesoproterozoic carbonate sequences (1.6–1.4 Ga) from Yanshan in North China. *International Journal of Oceanography*, *2011*, 1–11.

House, C. H., Schopf, J. W., McKeegan, K. D., Coath, C. D., Harrison, T. M., & Stetter, K. O. (2000). Carbon isotopic composition of individual Precambrian microfossils. *Geology*, *8*, 707–710.

House, C. H., Oehler, D. Z., Sugitani, K., & Mimura, K. (2013). Carbon isotopic analyses of ca. 3.0 Ga microstructures imply planktonic autotrophs inhabited Earth's early oceans. *Geology*, *41*, 651–654.

Jardine, T. D., & Cunjak, R. A. (2005). Analytical error in stable isotope ecology. *Oecologia*, *144*, 528–533.

Javaux, E. J., & Lepot, K. (2018). The Paleoproterozoic fossil record: Implications for the evolution of the biosphere during Earth's middle-age. *Earth-Science Reviews*, *176*, 68–86.

Johnston, D. T., Wolfe-Simon, F., Pearson, A., & Knoll, A. H. (2009). Anoxygenic photosynthesis modulated Proterozoic oxygen and sustained Earth's middle age. *Proceedings of the National Academy of Sciences USA*, *106*, 16925–16929.

Johnston, D. T., Macdonald, F. A., Gill, B. C., Hoffman, P. F., & Schrag, D. P. (2012). Uncovering the Neoproterozoic carbon cycle. *Nature*, *483*, 320–323.

Karlstrom, K. E., Bowring, S. A., Dehler, C. M., Knoll, A. H., Porter, S. M., Des Marais, D. J., Weil, A. B., Sharp, Z. D., Geissman, J. W., Elrick, M. B., Timmons, J. M., Crossey, L. J., & Davidek, K. L. (2000). Chuar Group of the Grand Canyon: Record of breakup of Rodinia, associated change in the global carbon cycle, and ecosystem expansion by 740 Ma. *Geology*, *28*, 619–622.

Kaufman, A. J., & Xiao, S. (2003). High CO_2 levels in the Proterozoic atmosphere estimated from analyses of individual microfossils. *Nature*, *425*, 279–282.

Kaufman, A. J., Johnston, D. T., Farquhar, J., Masterson, A. L., Lyons, T. W., Bates, S., Anbar, A. D., Arnold, G. L., Garvin, J., & Buick, R. (2007). Late Archean biospheric oxygenation and atmospheric evolution. *Science*, *317*, 1900–1903.

Kita, N. T., Ushikubo, T., Fu, B., & Valley, J. W. (2009). High precision SIMS oxygen isotope analysis and the effect of sample topography. *Chemical Geology*, *264*, 43–57.

Klein, C., Beukes, N. J., & Schopf, J. W. (1987). Filamentous microfossils in the early Proterozoic Transvaal Supergroup: their morphology, significance, and paleoenvironmental setting. *Precambrian Research*, *36*, 81–94.

Knauth, L. P. (2005). Temperature and salinity history of the Precambrian ocean: Implications for the course of microbial evolution. *Palaeogeography, Palaeoclimatology, Palaeoecology*, *219*, 53–69.

Knoll, A. H. (1985). The distribution and evolution of microbial life in the Late Proterozoic era. *Annual Review of Microbiology*, *39*, 391–417.

Knoll, A. H. (2012). The fossil record of microbial life. In A. H. Knoll, D. E. Canfield, & K. O. Konhauser (Eds.), *Fundamentals of Geobiology* (pp. 297–314). USA: Blackwell Publishing Ltd.

Knoll, A. H., Swett, K., & Burkhardt, E. (1989). Paleoenvironmental distribution of microfossils and stromatolites in the Upper Proterozoic Backlundtoppen Formation, Spitsbergen. *Journal of Paleontology*, *63*, 129–145.

Kouketsu, Y., Mizukami, T., Mori, H., Endo, S., Aoya, M., Hara, H., Nakamura, D., & Wallis, S. (2014). A new approach to develop the Raman carbonaceous material geothermometer for low-grade metamorphism using peak width. *Island Arc*, *23*, 33–50.

Kremer, B., Kazmierczak, J., Łukomska-Kowalczyk, M., & Kempe, S. (2012). Calcification and silicification: fossilization potential of cyanobacteria from stromatolites of Niuafo‘ou’s Caldera Lakes (Tonga) and implications for the early fossil record. *Astrobiology*, *12*, 535–548.

Laws, E. A., Popp, B. N., Bidigare, R. R., Kennicutt, M. C., & Macko, S. A. (1995). Dependence of phytoplankton carbon isotopic composition on growth rate and $[CO_2]_{aq}$: Theoretical considerations and experimental results. *Geochimica et Cosmochimica Acta*, *59*, 1131–1138.

Laws, E. A., Bidigare, R. R., & Popp, B. N. (1997). Effect of growth rate and CO_2 concentration on carbon isotopic fractionation by the marine diatom *Phaeodactylum tricornutum*. *Limnology and Oceanography*, *42*, 1552–1560.

Li, H. K., Zhu, S. X., Xiang, Z. Q., Su, W. B., Lu, S. N., Zhou, H. Y., Geng, J. Z., Li, S., & Yang, F. J. (2010). Zircon U–Pb dating on tuff bed from Gaoyuzhuang Formation in Yanqing, Beijing:

further constraints on the new subdivision of the Mesoproterozoic stratigraphy in the northern North China Craton. *Acta Petrologica Sinica*, *26*, 2131–2140 (in Chinese with English abstract).

Lu, S. N., & Li, H. M. (1991). A precise U-Pb single zircon age determination for the volcanics of Dahongyu Formation, Changcheng System in Jixian. *Bulletin of the Chinese Academy of Geological Sciences*, *22*, 137–145.

Meng, Q. R., Wei, H. H., Qi, Y. Q., & Ma, S. X. (2011). Stratigraphic and sedimentary records of the rift to drift evolution of the northern North China craton at the Paleo- to Mesoproterozoic transition. *Gondwana Research*, *20*, 205–218.

Moore, T. B., & Schopf, J. W. (1992). Geographic and geologic data for PPRG rock samples. In J. W. Schopf, & C. Klein (Eds.) *The Proterozoic Biosphere, A Multidisciplinary Study* (pp. 603–693). USA: Cambridge University Press.

Nisbet, E. G., Grassineau, N. V., Howe, C. J., Abell, P. I., Regelous, M., & Nisbet, R. E. R. (2007). The age of Rubisco: The evolution of oxygenic photosynthesis. *Geobiology*, *5*, 311–335.

Orphan, V. J., & House, C. H. (2009). Geobiological investigations using secondary ion mass spectrometry: microanalysis of extant and paleo-microbial processes. *Geobiology*, *7*, 360–372.

Padan, E. (1979). Facultative anoxygenic photosynthesis in cyanobacteria. *Annual Review of Plant Physiology*, *30*, 27–40.

Popp, B. N., Laws, E. A., Bidigare, R. R., Dore, J. E., Hanson, K. L., & Wakeham, S. G. (1998). Effect of phytoplankton cell geometry on carbon isotopic fractionation. *Geochimica et Cosmochimica Acta*, *62*, 69–77.

Preuβ, A., Schauder, R., Fuchs, G., & Stichler, W. (1989). Carbon isotope fractionation by autotrophic bacteria with 3 different CO_2 fixation pathways. *Zeitschrift für Naturforschung C: Journal of Bioscience*, *44*, 397–402.

Reid, R. P., Visscher, P. T., Decho, A. W., Stolz, J. F., Bebout, B. M., Dupraz, C., Macintyre, I. G., Paerl, H. W., Pinckney, J. L., Prufert-Bebout, L., & Steppe, T. F. (2000). The role of microbes in accretion, lamination and early lithification of modern marine stromatolites. *Nature*, *406*, 989–992.

Roeske, C. A., & O'Leary, M. H. (1985). Carbon isotope effect on carboxylation of ribulose bisphosphate catalyzed by ribulose bisphosphate carboxylase from *Rhodospirillum rubrum*. *Biochemistry*, *24*, 1603–1607.

Schidlowski, M. (2001). Carbon isotopes as biogeochemical recorders of life over 3.8 Ga of Earth history: evolution of a concept. *Precambrian Research*, *106*, 117–134.

Schidlowski, M., Hayes, J., & Kaplan, I. (1983). Isotopic inferences of ancient biochemistries: carbon, sulfur, hydrogen, and nitrogen. In J. W. Schopf (Ed.), *Earth's Earliest Biosphere, Its Origin and Evolution* (pp. 149–185). USA: Princeton University Press.

Schiffbauer, J. D., Wallace, A. F., Hunter Jr., J. L., Kowalewski, M., Bodnar, R. J., Xiao, S. (2012). Thermally-induced structural and chemical alteration of organic-walled microfossils: an experimental approach to understanding fossil preservation in metasediments. *Geobiology*, *10*, 402–423.

Schopf, J. W. (1968). Microflora of the Bitter Springs formation, late Precambrian, central Australia. *Journal of Paleontology*, *42,* 651–688.

Schopf, J. W. (1992). Proterozoic prokaryotes: affinities, geologic distribution, and evolutionary trends. In J. W. Schopf, & C. Klein (Eds.), *The Proterozoic Biosphere: A Multidisciplinary Study* (pp. 195–218). USA: Cambridge University Press.

Schopf, J. W. (1994). Disparate rates, differing fates: The rules of evolution changed from the Precambrian to the Phanerozoic. *Proceedings of the National Academy of Sciences USA*, *91,* 6735–6742.

Schopf, J. W. (2011). The paleobiological record of photosynthesis. *Photosynthesis Research*, *107*, 87–101.

Schopf, J. W. (2019). *Life in Deep Time: Darwin's "Missing" Fossil Record, A Personal Account of Paradigm-Changing Science*. CRC Press, Florida.

Schopf, J. W., & Sovietov, Y. K. (1976). Microfossils in *Conophyton* from the Soviet Union and their bearing on Precambrian biostratigraphy. *Science*, *193*, 143–146.

Schopf, J. W., Ford, T. D., & Breed, W. J. (1973). Microorganisms from the late Precambrian of the Grand Canyon, Arizona. *Science*, *179*, 1319–1321.

Schopf, J. W., Zhu, W. Q., Xu, Z. L., & Hsu, J. (1984). Proterozoic stromatolitic microbiotas of the 1400–1500 Ma-old Gaoyuzhuang formation near Jixian, northern China. *Precambrian Research*, *24*, 335–349.

Schopf, J. W., Kudryavtsev, A. B., Agresti, D. G., Czaja, A. D., & Wdowiak, T. J. (2005). Raman imagery: a new approach to assess the geochemical maturity and biogenicity of permineralized Precambrian fossils. *Astrobiology*, *5*, 333–371.

Schopf, J. W., Kudryavtsev, A. B., Czaja, A. D., & Tripathi, A. B. (2007). Evidence of Archean life: Stromatolites and microfossils. *Precambrian Research*, *158*, 141–155.

Schopf, J. W., Kudryavtsev, A. B., Walter, M. R., Van Kranendonk, M. J., Williford, K. H., Kozdon, R., Valley, J. W., Gallardo, V. A., Espinoza, C., & Flannery, D. T. (2015). Sulfur-cycling

fossil bacteria from the 1.8-Ga Duck Creek Formation provide promising evidence of evolution's null hypothesis. *Proceedings of the National Academy of Sciences USA*, *112*, 2087–2092.

Schopf, J. W., Kitajima, K., Spicuzza, M. J., Kudryavtsev, A. B., & Valley, J. W. (2018). SIMS analyses of the oldest known assemblage of microfossils document their taxon-correlated carbon isotope compositions. *Proceedings of the National Academy of Sciences USA*, *115*, 53–58.

Sergeev, V. N., Sharma, M., & Shukla, Y. (2012). Proterozoic fossil cyanobacteria. *The Palaeobotanist*, *61*, 189–358.

Strauss, H., & Moore, T. B. (1992). Abundances and isotopic compositions of carbon and sulfur species in whole rock and kerogen samples. In J. W. Schopf, & C. Klein (Eds.), *The Proterozoic Biosphere: A Multidisciplinary Study* (pp. 709–798). USA: Cambridge University Press.

Strauss, H., Des Marais, D. J., Hayes, J. M., Lambert, I. B., & Summons, R. E. (1992a). Procedures of whole rock and kerogen analysis. In J. W. Schopf, & C. Klein (Eds.), *The Proterozoic Biosphere: A Multidisciplinary Study* (pp. 699–707). USA: Cambridge University Press.

Strauss, H., Des Marais, D. J., Summons, R. E., & Hayes, J. M. (1992b). The carbon isotopic record. In J. W. Schopf, & C. Klein (Eds.), *The Proterozoic Biosphere: A Multidisciplinary Study* (pp. 117–128). USA: Cambridge University Press.

Summons, R. E., Brassell, S. C., Eglinton, G., Evans, E., Horodyski, R. J., Robinson, N., & Ward, D. M. (1988). Distinctive hydrocarbon biomarkers from fossiliferous sediment of the Late Proterozoic Walcott Member, Chuar Group, Grand Canyon, Arizona. *Geochimica et Cosmochimica Acta*, *52*, 2625–2637.

Swett, K., & Knoll, A. H. (1989). Marine pisolites from upper Proterozoic carbonates of East Greenland and Spitsbergen. *Sedimentology*, *36*, 75–93.

Tice, M. M., Bostick, B. C., & Lowe, D. R. (2004). Thermal history of the 3.5–3.2 Ga Onverwacht and Fig Tree Groups, Barberton greenstone belt, South Africa, inferred by Raman microspectroscopy of carbonaceous material. *Geology*, *32*, 37–40.

Ueno, Y., Isozaki, Y., Yurimoto, H., & Maruyama, S. (2001). Carbon isotopic signatures of individual Archean microfossils(?) from Western Australia. *International Geology Review*, *43*, 196–212.

Walsh, M. M., & Lowe, D. R. (1985). Filamentous microfossils from the 3,500-Myr-old Onverwacht Group, Barberton Mountain Land, South Africa. *Nature*, *314*, 530–532.

Walter, M. R., Hofmann, H. J., & Schopf, J. W. (1983). Geographic and geologic data for processed rock samples. In J. W. Schopf (Ed.), *Earth's Earliest Biosphere, Its Origin and Evolution* (p. 392). USA: Princeton University Press.

Williford, K. H., Ushikubo, T., Schopf, J. W., Lepot, K., Kitajima, K., & Valley, J. W. (2013). Preservation and detection of microstructural and taxonomic correlations in the carbon isotopic compositions of individual Precambrian microfossils. *Geochimica et Cosmochimica Acta*, *104*, 165–182.

Zerkle, A. L., House, C. H., & Brantley, S. L. (2005). Biogeochemical signatures through time as inferred from whole microbial genomes. *American Journal of Science*, *305*, 467–502.

Zhang, Y. (1981). Proterozoic stromatolite microfloras of the Gaoyuzhuang Formation (Early Sinian: Riphean), Hebei, China. *Journal of Paleontology*, 55, 485–506.

Chapter 3

Thermal alteration of Precambrian microfossils and the search for signs of early life on Earth

Jeffrey T. Osterhout, J. William Schopf, Kenneth H. Williford, Anatoliy B. Kudryavtsev, Kevin D. McKeegan, Ming-Chang Liu

1. INTRODUCTION

The search for evidence of Precambrian life on Earth has traditionally focused on the detection and characterization of fossilized microbial mats (e.g., stromatolites) preserved in sedimentary rocks, and of any microscopic fossils (microfossils) they may contain (Westall, 2004; Schopf et al., 2007; Knoll et al., 2016). In addition to these distinctive morphological features, signs of life in Precambrian deposits can be investigated using geochemical techniques to determine the molecular structure and stable isotopic composition of macromolecular organic matter (i.e., kerogen), and possibly other co-occurring more soluble and less stable organic compounds. Currently, the oldest well-established carbonaceous microfossils, including taxa that exhibit carbon isotope ($\delta^{13}C$) signatures typical of prokaryotic microorganisms (Schopf, 1993; Schopf et al., 2018), are known from the ~3.465 Ga Apex chert of northwestern Australia. Additional morphological structures, both stromatolites and microfossils, have been reported from slightly younger rocks of the ~3.426–3.350 Ga Strelley Pool Formation of Western Australia (e.g., Allwood et al., 2006a; Sugitani et al., 2010; Wacey et al., 2012) and the ~3.547-3.260 Ga Barberton Greenstone Belt of South Africa (e.g., Byerly et al., 1986; Walsh, 1992; Westall et al., 2001). The

kerogenous components of the prominent stromatolitic strata from these Archean units exhibit $\delta^{13}C$ signatures evidencing the presence of ancient microbial life (Ueno et al., 2001; Marshall et al., 2007; Lepot et al., 2013; Flannery et al., 2018), and although the occurrence of organic-walled microfossils and unequivocal stromatolites has not been established in older (and often more altered) sedimentary rocks – such as those of the ~3.7-3.8 Ga Isua Supracrustal Group of southwestern Greenland (e.g., Allwood et al., 2018) – recent analyses including Raman spectroscopy and secondary ion mass spectrometry (SIMS) measurements have firmly established the presence of potentially biogenic reduced carbon (kerogen and graphite) in such metasedimentary rocks and minerals (e.g., Bell et al., 2015; Foucher et al., 2015). These findings have identified a growing need for direct comparisons of stable carbon isotope compositions and geothermal maturity in sedimentary rocks containing putative evidence of ancient microbial life.

Stable carbon isotope analyses of carbonaceous matter performed on geologic samples dating up to ~4.1 Ga have yielded isotopically "light" (^{13}C-depleted compared to a terrestrial standard) $\delta^{13}C$ values that might represent evidence of biologically-produced organic matter (Mojzsis et al., 1996; Ueno et al., 2002; McKeegan et al., 2007; Ohtomo et al., 2014; Bell et al., 2015; Tashiro et al., 2017). Such measurements include those of earlier bulk (i.e., 1-kg whole-rock) analyses (Schidlowski et al., 1979, 1983; Hayes et al., 1983) and more recent SIMS measurements of microscopically preserved graphite particles contained within particular minerals, most notably grains of apatite (Mojzsis et al., 1996; McKeegan et al., 2007) and zircon (Bell et al., 2015), as well as other diverse mineral assemblages within metasedimentary rocks (Ueno et al., 2002; Ohtomo et al., 2014; Tashiro et al., 2017). Ion microprobe analyses of carbon isotopes in younger, better preserved Precambrian microfossils and kerogen (House et al., 2000, 2013; Williford et al., 2013; Peng et al., 2016; Ishida et al., 2018) serve as a valuable reference for

interpreting measurements of older Precambrian, Archean (or Hadean) samples (Lepot et al., 2013; Oehler et al., 2017; Flannery et al., 2018; Schopf et al., 2018). Such studies of ancient microfossils and kerogen emphasize the significance of characterizing geochemical signatures within their proper geologic context, with particular attention to the thermal history of the sedimentary rock unit investigated.

Thermal alteration of Precambrian sedimentary rocks can greatly affect the molecular structure and stable carbon isotope composition of preserved organic matter (Oehler et al., 1972; McKirdy and Powell, 1974; Des Marais, 2001; Schidlowski, 2001), although the degree of isotopic fractionation due to increasing thermal maturity remains poorly constrained and varies among different lithologies and minerals (e.g., Schidlowski et al., 1979, 1983; Van Zuilen et al., 2002; Tashiro et al., 2017; Osterhout et al., 2019). Such thermal effects were first reported by Hayes et al. (1983) based on bulk carbon isotope measurements of kerogen and graphite from the Isua Greenstone Belt of West Greenland, which revealed relatively "heavy" (^{13}C-enriched) carbon isotope values of $\delta^{13}C_{org} = -15.3 \pm 6‰$ (Schidlowski et al., 1979) and $-17.5 \pm 5‰$ (Hayes et al., 1983) in comparison with the ca. –20 to –40‰ range of $\delta^{13}C_{org}$ typically observed for kerogen extracted from younger Archean and Proterozoic rocks (Schidlowski, 2001). This seminal observation called into question the reliability of measurements of carbon isotopes in ancient sedimentary rocks that have experienced significant thermal alteration and/or metamorphism.

The Isua metasediments studied by Schidlowski et al. (1979) and Hayes et al. (1983) notably experienced high-temperature metamorphism ranging from upper greenschist to amphibolite facies (~450–650 °C) (Schidlowski, 2001; Rollinson, 2003). The reported "heavy" (^{13}C-enriched) $\delta^{13}C_{org}$ values have been attributed to isotopic re-equilibration between the carbon of coexisting organic matter (or graphite) and carbonate minerals, to the preferential breakage of

^{12}C–^{12}C bonds relative to ^{12}C–^{13}C bonds, and/or the concurrent release of isotopically "light" (^{13}C-depleted) alkyl groups and CH_4 resulting from the devolatization of kerogen (Hayes et al., 1983; Des Marais, 2001; Schidlowski, 2001). For lower temperatures, the metamorphic onset of the carbon isotopic alteration of kerogen remains undetermined – a focus of this study – and while this geochemical relationship has been more thoroughly documented for relatively young (Phanerozoic) deposits, there exist several limitations in applying those findings to Precambrian units. Most notably, the biological cycling of carbon isotopes on the Precambrian Earth was dominated by microbial communities in the absence of fungi, higher plants and macroscopic animals (Des Marais, 2001; Schidlowski, 2001), and the far more ancient rocks have typically been exposed to deeper burial and/or higher temperatures over much longer periods of time.

For Phanerozoic sedimentary rocks, vitrinite reflectance is a method often used to assess thermal maturity and peak metamorphic temperatures of preserved organic matter (e.g., Simoneit et al., 1981). This technique, however, is not directly applicable to Precambrian samples, as the land plants from which vitrinite macerals are derived had not yet evolved. Thus, other methods for determining the thermal alteration of ancient sedimentary rocks have been utilized. Raman spectroscopy has become a well-established tool for 2-D and 3-D geochemical mapping, and for investigating the thermal alteration of ancient kerogen and graphite (e.g., Beyssac et al., 2002; Allwood et al., 2006b; Kouketsu et al., 2014; Henry et al., 2019), including that of Precambrian carbonaceous microfossils preserved at a micrometer scale (e.g., Kudryavtsev et al., 2001; Schopf et al. 2005; Foucher et al., 2015).

Kerogen is primarily composed of large, interlinking polycyclic aromatic hydrocarbons (PAHs), which becomes increasingly ordered and carbon-rich as its other elemental constituents are increasingly lost during its graphitization with increasing temperature. Given that organic

hydrogen is more labile than carbon, the thermal maturity of fossilized organic matter may also be classified according to the elemental H/C ratio, wherein H/C values typically decrease (as $\delta^{13}C_{org}$ values increase) in more thermally altered kerogen (Hayes et al., 1983). However, measurements of elemental H/C ratios are normally limited to bulk (whole-rock) elemental analyses (e.g., Strauss et al., 1992a) and thus cannot be used directly to account for thermal alteration of kerogen at higher spatial resolution – for example, of individual microfossils or microscopic pieces of organic detritus.

In contrast, Raman spectroscopy is a non-destructive analytical technique that can be combined with optical microscopy to enable micrometer-scale in situ investigations of kerogenous microfossils and organic matter in petrographic thin sections (e.g., Schopf et al., 2005; Schopf and Kudryavtsev, 2009). As is here illustrated, this combination of geochemical techniques has allowed for more detailed comparisons of thermal maturity for organic carbon in the Precambrian rock record. Although the point at which the peak metamorphic temperature affects the carbon isotopic composition of microfossils and associated kerogen has yet to be determined, this study addresses these challenges by firmly establishing a comparison of Raman spectra and SIMS-derived $\delta^{13}C_{org}$ values from eight geologic units and their organic-walled microfossils (and detrital kerogen), all permineralized within sedimentary cherts affected by natural thermal alteration.

2. MATERIALS AND METHODS

2.1. Geologic units

Samples used in this study come from polished thin sections of organic-rich chert from eight separate geologic units, including seven Proterozoic deposits and one unit of Phanerozoic

age (ordered in Table 3-1 by increasing thermal maturity): the Kalkberg Limestone (~418 Ma), the Bungle Bungle Dolomite (~1,364 Ma), the Wumishan Formation (~1,500 Ma), the McLeary Formation (~2,100 Ma), the Vempalle Formation (1,700 Ma), the Beck Spring Dolomite (~850 Ma), the Auburn Dolomite (~740 Ma), and the River Wakefield Formation (~775 Ma). Thin sections of these eight fossiliferous cherts were acquired from the original collection of samples studied by Schopf et al. (2005), which analyzed Raman spectra from 22 geologic units and established the Raman Index of Preservation (RIP) for characterizing the relative geochemical alteration of variably altered carbonaceous microfossils. This index, the RIP, represents a Raman-based numerical metric for estimating the geothermal maturity of sedimentary kerogen based on changes in the broad "disordered" D-band (~1100–1500 cm^{-1}), and ranges linearly from least geochemically altered (a value of 9.0) to most altered (1.0).

The samples studied here are mostly stromatolitic and are all of the same lithology (chert), containing organic-walled fossil microorganisms and associated detrital kerogen permineralized in their siliceous host-rock matrix (viz., microcrystalline quartz). Importantly for the purposes of this study, this assemblage of samples includes organic constituents of varying thermal maturities, from unmetamorphosed to lower or mid-greenschist facies. Below and in Table 3-1 the eight geologic units studied here are listed in the descending order of their RIP values – not their geologic ages – as measured by Schopf et al. (2005), and the bulk geochemical data obtained from previous studies are briefly summarized.

Kalkberg Limestone (RIP = 8.5)

The Lower Devonian ~395 ± 5 Ma Kalkberg Formation, part of the Helderberg Group of central New York state, U.S.A., represents a shallow-marine offshore shelf environment with

preserved silicified limestones that contain permineralized organic-walled acritarchs exhibiting complex surface ornamentation, including such spiny acanthomorphs as *Multiplicisphaeridium* and *Micrhystridium,* representing extinct phytoplankton (Loeblich, 1970; Wicander and Schopf, 1974). The Kalkberg Formation limestones are of low metamorphic grade and record a decreasing carbon isotope trend following a positive isotopic excursion ($\delta^{13}C_{carb} \approx +5‰$) near the underlying Silurian–Devonian boundary, the overall $\delta^{13}C_{carb}$ values reported for the Kalkberg ranging from ~0‰ to +3.5‰ measured across several stratigraphic sections, with most values clustered around +1–2‰ and decreasing closer to 0‰ upsection (Husson et al., 2016; Hess and Trop, 2019).

Bungle Bungle Dolomite (RIP = 7.5)

Silicified stromatolitic carbonates of the ~1,364 Ma Bungle Bungle Dolomite occur in the Osmond Range of northeastern Western Australia and contain preserved microfossils such as the tubular sheaths of oscillatoriacean cyanobacteria (e.g., *Eomycetopsis*; Diver, 1974; Hofmann and Schopf, 1983). The depositional environment of the Bungle Bungle Dolomite has been interpreted as a restricted shallow-marine setting, the fossiliferous chert being of early diagenetic origin following the replacement of primary unmetamorphosed or subgreenschist facies carbonate sediments. Carbonate carbon isotope data for the Bungle Bungle Dolomite have average $\delta^{13}C_{carb}$ values of –0.7‰ (Schidlowski et al., 1983) and –0.3‰ for carbonate within a sample of chert (Strauss and Moore, 1992). Organic carbon isotope data for the unit have reported average $\delta^{13}C_{org}$ values of –23.1‰ (Schidlowski et al., 1983) and –28.1‰ (Hayes et al., 1983) for "whole-rock" total organic carbon (TOC). Strauss et al., 1992b further reported $\delta^{13}C_{org}$ analyses for two Bungle Bungle Dolomite samples, of TOC from carbonate (–24.6‰) and chert (–21.6‰).

Wumishan Formation (RIP = 7.4)

The ~1550–1450 Ma Wumishan Formation is part of the Early Mesoproterozoic Jixian Group exposed in North China, which on the bases of the lithologies and widespread unmetamorphosed stromatolitic deposits observed in several stratigraphic sections is thought to represent a peritidal, epicontinental environment (e.g., Kuang et al., 2012; Guo et al., 2013). Cherts of the Wumishan Formation stromatolites contain a diverse assemblage of microfossils, including filaments, spheroids, and other morphologies representing a variety of taxa (Zhang, 1985). Unmetamorphosed limestones and dolostones from the Wumishan Formation have yielded $\delta^{13}C_{carb}$ values that are mostly clustered around 0‰, and range from about –2‰ to +2‰ (Kuang et al., 2011; Guo et al., 2013). Strauss and Moore (1992) and Strauss et al. (1992b) report an average $\delta^{13}C_{org}$ value of –28.4‰ (the values ranging from –30.4‰ to –26.3‰) for "whole-rock" total organic carbon, and a value of –30.1‰ for kerogen extracted from a sample of chert (Strauss and Moore, 1992; Strauss et al., 1992a). Guo et al. (2013) reported a wider range of bulk organic carbon isotope values for the Wumishan Formation, ranging from approximately –31‰ to –23‰ and interpreted to reflect the presence of an autotrophic microbial community inhabiting a well-oxygenated and stratified peritidal marine environment.

McLeary Formation (RIP = 5.8)

The ~2,100 Ma McLeary Formation, located on the Belcher Islands in Hudson Bay, eastern Canada, contains Paleoproterozoic cyanobacterial microfossils (e.g., the entophysalidacean *Eosynechococcus* and the chroococcacean *Palaeoanacystis*) preserved in shallow marine stromatolitic cherts (Hofmann, 1976; Demoulin et al., 2019) and reaching a metamorphic grade of subgreenschist (Hayes et al., 1983). Bulk carbon isotope measurements yielded $\delta^{13}C_{carb}$ values of

–0.4‰ (Schidlowski et al., 1983; Strauss and Moore, 1992), along with $\delta^{13}C_{org}$ values of –24.9‰ for total organic carbon and –28.4‰ for extracted kerogen (Hayes et al., 1983; Strauss and Moore, 1992).

Vempalle Formation (RIP = 5.7)

The late Paleoproterozoic ~2,000–1,900 Ma Vempalle Formation of the Lower Cuddapah Supergroup occurs in the Cuddapah Basin of Andhra Pradesh, India. Shallow-marine cherts of this unit, reaching subgreenschist facies, preserve a diverse microbiota within *Collenia*-like stromatolites, including kerogenous, unnamed spheroidal unicells, preserved along with cellular, trichome-like filaments and broad tubular sheaths of oscillatoriacean cyanobacteria (Schopf and Prasad, 1978). Strauss and Moore (1992) documented an average $\delta^{13}C_{org}$ value of –28.0‰ for total organic carbon from two samples of the Vempalle chert. More recent carbonate carbon isotope analyses of stromatolitic dolomites of the Formation have recorded $\delta^{13}C_{carb}$ values ranging from –0.03 to –5.74‰, having an average value of –2.3‰ (Chakrabarti et al., 2011); other workers have reported $\delta^{13}C_{carb}$ values up to +2.0‰ with an average of +0.76‰ (Khelen et al., 2017).

Beck Spring Dolomite (RIP = 4.4)

The Beck Spring Dolomite (~780–730 Ma) is part of the "slightly metamorphosed" Neoproterozoic Pahrump Group cropping-out in southeastern California, U.S.A., samples of shallow-marine stromatolitic chert preserving such kerogenous cyanobacterial microfossils as the filamentous oscillatoriacean *Beckspringia communis* and the unicellular chroococcacean *Maculosphaera* (Licari et al., 1969; Licari, 1978; Schopf et al., 2005). Reported $\delta^{13}C_{org}$ values range from –25.7‰ for the kerogen of Beck Spring chert-carbonate to –15.2‰ for that in dolomite,

yielding an average of –22.0‰, not including a lower value of –26.5‰ for acid-extracted kerogen from such carbonate (Strauss and Moore, 1992). $\delta^{13}C_{carb}$ values for carbonates from the Beck Spring Dolomite average +4.2‰ and range from +3.8 to +4.8‰ (Strauss and Moore, 1992).

Auburn Dolomite (RIP = 1.5)

The late Neoproterozoic (~740 Ma) Auburn Dolomite Member of the Burra Group Saddleworth Formation, crops out near Leasingham in South Australia within the Adelaide Geosyncline, reaching lower greenschist facies (Preiss, 2000; Schopf et al., 2005). Samples of silicified clasts within bedded cherts preserve kerogenous microstructures including unnamed ellipsoidal unicells and "sheath-like filaments" (Schopf, 1975, 1992). Strauss and Moore (1992) and Strauss et al. (1992b) report a $\delta^{13}C_{org}$ value of –19.3‰ for one sample of chert-carbonate.

River Wakefield Formation (RIP = 1.0)

The River Wakefield Formation (~775 Ma), formerly the River Wakefield Subgroup (Preiss and Cowley, 1999), is part of the Burra Group Emeroo Subgroup of South Australia. Positioned stratigraphically below the Auburn Dolomite Member discussed above and similarly reaching lower greenschist facies (Preiss, 2000) – both situated in the Peake and Denison Ranges of northern South Australia and the two most geochemically altered of the eight units here investigated – the River Wakefield includes shallow-marine bedded cherts that contain morphologically diverse microfossils including colonial spheroids and asymmetrical laminated stalks of the *Solentia*-like pleurocapsacean cyanobacterium *Polybessurus* (Schopf, 1975, 1992). Strauss and Moore (1992) and Strauss et al. (1992b) reported average $\delta^{13}C_{org}$ values of –14.3‰, –19.1‰, and –18.1‰ for total organic carbon from samples of chert, shale, and carbonate,

respectively. Additionally, two $\delta^{13}C_{org}$ measurements of kerogen extracted from cherts yielded values of –31.7‰ and –16.4‰ (average = –24.1‰). Inorganic carbon isotope analyses of dolomite samples provided an average $\delta^{13}C_{carb}$ value of +2.7‰ within a range extending from +0.9 to +3.7‰.

2.2. Sample preparation and microscopy

Polished ~50–150 μm-thick petrographic thin sections of cherts from each of the eight geologic units were surveyed using transmitted light optical microscopy to locate surface-exposed microfossils and associated detrital kerogen appropriate for SIMS analysis. Use of microscopy immersion oil, typically applied to thin sections to improve the quality of high magnification (100X) optical microscopy, was avoided here in order to minimize potential surface organic contamination and better visualize surface defects (e.g., pits) on the thin sections – which happen to serve as useful navigational "landmarks" under the SIMS microscope. The samples previously investigated by Schopf et al. (2005) included many microfossils situated relatively deep (>5 μm) below the surface of the thin section that were not suitable for SIMS analysis, which measures carbon only from the specimens exposed at the surface of a thin section. This study thus required identification of microfossils near the thin section surface which are free from detrital kerogen that might interfere with their stable carbon isotope analysis. The carbon isotopic compositions of the background material were characterized by analyzing the detrital kerogen – identified here as diffuse, particulate kerogen distributed throughout the surface of the thin sections – away from the analyzed fossils.

Fossiliferous areas of thin sections containing surface-exposed kerogen were cut or mounted in epoxy on ~1" round mounts suitable for the SIMS sample holder, the fossils being

positioned as close to the center of the mount as possible in order to avoid adverse effects from measurements near the sample edge. The thin sections and epoxy-mounted standards were cleaned and sonicated multiple times in deionized (DI) water and ethanol for up to 1 min., then rinsed in DI water after each treatment and dried overnight in a vacuum oven at 50 °C. After cleaning, the target microfossils and associated background kerogen were photographed with transmitted and reflected light at multiple magnifications using a Leica DM6000 microscope housed at the NASA Jet Propulsion Laboratory (JPL) Astrobiogeochemistry Laboratory (abcLab), and their stage coordinates were documented relative to fiducial marks inserted at the edge of each thin section.

Scanning electron microscopy (SEM) of the analyzed samples was performed at the JPL abcLab using a Hitachi SU-3500 SEM to acquire images in secondary and backscattered electron modes. Prior to SIMS analyses, a 3-nm-thick platinum (Pt) veneer was applied to the sample surface and SEM images were acquired under high vacuum using an accelerating voltage of 15 keV at a working distance of ~7 mm. The mounts were then covered with a thicker (~30 nm) gold coat required for conductivity during SIMS analysis, and were degassed overnight in the SIMS sample storage chamber. Following each SIMS session, the gold coat was carefully removed with a 0.1-µm aluminum oxide polishing solution, and each specimen was re-imaged with variable-pressure SEM (backscattered electron) mode to confirm the accuracy of the positioning of analytical SIMS pits.

2.3. Raman spectroscopy

For all of the specimens investigated – each analyzed microfossil as well as background particulate detrital kerogen – Raman spectroscopy was used to document its kerogenous composition and geochemical, RIP-determined, maturity (Fig. 3-1). These Raman data were

acquired at the Raman Laboratory of the UCLA Center for the Study of Evolution and the Origin of Life using a T64000 triple-stage confocal laser-Raman system equipped with an argon ion laser having an excitation wavelength of 457.9 nm, a spectral window centered at ~1700 cm^{-1} and a ~1 μm spot size, comparable to this lab's many previous studies of Precambrian microfossils. Raman spectra collected here were calibrated using a silicon (Si) wafer standard with an established Raman shift of 520.2 cm^{-1}, a system that results in acquisition of both individual point spectra as well as two-dimensional Raman images that can be used to characterize the spatial distribution of geochemical components. Raman point spectra and 2-D geochemical maps were acquired and used to characterize the spatial relationships between each fossil and its associated kerogenous detritus and also of the host matrix consisting of microcrystalline chert (Figs. 3-1 and 3-2). Two-dimensional Raman geochemical maps were acquired across a ~20×20-μm area at ~0.5–2.0 μm depths, and Raman point spectra were occasionally collected from slightly deeper (up to ~10 μm) to obtain improved spectra used for deconvolution and calculating its geothermometry. Background noise for each spectrum was subtracted using a linear baseline between 950 and 1800 cm^{-1}, and spectra shown here (Fig. 3-1) are normalized to the intensity of the kerogen G-band (~1600 cm^{-1}).

Carbonaceous materials preserved in ancient sedimentary rocks exhibit two main Raman bands in the first-order region (~1000–1800 cm^{-1}) of the spectrum: the "disordered" D-band at ~1350 cm^{-1}, and the "graphitic" G-band at ~1600 cm^{-1}. The second-order region (~2400–3500 cm^{-1}) contains several less prominent bands (e.g., the S2-band at ~2900 cm^{-1}) that become more evident with increasing thermal maturity and are largely absent from spectra of unmetamorphosed organic matter (Pasteris & Wopenka, 1991; Beyssac et al., 2002; Schopf et al., 2005; Henry et al., 2019). The first-order bands can be deconvoluted to include additional subsidiary bands. Those

included here follow the deconvolution method applied by Kouketsu et al. (2014): the D1-band (~1350 cm^{-1}), D2-band (~1620 cm^{-1}), D3-band (~1510 cm^{-1}), and D4-band (~1245 cm^{-1}), in addition to an individual G-band at ~1580 cm^{-1} (Kouketsu et al., 2014). The main "graphitic" G-band located within the first-order region at ~1600 cm^{-1} combines both the D2-band and the individual G-band, resulting in a peak center position situated between the two bands. With increasing thermal maturity (i.e., graphitization), the first-order region of the Raman spectrum becomes dominated by a single G-band peak at 1583 cm^{-1} representing crystalline graphite, as is the case for the highly-oriented pyrolytic graphite (HOPG) standard also included here (Fig. 3-1). In addition to analyzing kerogen, Raman spectroscopy is also capable of determining the composition of minerals within the host rock matrix. For example, quartz (465 cm^{-1}) and carbonate minerals (ca. 1100 cm^{-1}) are frequently associated with permineralized carbonaceous microfossils, a result of early diagenetic silicification occurring within originally calcareous stromatolitic deposits.

Raman point spectra obtained for all microfossils and background kerogen were assessed and characterized quantitatively according to their Raman Index of Preservation (RIP) value. Schopf et al. (2005) defined the RIP value as the ratio of these two variables (α/γ) normalized to a set of thermally altered microfossils having RIP values ranging from 9 (least altered) to 1 (most altered), generated by the following equation:

(1) $$RIP = \frac{\alpha}{\gamma} \times \frac{8}{1.0082} - 0.005356.$$

in which α and γ represent the integrated area under the spectral curve between 1100 and 1300 cm^{-1} and 1300 and 1370 cm^{-1}, respectively.

Other methods of characterizing the geochemical maturity of kerogen using Raman spectroscopy include Raman geothermometry calculations for high-grade (e.g., Beyssac et al.,

2002; Aoya et al., 2010) and low-grade (e.g., Kouketsu et al., 2014) metasedimentary rocks. These Raman geothermometers are used to reconstruct peak metamorphic temperatures experienced by carbonaceous materials in sedimentary rocks and have been directly compared with other metrics used for determining temperatures in younger rocks, such as vitrinite reflectance and metamorphic mineral compositions.

Raman geothermometry calculations in this study were performed following the method described by Kouketsu et al. (2014), and processed Raman spectra of kerogen were deconvoluted using the software package PeakFit (v.4.12; SeaSolve Software Inc., Massachusetts, U.S.A.). Based on the recorded Raman spectrum, the proper peak fitting was selected. This study used the G, F, E, and D fittings for Raman geothermometry calculations (Table 3-3), as appropriate, to estimate peak metamorphic temperatures using Equation 2:

(2) $$T\ (°C) = -2.15(\text{FWHM-D1}) + 478$$

where FWHM-D1 (cm^{-1}) represents the full width at half maximum for the D1 Raman band of carbonaceous matter (i.e., kerogen) centered at 1350 cm^{-1}. This calculation is reliable for temperature measurements in the range of 150–400 °C with an error of ±30 °C (Kouketsu et al., 2014). These geothermometry values were used to provide estimates of peak metamorphic temperatures and to compare these results with the relative level of thermal maturity indicated by the RIP values obtained.

2.4. SIMS carbon isotope measurements

Standards

This study used a combination of two chert-kerogen standards developed from previous SIMS studies of Precambrian microfossils (e.g., House et al., 2000, 2013; Williford et al., 2013;

Schopf et al., 2018). The standards each contain four rock chips of carbonaceous chert centered within a ~1" round epoxy mount and polished to a <1-μm finish. Both standards come from the ~3,350 Ma Fig Tree Group of South Africa: standard specimen PPRG-215-1/2 contains thermally mature kerogen and comes from the PPRG-215 sample housed in the Precambrian Paleobiology Research Group (PPRG) collections at UCLA (Walter et al., 1983); the other standard specimen, the more thermally altered FTS-1 mount was acquired from the Fig Tree chert on the southeastern side of the Barberton Greenstone Belt within the Kaapvaal Craton. The two standards are thermally and isotopically distinct, differing both in their Raman spectra (Fig. 3-1) and their bulk carbon isotope compositions that are offset by ~18‰ (PPRG-215-1/2 = –31.5‰; FTS-1 = –13.5‰). This isotopic difference between the two standards allows for 2-point isotope calibration (Jardine and Cunjak, 2005), and for detailed comparison with SIMS-acquired fossil $\delta^{13}C_{org}$ values as calculated by use of Equation 4, discussed below.

Microfossil samples

SIMS carbon isotope measurements were performed during two analytical sessions (6/10–6/12/2019 and 10/29–10/31/2019) on the CAMECA IMS-1290 at the UCLA W.M. Keck Foundation Center for Isotope Geochemistry. Negative carbon secondary ions were collected simultaneously with an off-axis Faraday cup for $^{12}C_2^-$ and the axial electron multiplier for $^{12}C^{13}C^-$ under mass resolution (M/ΔM) of 6,000, which was sufficient to separate interferences from the peaks of interest. A 20 keV, ~0.04–1.4 nA $^{133}Cs^+$ primary ion beam was focused to a 10 μm spot size, and a 5×5 μm raster in combination with 100% dynamic transfer was used during the measurements, reducing the down-pit isotope fractionation. Each analysis consisted of 45 s of presputtering followed by 20 measurement cycles over a total counting time of 240 seconds.

Counts determined with the electron multiplier were corrected for the deadtime (47 ns) and Faraday cup signals were corrected for the background determined for each analysis by deflecting the secondary ion beam out of the detector during presputtering.

For each group of ~5–20 analyzed specimens, eight measurements were made of the chert-kerogen standard for bracketing the sample analyses (Tables 3-4 and 3-5). The small size of some analyzed microfossils (<5 μm in diameter), or otherwise low carbon content within the ~10 μm diameter of the analytical spot, occasionally yielded low secondary ion count rates, and thus lower precision compared to larger and better exposed fossils and carbon-rich areas of detrital kerogen at the thin section surface. However, analytical spots containing an overabundance of carbon are subject to relatively high count rates that can saturate the SIMS detector, a complication that requires careful consideration of the quantity and distribution of surface-exposed kerogen for each SIMS measurement.

Instrumental bias (α_{SIMS}) was determined by calculating the average "raw" value ($\delta^{13}C_{raw} = [(^{12}C^{13}C/^{12}C^{12}C)_{measured}/(0.01118 \times 2) - 1] \times 1000$) of eight bracketing analyses for the working standard (PPRG-215-1/2 or FTS-1) compared to its average "whole-rock" carbon isotopic ($\delta^{13}C_{bulk}$) value (PPRG-215-1/2 = –31.5‰, Hayes et al., 1983; FTS-1 = –13.5‰), using the method of Kita et al. (2009) and Williford et al. (2013) and calculated using Equation 3:

(3) $$\alpha_{SIMS} = (\delta^{13}C_{raw} + 1000)/(\delta^{13}C_{bulk} + 1000).$$

The α_{SIMS} value obtained permits the correction of raw $\delta^{13}C$ values for unknown sample analyses by use of the following equation (Williford et al., 2013):

(4) $$\delta^{13}C_{VPDB}(sample) = [(1 + \delta^{13}C_{raw}(sample)/1000/\alpha_{SIMS} - 1] \times 1000.$$

External precision was calculated as two standard deviations (±2SD) of the $\delta^{13}C_{raw}$ values obtained for eight bracketing measurements of the standard. Internal precision was calculated as

two standard errors (±2SE) of $\delta^{13}C_{raw}$ values measured over 20 individual cycles for each SIMS analysis, results largely influenced by heterogeneity in the amount of organic carbon at depth within the target area and its effect on counting statistics. Unstable or fluctuating (increasing and/or decreasing) count rates during SIMS analysis are attributed here to the heterogeneity of carbon within the analytical pit area as the primary ion beam penetrated the chert-kerogen matrix. For cases in which $^{12}C_2^-$ count rates either rapidly decreased, increased (i.e., flooding the detector), or considerably fluctuated, the measurement was aborted during analysis or removed from the dataset.

In order to avoid overestimation of errors and more accurately reflect variations in isotopic compositions and $^{12}C_2^-$ count rates within a single analytical spot, total uncertainty is expressed here as the square root of the sum of the squares for the standard error of the bracketing mean and the internal precision of each sample analysis (Tables 3-4 and 3-5) (Peng et al., 2016). The ratio of $^{12}C_2^-$ counts for individual microfossils (and background kerogen) to the average $^{12}C_2^-$ count rate for bracketing standards is referred to as $^{12}C_2^-{}_{rel}$ and shown as a percentage (%) (Tables 3-4 and 3-5). Although SIMS measurements of microfossils having low relative count rates ($^{12}C_2^-{}_{rel}$ below ~10%) were discarded from the dataset, it should be noted here that there was no observed correlation between $\delta^{13}C_{raw}$ and $^{12}C_2^-{}_{rel}$ values, or between $\delta^{13}C_{raw}$ and "yield" (1Mcps/nA) (see Schopf et al., 2018) for accepted standard and sample analyses, despite having a lower internal precision (cf. Peng et al., 2016). Some kerogen-poor background measurements are here included for comparison with the remainder of the dataset (Tables 3-4 and 3-5). Analyses of associated detrital kerogen often produced low $^{12}C_2^-$ count rates (range = 2.1×10^5 to 4.3×10^6 cps) due to the sparse distribution of particulate organic matter in the analyzed cherts, but are useful for evaluation in comparison with values obtained from analyzed microfossils; thus, the $\delta^{13}C_{org}$ values for

background kerogen are here included in the data presented, but not incorporated into the paleobiological interpretations of this study.

3. RESULTS

3.1. Raman spectra of kerogen

Raman spectra of kerogen from the microfossils and particulate background detritus in the eight geologic units studied here – listed above and ordered in Tables 3-1 and 3-2 by their RIP values – show the same trend of increasing thermal maturity from relatively unmetamorphosed units to lower greenschist facies as those initially reported by Schopf et al. (2005). The RIP values newly determined in this study, like those in the earlier work, were calculated from fossil kerogen spectra that thus show notable differences in the degree of geochemical maturity, and were found to range from ~8.7 (least altered) to ~2.0 (most altered), which corresponds to Raman geothermometry estimates ranging from ~209 °C to ~390 °C based on a total of 63 well-calibrated point spectrum measurements (Fig. 3-3). The variation among RIP values for a given geologic unit is low, the standard deviation values (1SD) for RIP reaching no greater than ~0.30 (Table 3-3). These data are further summarized in Table 3-2.

For the Kalkberg Limestone, RIP values average 8.2 ± 0.3 (1SD) and range from 7.9 to 8.7 (n = 5). Raman geothermometry measurements determined using these spectra show an average estimated temperature of 228 ± 5 °C (1SD), with a range of values from 219° to 233 °C (±30 °C; Kouketsu et al., 2014). RIP values for the Bungle Bungle Dolomite average 7.4 ± 0.1 and range from 7.2–7.6 (n = 14). For this unit, Raman geothermometry measurements give an average estimated temperature of 263 ± 7 °C, with a range from 248–274 °C. Raman spectra of kerogen

within the Wumishan Formation produced RIP values averaging 7.5 ± 0.2 and ranging from 7.4 to 7.9 (n = 8), with an average estimated temperature of 213 ± 5 °C and a range of 210–223 °C. The McLeary Formation yielded RIP values averaging 5.6 ± 0.2 and ranging from 5.3 to 5.9 (n = 8) yielding an average estimated temperature of 276 ± 5 °C, with a range from 270–284 °C. For the Vempalle Formation, RIP values for fossil kerogen average 5.3 ± 0.3 and range from 4.9–5.6 (n = 8). For this unit. Raman geothermometry values determined using these spectra show an average temperature of 286 ± 9 °C, with a range of 272–298 °C. The Raman spectra of kerogen within the Beck Spring Dolomite produced RIP values averaging 4.5 ± 0.2 and ranging from 4.3–4.6 (n = 6), with an average estimated temperature of 328 ± 10 °C and a range of 320–350 °C. RIP values for the Auburn Dolomite average 2.2 ± 0.1 and range from 2.1–2.4 (n = 7) yielding an average estimated temperature of 378 ± 2 °C, with a range from 376–380 °C. Raman spectra of kerogen within the River Wakefield Formation produced RIP values averaging 2.4 ± 0.3 and ranging from 2.0–2.7 (n = 7), with an average estimated temperature of 378 ± 8 °C and a range of 370–390 °C.

3.2. SIMS carbon isotopes

Over the course of the two SIMS analytical sessions, a total of 151 analyses were made for targeted sample microfossils and associated particulate kerogen. In total, 19 measurements were discarded due to excessively low or high (or fluctuating) $^{12}C_2^-$ count rates, providing 132 accepted SIMS sample measurements. For the chert-kerogen standards, 144 measurements were made in total, including the bracketing analyses of standards between the samples, and 18 were discarded due to variable count rates. Average $\delta^{13}C_{org}$ values determined for microfossils and background kerogen in each of the geologic units studied are listed in Table 3-2.

In the first SIMS session (6/10–6/12/2019), since the focus was the least geothermally altered units of the suite of samples analyzed, the PPRG-215-1/2 standard was used as the working standard. In the second SIMS session (10/29–10/31/2019) the FTS-1 standard was used, due to the higher geochemical maturity of the kerogenous microfossils (and detritus) of most samples analyzed. The PPRG-215-1/2 mount used as the first working standard yielded an average of ~1.0×10^6 $^{12}C_2^-$ counts per second (cps) with a range of ~2.3×10^5 to ~5.1×10^6 cps for accepted analyses (n = 44), whereas the FTS-1 mount averaged ~2.6×10^6 cps, ranging from ~8.8×10^5 to ~5.9×10^6 cps (n = 16). In the second SIMS session, this FTS-1 mount was used as the working standard with a similar average $^{12}C_2^-$ count rate of ~2.6×10^6 cps and a range of ~8.1×10^5 to ~7.8×10^6 cps (n = 64), and analyses of the PPRG-215-1/2 mount from this session yielded an average of 1.8×10^6 cps with a range from ~8.1×10^5 to ~3.4×10^6 cps (n = 8). These count rates give a comparison of the relative concentrations of organic carbon for each of the standards, and ultimately relate to the determination of $^{12}C_{2\,rel}^-$ values calculated for the sample analyses (Tables 3-4 and 3-5).

During the first SIMS session, the working standard, PPRG-215-1/2, yielded considerably lower count rates than the FTS-1 standard, likely due to the nature of the distribution and concentration of kerogen exposed at the surface of the epoxy-mounted rock chip. However, considering that the PPRG-215-1/2 standard had overall lower count rates (1.0×10^6 cps compared to 2.6×10^6 cps for FTS-1), it also yielded higher $^{12}C_{2\,rel}^-$ values (~109%) on average during Session 1 with average count rates of 9.1×10^5 cps for analyzed sample specimens, compared to that of the FTS-1 standard during Session 2 which had higher $^{12}C_2^-$ count rates on average (2.6×10^6 cps) but yielded lower $^{12}C_{2\,rel}^-$ values (~51%) on average (despite having slightly higher $^{12}C_2^-$ count rates of ~1.2×10^6 cps for the analyzed samples).

The SIMS $\delta^{13}C_{org}$ values determined for target microfossils and associated background kerogen are summarized in Tables 3-4 and 3-5. $\delta^{13}C_{org}$ values of microfossils from the Kalkberg Limestone range from –29.0 to –20.8‰ and average –24.0‰ (n = 8), with an average $^{12}C_2^-$ count rate of 2.5×10^6 cps. The $\delta^{13}C_{org}$ values of fossils and associated background kerogen from the Bungle Bungle Dolomite range from –31.1‰ to –23.4‰ (n = 27), with its microfossils yielding an average of –26.0‰ and background kerogen analyses averaging –26.2‰, with an overall average count rate of 7.8×10^5 cps. For the Wumishan Formation, the $\delta^{13}C_{org}$ values of fossils and background kerogen range from –31.2‰ to –25.4‰ (n = 12), with the analyzed microfossils averaging –29.0‰ and background kerogen yielding an average of –26.4‰, the average count rate for these analyses being 4.3×10^5 cps. The $\delta^{13}C_{org}$ values of detrital kerogen from the McLeary Formation range from –29.6‰ to –20.2‰ and average –25.2‰ (n = 22), along with an average count rate of 9.8×10^5 cps. The target fossils and associated background kerogen from the Vempalle Formation yielded $\delta^{13}C_{org}$ values ranging from –32.4‰ to –22.9‰ (n = 25), with microfossils averaging –26.3‰ compared to –25.8‰ for background kerogen, and an overall average count rate of 1.2×10^6 cps. The $\delta^{13}C_{org}$ values of samples from the Beck Spring Dolomite range from –25.6‰ to –23.0‰ (n = 4), with an average of –25.2‰ for microfossils and –23.0‰ for associated background kerogen, and an overall average count rate of 7.9×10^5 cps. For the Auburn Dolomite, $\delta^{13}C_{org}$ values of the target microfossils averaged –21.0‰ and range from –26.2‰ to –17.0‰ (n = 16), along with one measurement of detrital background kerogen having a value of –19.7‰ and an average count rate of 1.2×10^6 cps for all analyses of this unit. SIMS measurements from the River Wakefield Formation had an average $\delta^{13}C_{org}$ value of –26.2‰ and range from –32.3‰ to –21.4‰ (n = 16), microfossil analyses yielding an average of –26.8‰ and background kerogen having an average value of –24.4‰, with an overall average count rate of 5.2×10^5 cps.

4. DISCUSSION

The scientific pursuit for evidence of early life on Earth is guided by the practice of seeking constraints for establishing the indigenousness, syngenicity, and biogenicity of putative biologic microstructures in ancient sedimentary rocks. These paleobiological studies involve a combination of morphological, geochemical, and/or isotopic data (e.g., Schopf et al., 2007; Oehler and Cady, 2014), the "gold-standard" for such studies dating from the seminal 1965 studies of thin section-embedded chert-permineralized microscopic fossils in the Precambrian rock record (Barghoorn and Tyler, 1965; Barghoorn and Schopf, 1965) followed later by the pioneering use of SIMS for analyzing the carbon isotopes of such microfossils (House et al., 2000) and in situ laser Raman spectroscopy of their kerogenous components (Kudryavtsev et al., 2001), thus forming the basis of the strategy followed here.

However, due to the activity of plate tectonics during the course of Earth's ~4.5 billion year history, virtually all of Earth's earliest rock record has eroded away, there being only ~5% of the remaining rock record dating from the Archean, the earliest pre-2.5 Ga history of the planet (Garrels and McKenzie, 1971). Moreover, the vast majority of the earliest rocks exposed and still available for study have been far too heated or metamorphically altered to preserve morphological remains of fossilized microorganisms, thus leaving geochemical and isotopic evidence as the primary source of data for interpretation. In such cases, the typically less altered Proterozoic (and Phanerozoic) rock record, containing indigenous, syngenetic, and demonstrably biogenic cellularly preserved microbes, serves as a valuable source of reference for evaluating potential microfossils and associated organic matter preserved in older Archean-age rocks.

While morphological "biosignatures" are often destroyed during geological processes of diagenesis, lithification, and/or metamorphism, geochemical signatures such as macromolecular carbonaceous matter and associated stable isotope compositions are relatively more resilient and may survive and preserve evidence of ancient biological activity. Various sedimentary rocks and minerals behave differently under increasing pressure and temperature during burial and metamorphism and, compared to many other geochemical components, macromolecular kerogen and stable carbon isotope compositions of organic matter preserved in chert are considered to be among the materials most resistant to degradation over billion year timescales (Oehler et al., 1972; Schidlowski, 2001; McCollom, 2011; Javaux, 2019).

The detection and characterization of carbonaceous matter (i.e., kerogen, graphite) in Precambrian sedimentary rocks are regularly achievable with Raman spectroscopy, and the Raman spectra of kerogenous microfossils preserved in relatively unmetamorphosed cherts represent primary evidence of biologically produced carbon in the rock record. Although several earlier studies have combined Raman spectroscopic analyses with ion microprobe carbon isotope measurements in order to correlate fossil kerogen and graphite with measured $\delta^{13}C_{org}$ values (e.g., McKeegan et al., 2007; Williford et al., 2013; Schopf et al., 2018), none has systematically investigated the relationship between Raman spectra and $\delta^{13}C_{org}$ values for carbonaceous microfossils of differing thermal maturity. This study is ostensibly the first to characterize the Raman-based geochemical and SIMS-measured isotopic compositions of individual kerogenous microfossils and associated organic detritus through a range of thermally altered Precambrian chert samples, an effort to better define the preservation of carbon isotopic evidence associated with early life on Earth.

Stable carbon isotope compositions of Precambrian kerogen are primarily controlled by the biosynthetic pathways involved during the initial formation of microbial biomass or their organic biomolecular components which undergo polymerization resulting in the production of thermally immature kerogen. Traditional studies of sedimentary organic matter have used bulk (i.e., 1 kg whole-rock) analyses of total organic carbon and extracted kerogen along with other metrics to assess the paleoecology of Precambrian ecosystems, showing that the isotopic offset of roughly –25‰ between organic (kerogen, TOC) and inorganic (carbonate) carbon extends throughout the Precambrian – at least to ~3.5 Ga – and is primarily attributable to autotrophic carbon fixation by various microorganisms (Hayes et al., 1983, 1993; Des Marais, 1997, 2001; Schidlowski, 2001). SIMS analyses of individual Precambrian microfossils were first introduced to such studies by House et al. (2000), and have involved studies of both prokaryotic and eukaryotic photoautotrophic organisms from the later Precambrian (e.g., House et al., 2000, 2013; Williford et al., 2013; Peng et al., 2016), thus permitting direct characterization of the carbon isotope composition of distinct morphotypes for fossil microorganisms. The present study further expands the known microfossil $\delta^{13}C_{org}$ record by including analyses of new fossil morphologies in addition to those from more thermally altered geologic units exposed to greenschist facies metamorphism.

As the search for evidence of life's earliest records continues to expand into older and more thermally altered rock units, it has become increasingly important for paleobiologists to accurately understand the processes that control the preservation of geochemical and isotopic signatures associated with fossilization (i.e., taphonomy) and the subsequent alteration of sedimentary organic matter originally produced by primitive microorganisms. The data reported here provide a detailed comparison of the relationship between early thermal alteration of the kerogenous components of sedimentary cherts and the preservation of carbon isotope signatures associated

with ancient life. Moreover, although increasing thermal maturation is known to affect the carbon isotopic composition of preserved kerogen, it has heretofore proven difficult to determine the temperature and metamorphic grade at which such geochemical changes are initiated.

Earlier studies including those of McKirdy and Hahn (1982), Hayes et al. (1983), Schidlowski (1987, 1988), Des Marais et al. (1992), and Des Marais (1997) used bulk analyses of total organic carbon and elemental H/C ratios to relate changes in Precambrian $\delta^{13}C_{org}$ values to the progression of thermal alteration. At the time of these studies, it was already well accepted that stable carbon isotope compositions of sedimentary organic matter could be affected by "shallow" geological burial (<1 km) at temperatures as low as 60 °C (McKirdy and Hahn, 1982), and that the organic matter of thermally altered units may not be a reliable source of isotopic data (Summons and Hayes, 1992). Thus, the effects on carbon isotopic compositions resulting from the thermal maturation of Precambrian kerogen have been the subject of ongoing studies, a gradual progression of geochemical changes for most sedimentary lithologies thought to begin at or below greenschist facies (e.g., Hayes et al., 1983; Kitchen and Valley, 1995; Watanabe et al., 1997; Schidlowski, 2001). Current temperature-pressure estimates for greenschist metamorphism, while dependent on several factors including initial rock compositions, typically range from "unmetamorphosed", "low grade", or subgreenschist (<250 °C) to lower greenschist (~250–350 °C, 2–8 kb), mid-greenschist (~300–450 °C, 2–10 kb), and upper greenschist (~400–500 °C, 4–9 kb) (c.f., Klein and Hurlbut, 1985; Bucher and Grapes, 2011). These temperature and pressure estimates provide means to evaluate the data reported here from several geologic units, determined by RIP measurements, which have experienced low- to mid-greenschist facies alteration.

4.1. Raman spectra and geothermometry of kerogen

There are many complementary approaches to using Raman spectroscopy to determine the geothermal maturity of ancient kerogen (for a recent review see Henry et al., 2019). For example, despite their use of differing parameters to determine geothermal maturity, the RIP metric of Schopf et al. (2005) and the Raman geothermometry calculations of Kouketsu et al. (2014) track in parallel when applied to the same Raman data (Fig. 3-3), yielding a regression analysis R^2 value of 0.916 for the numerous samples studied here (n = 63). Comparison of these same data yields a calculated standard error of the regression line of ~16.5 (1SE), corresponding to the ± 30 °C error reported for the method of Kouketsu et al. (2014), and defines a basic mathematical relationship between the derived data (equation 5, below) for estimating peak metamorphic temperatures (°C) from the RIP values alone, an estimate that could be further constrained by the inclusion of additional relevant data:

(5) $$T\ (°C) = -25.776\ (RIP) + 433.99.$$

The Raman spectra documented here closely match those reported initially by Schopf et al. (2005), including new fossils and associated kerogen studied from the same chert thin sections. Slight differences were observed in some calculated RIP values, most notably those of the two most thermally altered members of the analyzed suite, the Auburn Dolomite Member and River Wakefield Formation, which yielded slightly higher RIP values (and thus a lower thermal maturity) compared to those reported by Schopf et al. (2005), while still exhibiting the lowest RIP values of the geologic units studied. Of these, although the Auburn Dolomite yielded the lowest average RIP value (2.2 ± 0.1), the lowest overall value observed came from the River Wakefield Formation (RIP = 2.0), and both samples provided an average estimated temperature of ~378 °C.

The total range of all RIP values observed was 8.7–2.0, corresponding to a peak temperature range for the eight analyzed units of ~210–390 °C. Kouketsu et al. (2014) indicate that their method for estimation of metamorphic temperature is applicable for temperatures of ~150–400 °C with a 30 °C error. The Raman spectra collected here and the RIP values calculated from these spectra closely match such geothermometry estimates. Moreover, the data presented in the present study also correlate well with the range of metamorphic grades ascribed to the geologic units analyzed, ranging from "unmetamorphosed" to lower greenschist. However, peak metamorphic temperatures greater than ~350 °C are usually indicative of mid-greenschist facies, into which the Auburn Dolomite and River Wakefield samples may be classified based on the Raman data presented here.

This study also notes a marked shift in previous bulk $\delta^{13}C$ values between unmetamorphosed sedimentary rocks and those of greenschist facies (Figs. 3-4 and 3-5), which suggests that changes in stable carbon isotope values resulting from increasing thermal maturity may be initiated at relatively lower temperatures (ca. 200–300 °C). Kitchen and Valley (1995) compared calcite-graphite carbon isotope fractionations ($\Delta_{(cal\text{-}gr)}$, ‰) with the reported metamorphic facies of the samples analyzed and noted a correlative shift in the carbon isotopic composition of calcite (decreasing $\delta^{13}C$) and graphite (increasing $\delta^{13}C$) as thermal alteration of sedimentary rocks progressed into amphibolite or granulite metamorphic facies (T > 450 °C). This scenario is possible provided that two different carbon species (organic and inorganic) are present and available for carbon-exchange and substitution, such as occurs during the metamorphism of carbonate rocks containing appreciable amounts of organic carbon. Exchange of $^{13}C/^{12}C$ between organic (kerogen, graphite) and inorganic (carbonate) carbon at such high temperatures has been proposed to result from isotopic re-equilibration of "light" (^{13}C-depleted) kerogen (or graphite)

and "heavy" gaseous carbon dioxide (CO_2) produced during metamorphic decarbonation reactions, like those that occur during synthesis of tremolite from dolomite and quartz (Bottinga, 1969; Schidlowski, 2001). However, because such reactions are highly dependent on the starting conditions of the host rock and can be difficult to constrain, it is important to characterize changes in thermal maturity and carbon isotope compositions of carbonaceous microfossils within the same lithology to properly understand the processes affecting shifts in the $\delta^{13}C$ values of ancient kerogen. Use of the techniques illustrated here, on samples of Precambrian cherts, demonstrate new insights to this problem.

4.2. SIMS carbon isotope analyses

The SIMS data reported from this study add to the growing number of investigations into the carbon isotope composition of individual Precambrian microfossils. Whereas previous work has mostly concentrated on either well-preserved Proterozoic microfossils (House et al., 2000, 2011; Williford et al., 2013; Peng et al., 2016) or less well-preserved and more thermally altered Archean samples (Ueno et al., 2001, 2002; Lepot et al., 2013; Morag et al., 2016; Schopf et al., 2018), none have systematically investigated the relationship between the thermal maturation of microfossil kerogen as measured by Raman spectroscopy and $\delta^{13}C_{org}$ values determined for individual fossils using SIMS. Here, we compare SIMS $\delta^{13}C_{org}$ values recorded from eight different geologic units and their representative fossil taxa, as well as their thermal maturities, studies based on optical microscopy and corresponding Raman images and spectra of permineralized kerogenous microfossils and associated detrital kerogen.

All $\delta^{13}C_{org}$ values presented here are consistent with previously reported interpretations of the biogenicity and taxonomic affinities of the identified microfossils. Moreover, combined with

fossil morphologies and consonant with the established depositional environments of the units investigated, the range of SIMS $\delta^{13}C_{org}$ values recorded in this study are evidently attributable to prokaryotic (bacterial) and/or eukaryotic photoautotrophy, with little or no influence from microbial (archaeal) methanogenesis or methanotrophy (Hayes, 1994; Des Marais, 2001; Schidlowski, 2001). Overall, $\delta^{13}C_{org}$ values differ by up to ~11‰ among the eight geologic units studied, and while $\delta^{13}C_{org}$ values for individual microfossil taxa are typically clustered close together (i.e., within 1–3‰) some also vary by up to ~5‰, generally consistent with previous findings (e.g., House et al., 2000; Williford et al., 2013). Additionally, average $\delta^{13}C_{org}$ values measured for each of the SIMS samples closely align and overlap with averages from bulk carbon isotope analyses of its geologic unit (the single exception being the River Wakefield Formation, which yielded average $\delta^{13}C_{org}$ values ~12‰ lower than that obtained from bulk analyses). This difference in the measured $\delta^{13}C_{org}$ values for one of the two most thermally altered units of this study suggests that it is a result of the preservation of kerogenous materials within the enclosing chert matrix which has effectively shielded the organic carbon from the isotopic fractionation experienced by other carbon species within the host rock as a result of increased metamorphic temperatures. Similar phenomena have been observed in previous studies of metamorphic rocks, and the means by which chert (i.e., quartz) protects organic carbon in thermally altered rocks has been referred to as the "armoring effect" (Wada and Suzuki, 1983), though the exact chemical mechanism remains contentious and requires further investigation (Ueno et al., 2002; Papineau et al., 2011; Ohtomo et al., 2014; Tashiro et al., 2017; Osterhout et al., 2019).

In using $\delta^{13}C_{org}$ values to reconstruct the physiology (i.e., metabolism) of ancient microfossils, carbon isotope signatures of fossil kerogen are characterized in reference to the range of known $\delta^{13}C_{org}$ values of extant microbial morphological counterparts, compared with $\delta^{13}C_{carb}$

inferred to represent their inorganic carbon substrate as typically recorded in associated primary carbonates. Naturally, this is not always feasible in geologic settings or within individual thin sections, and chemostratigraphic data commonly provide the best source of abundant and reliable $\delta^{13}C_{carb}$ values. Despite these limitations, efforts are continually being made by paleobiologists to classify morphologically distinct Precambrian microfossils according to their assumed isotopic fractionation ($\varepsilon_p \approx \delta^{13}C_{carb} - \delta^{13}C_{org}$) based on average $\delta^{13}C_{carb}$ values of primary carbonates and SIMS-analyzed $\delta^{13}C_{org}$ values of carbonaceous microfossils (e.g., Williford et al., 2013; Peng et al., 2016). Carbon isotope fractionation values (ε_p) calculated for the fossils analyzed here, based on average $\delta^{13}C_{carb}$ values from previous literature, range from ~25‰ to ~29‰.

Interestingly, some of the samples analyzed yielded distinct $\delta^{13}C_{org}$ values for morphologically differing fossils preserved within the same thin section. For instance, in the Kalkberg Limestone a ~5‰ difference exists on average between *Multiplicisphaeridium* (–21.3 ± 0.7‰, 1SD; n = 3) and *Micrhystridium* (–26.3 ± 2.5‰; n = 3) specimens and, in the River Wakefield Formation, between *Polybessurus* (–28.3 ± 2.4‰; n = 9) and unnamed spheroidal unicell colonies (–23.4 ± 1.9‰; n = 4). The data here recorded are too few to make broad interpretations regarding such differences in carbon fixation processes between the various preserved taxa. Nevertheless, the Kalkberg findings may be applied conservatively to the morphological characteristics of the two taxa noted, namely that *Multiplicisphaeridium* exhibits a much larger cell diameter than *Micrhystridium*, such size differences being known to affect ε_p values as the amount of $CO_2(aq)$ that is incorporated into a cell is related to its surface-to-volume ratio which, in turn, correlates with the maximum growth rate of a given taxon (Popp et al., 1998). Thus, for unicells that have a lower surface-to-volume ratio, the fractionation (ε_p) values may potentially be lower. Other factors could also influence the final $\delta^{13}C_{org}$ composition of kerogenous

microfossils, including differences in the surface-to-volume ratio produced by the presence of spines in acanthomorph as compared to sphaeromorph acritarchs and the differing density of spines in various acanthomorph taxa (e.g., *Multiplicisphaeridium* vs. *Micrhystridium*) as well as differences in nutrient and light availability (Cassar et al., 2006). Finally, the amount of thermal alteration experienced by the host sedimentary rock must also be accounted for in order to properly interpret microbial metabolisms from the preserved $\delta^{13}C_{org}$ values of microfossil populations, a factor that can be effectively ruled out for the unmetamorphosed Kalkberg Formation and potentially for the more geothermally altered River Wakefield Formation, as described above.

Several reports have noted a growing need for the development of a widely available SIMS standard for analyses of the carbon isotopes of individual chert-permineralized Precambrian microfossils (House et al., 2000; Orphan and House, 2009; House, 2015). Such SIMS studies have typically used only one type of analytical standard, which contains only either amorphous kerogen (House et al., 2000, 2013; Lepot et al., 2013; Williford et al., 2013; Morag et al., 2016; Peng et al., 2016; Schopf et al., 2018) or crystalline graphite (Ueno et al., 2001; Wacey et al., 2011). To the best of our knowledge, the present study represents the first using standards of both types for SIMS carbon isotope analyses of microfossils. Standards were previously typically selected on the basis of their "isotopic fit" with the analyzed specimens but sometimes differing starkly from the analyzed material, and even yielding differing values from the same geologic unit (see Morag et al., 2016, p. 443).

In the present study, two epoxy-mounted standards were used, one containing better preserved (^{13}C-depleted) amorphous kerogen (PPRG-215) and the other more graphitized (and ^{13}C-enriched) carbon (FTS-1), both coming from sedimentary cherts of the same geologic unit. Use of this two-standard approach affords several advantages, most notably the direct comparison

of Raman spectra and RIP values of the standards with those of the targeted specimens. Moreover, the carbon isotope measurements of newly analyzed microfossils and associated kerogen can be evaluated relative to two differing natural standards and their distinct $\delta^{13}C_{org}$ values (as determined by conventional bulk "whole-rock" analyses). Thus, total uncertainty is primarily controlled by the isotopic heterogeneity of the two analytical standards, the two used here exhibiting different levels of $\delta^{13}C_{org}$ homogeneity and $^{12}C_2^-$ count rates, the PPRG-215-1/2 (kerogenous) standard generally yielding lower $\delta^{13}C_{org}$ values and lower $^{12}C_2^-$ count rates compared to those of the FTS-1 (graphitized) standard.

Thus, for each set of specimens (i.e., microfossils and background kerogen) here analyzed from the eight geologic units and evaluated in comparison with bracketing analyses of a particular carbonaceous chert standard, the $\delta^{13}C_{org}$ value of each analysis can be calculated based on the measured $^{12}C^{13}C/^{12}C^{12}C$ ratio and α_{SIMS} value as described in Equations 3 and 4 above, and also compared, using equations 6 and 7, with the two-point calibration equation derived from the accepted standard analyses for each analytical session:

(6) $$\delta^{13}C_{VPDB}(calibrated) = 0.9209 \times \delta^{13}C_{raw} + 7.5146$$ (Session 1)

(7) $$\delta^{13}C_{VPDB}(calibrated) = 0.8523 \times \delta^{13}C_{raw} + 14.796$$ (Session 2)

Values of an analyzed specimen that differ significantly from the observed range for the two standards (i.e., more than ~3.5‰; 2SE) should be examined and potentially excluded from the data based on the observed difference from other sample measurements compared to the standards measured during the same SIMS session.

4.3. Application to studies of early life on Earth

Precambrian sedimentary rocks can form through a variety of processes, the generation of units containing chert-permineralized microbial fossils typically resulting from the initial deposition of calcareous sediments in which the original carbonate has been replaced during early diagenesis by colloidal silica that, upon lithification, results in the fossils and associated organics being three-dimensionally embedded in microcrystalline quartz. Such silica-permineralization is particularly common in the Precambrian, a result of the supersaturation of silica in shallow marine environments prior to the evolution of siliceous organisms such as sponges, diatoms, and radiolarians that govern the current marine silica cycle (e.g., Maliva et al., 2005; Perry and Lefticariu, 2014).

As a result of this process, the formation and burial of microbial mat communities – in their lithified form known as stromatolites – and of both their cellular components and associated organic detritus permits their detailed geochemical analysis as presented here. Studies of modern microbial communities indicate that the components most resistant to degradation are cell walls and the extracellular polymeric substances (EPS) that surround individual cells, trichomes, colonies, and their multi-component aggregates (i.e., biofilms) (Bartley, 1996; Kremer et al., 2012; Manning-Berg et al., 2019). These biological materials remain in the host rock primarily as a complex mix of polysaccharides and other degradation products of biomolecules. Over geological time, and with increasing burial depths accompanied by rising temperatures and pressures, these distinctive biological materials are transformed into amorphous macromolecular kerogen (e.g., Kaźmierczak and Kremer, 2002; Lee et al., 2019).

Although the process of permineralization is responsible for the preservation of organic-walled microfossils, it frequently precludes meaningful direct measurement of the carbon isotopes

of co-existing primary carbonate minerals, as the carbonate minerals in stromatolitic cherts (e.g., calcite and dolomite rhombs, siderite crystals) may have a post-depositional origin (e.g., Buick, 1990; Petrash et al., 2016). Nevertheless, it is evident that bedded carbonates from the same geologic unit may preserve evidence of seawater chemistry including the temperature-dependent (–0.063‰/°C) $\delta^{13}C$ composition of CO_2(aq) in shallow photic-zone waters (Emrich et al., 1970; Freeman and Hayes, 1992; Hayes et al., 1999; Williford et al., 2013). And, of course, these challenges are even further complicated in the older and more geochemically altered rocks of the early Archean and Hadean, for which there are evidently very few primary unaltered carbonates present.

Available evidence indicates that stable carbon isotopes can withstand being altered below greenschist facies within unmetamorphosed Precambrian cherts, but previously reported data from the geologic units studied here suggest that isotope fractionation may begin as early as lower- to mid-greenschist facies (ca. 300–400 °C) when considering bulk whole-rock measurements. However, when comparing the thermal alteration and carbon isotope compositions of kerogenous microfossils at high spatial resolution within petrographic thin sections, it appears that $\delta^{13}C_{org}$ values may be largely shielded from the effects of increasing geothermal maturity and that the permineralized organic matter of ancient microorganisms and that of associated kerogenous detritus could retain their primary isotopic composition through greenschist facies metamorphism. The bases of this interpretation are best exemplified by data reported here for carbonaceous microfossils and kerogen from the Auburn Dolomite Member and River Wakefield Formation, both of which have preserved $\delta^{13}C_{org}$ values below or within range of bulk measurements despite having reached peak metamorphic temperatures over ~350 °C (i.e., mid-greenschist facies). $\delta^{13}C_{org}$ values approaching –17‰ for kerogen from the Auburn Dolomite sediments could possibly

represent the onset of fractionation due to thermal alteration, relative to the highest value of –23‰ for the similarly aged Beck Spring Dolomite (~330 °C). However, without coeval $\delta^{13}C_{carb}$ values of inorganic carbon (carbonate) available for reference from the Auburn Dolomite, the potential metabolic fractionation of microbial biomass and the degree to which isotopic exchange between organic and inorganic carbon may have occurred remain poorly constrained. In contrast, for the organics of the River Wakefield Formation the available $\delta^{13}C_{carb}$ data suggest that there has not been excessive carbon isotope exchange due to increasing thermal alteration, and $\delta^{13}C_{org}$ values consistently below –21‰ reported here indicate the presence of relatively well-preserved kerogen associated with carbonaceous microfossils as well as primary evidence of isotopic fractionation (ε_p) in the microbial biomass preserved within the chert.

The findings reported here are of significance to the search for early life on Earth and the application of geochemical techniques to studying microbial remains in thermally altered Precambrian rocks. These data support the possibility of carbon isotope signatures associated with ancient microbial life being preserved in early Archean or Hadean organics, perhaps even graphite, given that there seems to be a preferential preservation of kerogen within certain minerals and lithologies, chert (i.e., microcrystalline quartz) exhibiting characteristics of the "armoring effect" that may help to shield organic carbon from isotopic fractionation or exchange with other carbon-bearing minerals or fluids. The ongoing search for evidence of life in Earth's oldest rocks can thus be guided by further efforts to recover samples of relatively unaltered, well-preserved kerogen (or graphite), ideally in the presence of diagnostic morphological or textural (i.e., stromatolitic) structures permineralized and preserved at high spatial resolutions. These paleobiological explorations are parallel to those aimed at understanding the potential abiotic formation of organic compounds and the initial carbon inventories associated with paleoenvironments (e.g.,

hydrothermal vents, hot springs) of Earth's earliest habitable surfaces. Together, these characterizations will provide a robust geochemical framework in which to interpret possible evidence of early microbial life, including that preserved within the stable carbon isotope composition of the oldest thermally altered organic matter.

TABLES

Geologic unit	Locality	Estimated Age (Ma)	Lithology	Metamorphic grade	RIP*	H/C	Averages of bulk analyses TOC	Averages of bulk analyses $\delta^{13}C_{org}$	Averages of bulk analyses $\delta^{13}C_{carb}$
Kalkberg Limestone	New York, USA	395[a]	Bedded chert	"Low grade"	8.5	Unknown	Unknown	Unknown	~ +2.0[a]
Bungle Bungle Dolomite	Dixon Range, Western Australia	1,364	Stromatolitic chert	Unknown	7.5	0.37	0.08–0.90	-28.1 to -21.6[d]	-0.7
Wumishan Formation	Jixian, China	1,500[b]	Stromatolitic chert	"Essentially unmetamorphosed"	7.4	0.54	0.42	-28.4	~0‰
McLeary Formation	Belcher Islands, Northwest Territories, Canada	2,100	Stromatolitic chert	Subgreenschist	5.8	0.26	0.70	-24.9	-0.4
Vempalle Formation	Andhra Pradesh, India	1,950	Stromatolitic chert	Subgreenschist	5.7	Unknown	0.08	-27.8	-2.3[e] to 0.8[f]
Beck Spring Dolomite	California, USA	750	Stromatolitic chert	"Slightly to moderately metamorphosed"	4.4	0.14	0.35	-26.5** to -15.2**	+4.2***
Auburn Dolomite	Leasingham, South Australia	740[c]	Bedded chert	Lower greenschist	1.5	0.17	0.55	-19.3**	Unknown
River Wakefield Formation	Carrieton, South Australia	775	Bedded chert	Lower greenschist	1.0	0.44	0.88	-14.3	+2.7***

* *Raman Index of Preservation (RIP) values from Schopf et al. (2005).*
** *Kerogen from carbonate (Strauss and Moore, 1992; Strauss et al., 1992b)*
*** *Data from dolomite only (Strauss and Moore, 1992)*
[a] *Husson et al. (2016)*
[b] *Guo et al. (2013)*
[c] *Preiss (2000)*
[d] *Schidlowski et al. (1983), Hayes et al. (1983), Strauss et al. (1992b)*
[e] *Chakrabarti et al. (2011)*
[f] *Khelen et al. (2017)*

Table 3-1. Geologic units studied, ordered by their Raman Index of Preservation (RIP) value from Schopf et al. (2005), with relevant geochemical and lithological information. Estimated age and metamorphic grade for each geologic unit reported by Moore and Schopf (1992) and Schopf et al. (2005) and references therein, and data for approximate averages of bulk analyses come from Strauss et al. (1992b) and Strauss and Moore (1992), unless otherwise noted.

Geologic unit	Fossils analyzed	$\delta^{13}C_{org}$ (‰)	σ	n	RIP*	σ	n	Fitting**	FWHM-D1 (cm^{-1})	Temp (°C)
Kalkberg Limestone	*Multiplicisphaeridium, Micrhystridium,* spheroidal unicells (unnamed)	-24.0	2.8	8	8.2	0.3	5	G	116.2	228
Bungle Bungle Dolomite	*Eomycetopsis,* oscillatoriacean sheaths, colonial spheroids (unnamed)	-26.0	1.8	27	7.4	0.1	14	G	99.8	263
Wumishan Formation	*Eomycetopsis*	-28.4	2.1	12	7.5	0.2	8	G	123.1	213
McLeary Formation	Detrital kerogen only	-25.2	2.3	22	5.6	0.2	8	F	93.2	278
Vempalle Formation	Oscillatoriacean sheaths, cellular filaments (unnamed), spheroidal unicells (unnamed)	-26.1	2.1	25	5.3	0.2	8	F	89.3	286
Beck Spring Dolomite	*Beckspringia communis*	-24.1	1.3	4	4.5	0.2	6	E	69.6	328
Auburn Dolomite	Sheath-like filaments	-21.0	2.4	17	2.2	0.1	7	D	46.5	378
River Wakefield Formation	*Polybessurus,* colonial spheroids (unnamed)	-26.2	3.0	17	2.4	0.3	7	D	46.7	378

** Raman Index of Preservation (RIP) values from Schopf et al. (2005).*

*** Raman deconvolution fittings from Kouketsu et al. (2014).*

Table 3-2. Averages of SIMS carbon isotope values ($\delta^{13}C_{org}$) for kerogenous microfossils and background kerogen from the eight geologic units studied, ordered according to their previously determined thermal maturity. Average $\delta^{13}C_{org}$ and RIP values shown with standard deviation (σ; 1SD) and number of analyses (n). Error for temperature estimates is ±30 °C (Kouketsu et al., 2014).

Geologic Unit	Thin Section	Sample	Analysis	RIP	1SD	Fitting*	FWHM-D1	Temp (°C)
Kalkberg Limestone	On-Dev Kalk-2-C	KALK-16	10036	7.9		G	116.0	229
	On-Dev Kalk-2-C	KALK-22A	10059	8.1		G	116.3	228
	On-Dev Kalk-2-C	KALK-22B	10062	8.1		G	113.8	233
	On-Dev Kalk-2-C	KALK-23	10065	8.7		G	120.3	219
	On-Dev Kalk-2-C	KALK-24	10068	8.1		G	114.8	231
AVERAGE				8.2	0.3		116.2	228
Bungle Bungle Dolomite	BUNG-159-1A	BUNG-2	9695	7.6		G	106.9	248
	BUNG-159-1A	BUNG-3B	9701	7.4		G	99.2	265
	BUNG-159-1A	BUNG-3C	9704	7.5		G	104.4	253
	BUNG-159-1A	BUNG-6B	9707	7.5		G	100.4	262
	BUNG-159-1A	BUNG-7	9760	7.3		G	98.2	267
	BUNG-159-1A	BUNG-9	9766	7.3		G	101.5	260
	BUNG-159-1A	BUNG-10	9769	7.3		G	97.6	268
	BUNG-159-1A	BUNG-11A	9772	7.5		G	101.2	260
	BUNG-159-1A	BUNG-11B	9775	7.4		G	102.0	259
	BUNG-159-1A	BUNG-13A	9789	7.2		G	97.3	269
	BUNG-159-1A	BUNG-13B	9792	7.4		G	95.8	272
	BUNG-159-1A	BUNG-20-BGK1	9795	7.5		G	99.4	264
	BUNG-159-1A	BUNG-21-BGK2	9798	7.4		G	98.9	265
	BUNG-159-1A	BUNG-22-BGK3	9801	7.3		G	94.7	274
AVERAGE				7.4	0.1		99.8	263
Wumishan Formation	WUM-001-a-A2	WUM-3a	9736	7.5		G	123.3	213
	WUM-001-a-A2	WUM-3b	9739	7.4		G	121.4	217
	WUM-001-a-A2	WUM-4	9742	7.4		G	122.4	215
	WUM-001-a-A2	WUM-5	9745	7.4		G	124.8	210
	WUM-001-a-A2	WUM-8	9748	7.5		G	123.8	212
	WUM-001-a-A2	WUM-A2-BG1	9751	7.9		G	124.8	210
	WUM-001-a-A2	WUM-A2-BG2	9754	7.4		G	118.8	223
	WUM-001-a-A2	WUM-A2-BG3	9757	7.9		G	125.3	209
AVERAGE				7.5	0.2		123.1	213
McLeary Formation	MCL-447-1A	MCL-1	9670	5.3		F	90.1	284
	MCL-447-1A	MCL-2	9673	5.7		F	94.1	276
	MCL-447-1A	MCL-4	9676	5.4		F	93.3	277
	MCL-447-1A	MCL-5	9679	5.5		F	92.3	280
	MCL-447-1A	MCL-5	9682	5.5		F	94.8	274
	MCL-447-1A	MCL-6	9685	5.5		F	91.3	282
	MCL-447-1A	MCL-7	9688	5.7		F	93.1	278
	MCL-447-1A	MCL-8	9692	5.9		F	96.9	270
AVERAGE				5.6	0.2		93.2	278
Vempalle Formation	CUD-1-4-B	VEM-1	9804	5.5		F	95.9	272
	CUD-1-4-B	VEM-1B	9807	5.2		F	87.6	290
	CUD-1-4-B	VEM-6	9810	5.6		F	93.8	276
	CUD-1-4-B	VEM-6B	9813	5.6		F	91.2	282
	CUD-1-4-B	VEM-BGK2	9819	5.3		F	87.5	290
	CUD-1-9-A	VEM-BGK1	9825	5.2		F	85.9	293
	CUD-1-9-A	VEM-BGK2	9828	4.9		F	83.6	298
	CUD-1-9-A	VEM-9	9831	5.1		F	88.5	288
AVERAGE				5.3	0.2		89.3	286
Beck Spring Dolomite	BK-Spr-4-B	BECK-1	9834	4.4		E	72.6	322
	BK-Spr-4-B	BECK-2	9837	4.3		E	73.5	320
	BK-Spr-4-B	BECK-3	9840	4.6		E	68.5	331
	BK-Spr-4-B	BECK-4	9843	4.6		E	71.1	325
	BK-Spr-4-B	BECK-BGK1	9847	4.3		E	71.7	324
	BK-Spr-4-B	BECK-BGK2	9850	4.6		E	59.9	349
AVERAGE				4.5	0.2		69.6	328
Auburn Dolomite	AD-BF-1-1-D	AUB-2	9961	2.4		D	47.1	377
	AD-BF-1-1-D	AUB-12	9964	2.2		D	45.5	380
	AD-BF-1-1-D	AUB-16	9970	2.2		D	45.9	379
	AD-BF-1-1-D	AUB-11A	9973	2.3		D	46.8	377
	AD-BF-1-1-D	AUB-11C	9979	2.2		D	47.1	377
	AD-BF-1-1-D	AUB-15	9982	2.1		D	46.1	379
	AD-BF-1-1-D	AUB-13B	9988	2.2		D	47.2	377
AVERAGE				2.2	0.1		46.5	378
River Wakefield Subgroup	RWG-BF-2-4-B	RW-3	9919	2.6		D	49.6	371
	RWG-BF-2-4-B	RW-4	9922	2.4		D	49.7	371
	RWG-BF-2-4-B	RW-5	9925	2.0		D	40.7	390
	RWG-BF-2-4-B	RW-6	9928	2.6		D	48.3	374
	RWG-BF-2-4-B	RW-7	9931	2.0		D	42.2	387
	RWG-BF-2-4-B	RW-8	9934	2.7		D	49.9	371
	RWG-BF-2-4-B	RW-9	9937	2.6		D	46.5	378
AVERAGE				2.4	0.3		46.7	378

**From Kouketsu et al. (2014)*

Table 3-3. Data for Raman spectroscopy measurements of microfossils and detrital kerogen.

Date	Filename	Analysis ID	Thin section	Description	$\delta^{13}C_{corrected}$ (‰, VPDB)	Error (±)	$\delta^{13}C_{2\text{-point adjusted}}$ (‰, VPDB)	$\delta^{13}C_{raw}$ (‰, VPDB)	±2 SE* (‰)	$^{12}C_2^-$ (cps)	$^{12}C_2^-$ rel (%)	$^{133}Cs^+$ intensity (nA)	α_{SIMS}	±2 SD** (‰)	IMF (‰)	SEM
Wumishan Formation																
6/10/19	WUM-3@21.asc	19	WUM-001-a-A2	*Eomycetopsis*	-29.7	1.9	-29.4	-40.1	3.65	2.4E+05	23%	1.35	0.9892	3.26	-10.43	0.576
6/10/19	WUM-3@23.asc	21	WUM-001-a-A2	*Eomycetopsis*	-31.2	2.0	-30.8	-41.6	3.75	2.3E+05	23%	1.35	0.9892	3.26	-10.43	0.576
6/10/19	WUM-4@25.asc	23	WUM-001-a-A2	*Eomycetopsis*	-27.6	1.8	-27.6	-38.1	3.34	2.2E+05	21%	1.36	0.9892	3.26	-10.43	0.576
6/10/19	WUM-4@26.asc	24	WUM-001-a-A2	*Eomycetopsis*	-30.9	1.7	-30.6	-41.4	3.16	2.5E+05	24%	1.36	0.9892	3.26	-10.43	0.576
6/10/19	WUM-4@27.asc	25	WUM-001-a-A2	*Eomycetopsis*	-25.4	1.4	-25.6	-35.9	2.55	3.1E+05	30%	1.37	0.9892	3.26	-10.43	0.576
6/10/19	WUM-5@28.asc	26	WUM-001-a-A2	*Eomycetopsis*	-29.0	1.0	-28.8	-39.4	1.55	8.3E+05	80%	1.37	0.9892	3.26	-10.43	0.576
6/10/19	WUM-8@29.asc	27	WUM-001-a-A2	*Eomycetopsis*	-30.2	1.1	-29.9	-40.6	1.91	4.0E+05	38%	1.37	0.9892	3.26	-10.43	0.576
6/10/19	WUM-8@30.asc	28	WUM-001-a-A2	*Eomycetopsis* (background fossil)	-29.7	1.2	-29.5	-40.2	1.99	4.5E+05	44%	1.37	0.9892	3.26	-10.43	0.576
6/10/19	WUM-8@31.asc	29	WUM-001-a-A2	*Eomycetopsis* (background fossil)	-27.6	1.1	-27.5	-38.0	1.77	5.0E+05	48%	1.37	0.9892	3.26	-10.43	0.576
6/10/19	WUM-BGK1@32.asc	30	WUM-001-a-A2	Background kerogen (stromatolitic)	-25.7	1.5	-25.8	-36.2	2.72	2.8E+05	27%	1.37	0.9892	3.26	-10.43	0.576
6/10/19	WUM-BGK1@33.asc	31	WUM-001-a-A2	Background kerogen (stromatolitic)	-25.5	1.4	-25.7	-36.0	2.46	3.1E+05	30%	1.37	0.9892	3.26	-10.43	0.576
6/10/19	WUM-BGK2@34.asc	32	WUM-001-a-A2	Background kerogen	-27.9	0.8	-27.8	-38.4	1.01	1.2E+06	114%	1.37	0.9892	3.26	-10.43	0.576
AVERAGE					-28.4	1.4	-28.2	-38.8	2.49	4.3E+05	42%	1.36	0.9892	3.26	-10.43	0.576
McLeary Formation																
6/11/19	MCL-1@46.asc	44	MCL-447-1A	Detrital kerogen	-23.3	0.8	-23.7	-33.9	1.00	1.1E+06	160%	1.23	0.9892	3.21	-10.50	0.567
6/11/19	MCL-1@47.asc	45	MCL-447-1A	Detrital kerogen	-24.3	0.8	-24.6	-34.9	1.08	1.6E+06	229%	1.23	0.9892	3.21	-10.50	0.567
6/11/19	MCL-1@48.asc	46	MCL-447-1A	Detrital kerogen	-23.6	0.9	-24.0	-34.2	1.32	1.0E+06	147%	1.23	0.9892	3.21	-10.50	0.567
6/11/19	MCL-2@49.asc	47	MCL-447-1A	Detrital kerogen	-23.6	0.7	-24.0	-34.2	0.72	1.2E+06	173%	1.23	0.9892	3.21	-10.50	0.567
6/11/19	MCL-2@50.asc	48	MCL-447-1A	Detrital kerogen	-22.5	1.0	-23.0	-33.1	1.76	6.6E+05	96%	1.23	0.9892	3.21	-10.50	0.567
6/11/19	MCL-2@51.asc	49	MCL-447-1A	Detrital kerogen	-27.9	0.8	-27.9	-38.4	1.00	1.1E+06	162%	1.24	0.9892	3.21	-10.50	0.567
6/11/19	MCL-2@52.asc	50	MCL-447-1A	Detrital kerogen	-26.4	0.7	-26.5	-37.0	0.73	1.6E+06	236%	1.24	0.9892	3.21	-10.50	0.567
6/11/19	MCL-4@53.asc	51	MCL-447-1A	Detrital kerogen	-26.6	0.9	-26.7	-37.2	1.48	1.1E+06	161%	1.24	0.9892	3.21	-10.50	0.567
6/11/19	MCL-4@54.asc	52	MCL-447-1A	Detrital kerogen	-27.4	0.8	-27.4	-37.9	1.15	1.7E+06	240%	1.25	0.9892	3.21	-10.50	0.567
6/11/19	MCL-4@55.asc	53	MCL-447-1A	Detrital kerogen	-25.2	0.9	-25.4	-35.8	1.44	5.9E+05	86%	1.25	0.9892	3.21	-10.50	0.567
6/11/19	MCL-5@56.asc	54	MCL-447-1A	Detrital kerogen	-26.0	0.8	-26.2	-36.6	1.16	1.2E+06	166%	1.25	0.9892	3.21	-10.50	0.567
6/11/19	MCL-5@57.asc	55	MCL-447-1A	Detrital kerogen	-26.1	0.9	-26.2	-36.6	1.44	7.1E+05	103%	1.22	0.9892	3.21	-10.50	0.567
6/11/19	MCL-5@58.asc	56	MCL-447-1A	Filamentous texture	-24.0	1.3	-24.3	-34.6	2.30	5.5E+05	80%	1.22	0.9892	3.21	-10.50	0.567
6/11/19	MCL-6@59.asc	57	MCL-447-1A	Detrital kerogen	-25.8	0.8	-25.9	-36.3	1.05	1.1E+06	154%	1.22	0.9892	3.21	-10.50	0.567
6/11/19	MCL-6@60.asc	58	MCL-447-1A	Detrital kerogen	-27.0	0.7	-27.1	-37.6	0.94	1.7E+06	249%	1.22	0.9892	3.21	-10.50	0.567
6/11/19	MCL-6@61.asc	59	MCL-447-1A	Detrital kerogen	-29.0	0.9	-28.9	-39.5	1.52	8.7E+05	126%	1.22	0.9892	3.21	-10.50	0.567
6/11/19	MCL-7@62.asc	60	MCL-447-1A	Coccoidal texture	-23.7	1.3	-24.1	-34.3	2.27	5.5E+05	79%	1.22	0.9892	3.21	-10.50	0.567
6/11/19	MCL-7@63.asc	61	MCL-447-1A	Coccoidal texture	-29.6	1.0	-29.4	-40.1	1.60	5.8E+05	84%	1.22	0.9892	3.21	-10.50	0.567
6/11/19	MCL-7@64.asc	62	MCL-447-1A	Coccoidal texture	-21.9	1.5	-22.4	-32.5	2.77	3.0E+05	43%	1.22	0.9892	3.21	-10.50	0.567
6/11/19	MCL-7@65.asc	63	MCL-447-1A	Coccoidal texture	-20.2	1.1	-20.9	-30.9	1.89	4.0E+05	57%	1.22	0.9892	3.21	-10.50	0.567
6/11/19	MCL-8@66.asc	64	MCL-447-1A	Detrital kerogen	-25.9	1.1	-26.1	-36.5	1.95	4.7E+05	68%	1.23	0.9892	3.21	-10.50	0.567
6/11/19	MCL-8@67.asc	65	MCL-447-1A	Spheroidal unicell?	-24.2	0.7	-24.5	-34.8	0.95	1.4E+06	203%	1.24	0.9892	3.21	-10.50	0.567
AVERAGE					-25.2	0.9	-25.4	-35.8	1.43	9.8E+05	141%	1.23	0.9892	3.21	-10.50	0.567
Bungle Bungle Formation																
6/11/19	BUNG-2@72.asc	70	BUNG-159-1A	*Eomycetopsis*	-29.8	2.0	-30.3	-41.0	3.88	2.5E+05	33%	1.29	0.9885	3.37	-11.17	0.595
6/11/19	BUNG-2@73.asc	71	BUNG-159-1A	*Eomycetopsis*	-27.7	1.3	-28.3	-38.9	2.21	4.2E+05	54%	1.29	0.9885	3.37	-11.17	0.595
6/11/19	BUNG-3@74.asc	72	BUNG-159-1A	*Eomycetopsis*	-25.3	0.8	-26.1	-36.5	1.17	7.9E+05	102%	1.29	0.9885	3.37	-11.17	0.595
6/11/19	BUNG-3@75.asc	73	BUNG-159-1A	*Eomycetopsis*	-26.6	0.7	-27.3	-37.8	0.76	3.2E+06	414%	1.30	0.9885	3.37	-11.17	0.595
6/11/19	BUNG-6A@76.asc	74	BUNG-159-1A	Large sheath (oscillatoriacean)	-24.0	0.8	-25.0	-35.3	1.08	9.3E+05	120%	1.30	0.9885	3.37	-11.17	0.595
6/11/19	BUNG-6A@77.asc	75	BUNG-159-1A	Large sheath (oscillatoriacean)	-24.8	0.7	-25.7	-36.1	0.85	1.4E+06	181%	1.30	0.9885	3.37	-11.17	0.595
6/11/19	BUNG-6B@78.asc	76	BUNG-159-1A	Large sheath (oscillatoriacean)	-28.0	0.8	-28.6	-39.3	0.95	1.5E+06	197%	1.30	0.9885	3.37	-11.17	0.595
6/11/19	BUNG-6B@79.asc	77	BUNG-159-1A	Large sheath (oscillatoriacean)	-27.8	0.8	-28.4	-39.0	1.09	1.4E+06	179%	1.30	0.9885	3.37	-11.17	0.595
6/11/19	BUNG-7@80.asc	78	BUNG-159-1A	*Eomycetopsis*	-23.7	1.5	-24.7	-34.9	2.66	3.6E+05	47%	1.31	0.9885	3.37	-11.17	0.595
6/11/19	BUNG-8A@81.asc	79	BUNG-159-1A	*Eomycetopsis*	-25.3	1.3	-26.2	-36.6	2.31	4.8E+05	61%	1.31	0.9885	3.37	-11.17	0.595
6/11/19	BUNG-9@82.asc	80	BUNG-159-1A	*Eomycetopsis*	-23.9	1.1	-24.9	-35.2	1.78	5.4E+05	70%	1.31	0.9885	3.37	-11.17	0.595
6/11/19	BUNG-10@83.asc	81	BUNG-159-1A	*Eomycetopsis*	-24.7	1.1	-25.6	-36.0	1.73	6.2E+05	80%	1.31	0.9885	3.37	-11.17	0.595
6/11/19	BUNG-10@84.asc	82	BUNG-159-1A	*Eomycetopsis*	-24.3	1.0	-25.2	-35.6	1.58	8.2E+05	106%	1.31	0.9885	3.37	-11.17	0.595
6/11/19	BUNG-11@85.asc	83	BUNG-159-1A	*Eomycetopsis*	-24.3	1.0	-25.2	-35.5	1.50	6.9E+05	89%	1.32	0.9885	3.37	-11.17	0.595
6/11/19	BUNG-11@86.asc	84	BUNG-159-1A	*Eomycetopsis*	-25.3	1.1	-26.1	-36.5	1.75	3.0E+05	39%	1.32	0.9885	3.37	-11.17	0.595
6/11/19	BUNG-12@87.asc	85	BUNG-159-1A	Colonial spheroids?	-26.7	1.1	-27.4	-37.9	1.82	5.4E+05	70%	1.32	0.9885	3.37	-11.17	0.595
6/11/19	BUNG-12@88.asc	86	BUNG-159-1A	Colonial spheroids?	-26.6	1.4	-27.3	-37.8	2.56	4.8E+05	63%	1.32	0.9885	3.37	-11.17	0.595
6/11/19	BUNG-12@89.asc	87	BUNG-159-1A	Colonial spheroids?	-27.4	0.8	-28.1	-38.6	1.12	1.2E+06	155%	1.32	0.9885	3.37	-11.17	0.595
6/11/19	BUNG-13A@95.asc	93	BUNG-159-1A	*Eomycetopsis*	-26.6	0.9	-27.4	-37.9	1.37	6.6E+05	73%	1.33	0.9884	3.54	-11.26	0.625
6/11/19	BUNG-13B@96.asc	94	BUNG-159-1A	Colonial spheroids?	-26.7	0.8	-27.5	-38.0	1.05	1.1E+06	119%	1.32	0.9884	3.54	-11.26	0.625
6/11/19	BUNG-20-BGK1@97.asc	95	BUNG-159-1A	Background kerogen	-31.1	1.1	-31.5	-42.4	1.88	6.1E+05	68%	1.33	0.9884	3.54	-11.26	0.625

6/11/19	BUNG-20-BGK1@98.asc	96	BUNG-159-1A	Background kerogen	-25.1	0.9	-26.0	-36.4	1.42	3.8E+05	42%	1.32	0.9884	3.54	-11.26	0.625
6/11/19	BUNG-21-BGK2@99.asc	97	BUNG-159-1A	Background kerogen	-27.0	1.2	-27.8	-38.3	2.13	3.5E+05	39%	1.33	0.9884	3.54	-11.26	0.625
6/11/19	BUNG-21-BGK2@100.asc	98	BUNG-159-1A	Background kerogen	-24.7	2.1	-25.7	-36.1	4.08	2.1E+05	24%	1.32	0.9884	3.54	-11.26	0.625
6/11/19	BUNG-22-BGK3@101.asc	99	BUNG-159-1A	Background kerogen	-23.4	0.9	-24.5	-34.8	1.39	8.1E+05	89%	1.32	0.9884	3.54	-11.26	0.625
6/11/19	BUNG-22-BGK3@102.asc	100	BUNG-159-1A	Background kerogen	-26.0	1.1	-26.8	-37.3	1.72	4.0E+05	44%	1.32	0.9884	3.54	-11.26	0.625
6/11/19	BUNG-22-BGK3@103.asc	101	BUNG-159-1A	Background kerogen	-26.3	1.1	-27.1	-37.6	1.79	6.2E+05	69%	1.32	0.9884	3.54	-11.26	0.625
AVERAGE					-26.0	1.1	-26.8	-37.3	1.8	7.8E+05	97%	1.31	0.9884	3.42	-11.20	0.605
Vempalle Formation																
6/12/19	VEM-1@115.asc	113	CUD-1-4-B	Oscillatoriacean sheath	-26.2	0.9	-27.3	-37.8	1.48	5.3E+05	57%	1.25	0.9882	2.47	-11.47	0.436
6/12/19	VEM-1@116.asc	114	CUD-1-4-B	Oscillatoriacean sheath	-23.3	0.9	-24.6	-34.8	1.47	7.0E+05	75%	1.25	0.9882	2.47	-11.47	0.436
6/12/19	VEM-1@117.asc	115	CUD-1-4-B	Oscillatoriacean sheath	-25.1	0.7	-26.3	-36.7	1.16	1.1E+06	115%	1.26	0.9882	2.47	-11.47	0.436
6/12/19	VEM-1@118.asc	116	CUD-1-4-B	Oscillatoriacean sheath	-27.5	0.6	-28.4	-39.0	0.91	1.8E+06	196%	1.26	0.9882	2.47	-11.47	0.436
6/12/19	VEM-1B@119.asc	117	CUD-1-4-B	Cellular filament (unnamed)	-27.5	0.7	-28.4	-39.0	1.09	1.3E+06	139%	1.26	0.9882	2.47	-11.47	0.436
6/12/19	VEM-1B@120.asc	118	CUD-1-4-B	Cellular filament (unnamed)	-25.6	0.7	-26.7	-37.1	1.18	1.1E+06	115%	1.27	0.9882	2.47	-11.47	0.436
6/12/19	VEM-6@121.asc	119	CUD-1-4-B	Oscillatoriacean sheath	-25.8	0.7	-26.9	-37.3	1.11	1.9E+06	203%	1.28	0.9882	2.47	-11.47	0.436
6/12/19	VEM-6@122.asc	120	CUD-1-4-B	Oscillatoriacean sheath	-29.5	0.5	-30.3	-41.0	0.66	2.9E+06	310%	1.28	0.9882	2.47	-11.47	0.436
6/12/19	VEM-6@123.asc	121	CUD-1-4-B	Oscillatoriacean sheath	-27.0	0.6	-27.9	-38.5	0.74	3.1E+06	330%	1.28	0.9882	2.47	-11.47	0.436
6/12/19	VEM-6@124.asc	122	CUD-1-4-B	Oscillatoriacean sheath	-28.3	0.6	-29.1	-39.8	0.88	2.6E+06	281%	1.28	0.9882	2.47	-11.47	0.436
6/12/19	VEM-6@125.asc	123	CUD-1-4-B	Oscillatoriacean sheath	-26.4	0.6	-27.4	-38.0	0.93	1.9E+06	202%	1.27	0.9882	2.47	-11.47	0.436
6/12/19	VEM-BGK1@126.asc	124	CUD-1-4-B	Background kerogen	-32.4	0.5	-32.9	-43.9	0.55	4.3E+06	462%	1.28	0.9882	2.47	-11.47	0.436
6/12/19	VEM-BGK1@127.asc	125	CUD-1-4-B	Background kerogen	-24.6	0.6	-25.8	-36.2	0.77	2.0E+06	216%	1.27	0.9882	2.47	-11.47	0.436
6/12/19	VEM-BGK1@128.asc	126	CUD-1-4-B	Background kerogen	-23.8	0.8	-25.1	-35.4	1.34	6.1E+05	65%	1.28	0.9882	2.47	-11.47	0.436
6/12/19	VEM-BGK2@129.asc	127	CUD-1-4-B	Background kerogen	-26.3	1.2	-27.3	-37.9	2.13	5.0E+05	53%	1.28	0.9882	2.47	-11.47	0.436
6/12/19	VEM-BGK2@130.asc	128	CUD-1-4-B	Background kerogen	-27.8	1.0	-28.7	-39.3	1.87	5.9E+05	63%	1.28	0.9882	2.47	-11.47	0.436
6/12/19	VEM-BGK2@131.asc	129	CUD-1-4-B	Background kerogen	-26.6	1.2	-27.6	-38.1	2.15	4.4E+05	47%	1.28	0.9882	2.47	-11.47	0.436
6/12/19	VEM-9@137.asc	135	CUD-1-9-A	Spheroidal unicell (unnamed)	-23.8	1.2	-25.4	-35.7	2.09	3.3E+05	27%	1.39	0.9877	2.84	-11.87	0.502
6/12/19	VEM-7@139.asc	137	CUD-1-9-A	Spheroidal unicell (unnamed)	-26.4	1.5	-27.7	-38.3	2.90	2.1E+05	18%	1.39	0.9877	2.84	-11.87	0.502
6/12/19	VEM-BGK1@140.asc	138	CUD-1-9-A	Background kerogen	-25.8	1.7	-27.2	-37.7	3.16	3.2E+05	26%	1.39	0.9877	2.84	-11.87	0.502
6/12/19	VEM-BGK1@141.asc	139	CUD-1-9-A	Background kerogen	-23.8	1.1	-25.4	-35.7	1.93	4.8E+05	40%	1.39	0.9877	2.84	-11.87	0.502
6/12/19	VEM-BGK1@142.asc	140	CUD-1-9-A	Background kerogen	-24.3	1.6	-25.9	-36.3	2.97	3.8E+05	31%	1.39	0.9877	2.84	-11.87	0.502
6/12/19	VEM-BGK2@143.asc	141	CUD-1-9-A	Background kerogen	-26.0	1.1	-27.4	-38.0	2.01	3.4E+05	28%	1.39	0.9877	2.84	-11.87	0.502
6/12/19	VEM-BGK2@144.asc	142	CUD-1-9-A	Background kerogen	-25.2	1.3	-26.7	-37.1	2.42	2.9E+05	24%	1.39	0.9877	2.84	-11.87	0.502
6/12/19	VEM-BGK2@145.asc	143	CUD-1-9-A	Background kerogen	-22.9	1.1	-24.6	-34.9	2.03	4.7E+05	39%	1.39	0.9877	2.84	-11.87	0.502
AVERAGE					-26.1	0.9	-27.2	-37.7	1.60	1.2E+06	126%	1.31	0.9880	2.59	-11.60	0.457

Table 3-4. SIMS $\delta^{13}C$ data from session 1 (6/10–6/12/2019).

Date	Filename	Analysis ID	Thin section	Description	$\delta^{13}C_{corrected}$ (‰ VPDB)	Error (±)	$\delta^{13}C_{2\text{-point adjusted}}$ (‰, VPDB)	$\delta^{13}C_{raw}$ (‰ VPDB)	±2 SE* (‰)	$^{12}C_2^-$ (cps)	$^{12}C_2^-$ nil (%)	$^{133}Cs^+$ intensity (nA)	α_{SIMS}	±2 SD** (‰)	IMF (‰)	SEM
River Wakefield Formation																
10/29/19	RWG-2-BGK1@32.asc	32	RWG-BF-2-4-B	Background kerogen	-23.9	1.9	-21.9	-43.0	3.6	2.5E+05	9%	0.45	0.9804	3.58	-19.295	0.633
10/29/19	RWG-2-BGK1@33.asc	33	RWG-BF-2-4-B	Background kerogen	-23.9	1.9	-21.8	-42.9	3.6	2.6E+05	9%	0.44	0.9804	3.58	-19.295	0.633
10/29/19	RWG-2-BGK1@34.asc	34	RWG-BF-2-4-B	Background kerogen	-25.4	1.3	-23.1	-44.4	2.2	4.8E+05	17%	0.43	0.9804	3.58	-19.295	0.633
10/29/19	RWG-2-BGK1@35.asc	35	RWG-BF-2-4-B	Background kerogen	-24.5	1.1	-22.4	-43.6	1.9	4.2E+05	15%	0.43	0.9804	3.58	-19.295	0.633
10/29/19	RWG-2-RW4@36.asc	36	RWG-BF-2-4-B	*Polybessurus*	-29.8	1.3	-26.8	-48.8	2.3	3.9E+05	14%	0.47	0.9804	3.58	-19.295	0.633
10/29/19	RWG-2-RW4@37.asc	37	RWG-BF-2-4-B	*Polybessurus*	-32.3	1.5	-28.9	-51.2	2.8	4.6E+05	17%	0.44	0.9804	3.58	-19.295	0.633
10/29/19	RWG-2-RW4@38.asc	38	RWG-BF-2-4-B	*Polybessurus*	-30.9	1.5	-27.7	-49.8	2.6	3.2E+05	11%	0.48	0.9804	3.58	-19.295	0.633
10/29/19	RWG-2-RW5@40.asc	40	RWG-BF-2-4-B	*Polybessurus*	-27.8	2.1	-25.1	-46.8	4.1	3.2E+05	11%	0.47	0.9804	3.58	-19.295	0.633
10/29/19	RWG-2-RW6@41.asc	41	RWG-BF-2-4-B	Colonial spheroids (unnamed)	-26.0	1.3	-23.6	-45.0	2.4	4.7E+05	17%	0.50	0.9804	3.58	-19.295	0.633
10/29/19	RWG-2-RW6@42.asc	42	RWG-BF-2-4-B	Colonial spheroids (unnamed)	-23.3	1.5	-21.3	-42.4	2.6	3.7E+05	13%	0.48	0.9804	3.58	-19.295	0.633
10/29/19	RWG-2-RW6@43.asc	43	RWG-BF-2-4-B	Colonial spheroids (unnamed)	-21.4	1.6	-19.8	-40.6	3.0	3.4E+05	12%	0.47	0.9804	3.58	-19.295	0.633
10/29/19	RWG-2-RW10@44.asc	44	RWG-BF-2-4-B	*Polybessurus*	-24.2	1.2	-22.1	-43.3	2.0	5.3E+05	19%	0.45	0.9804	3.58	-19.295	0.633
10/29/19	RWG-2-RW10@45.asc	45	RWG-BF-2-4-B	*Polybessurus*	-28.4	0.9	-25.6	-47.4	1.2	1.2E+06	44%	0.43	0.9804	3.58	-19.295	0.633
10/29/19	RWG-2-RW10@46.asc	46	RWG-BF-2-4-B	*Polybessurus*	-26.8	1.8	-24.3	-45.9	3.4	3.8E+05	14%	0.43	0.9804	3.58	-19.295	0.633
10/29/19	RWG-2-RW10@47.asc	47	RWG-BF-2-4-B	*Polybessurus*	-28.1	1.1	-25.3	-47.1	1.8	9.5E+05	34%	0.42	0.9804	3.58	-19.295	0.633
10/29/19	RWG-2-RW10@48.asc	48	RWG-BF-2-4-B	*Polybessurus*	-26.4	2.0	-23.9	-45.4	3.7	7.9E+05	28%	0.42	0.9804	3.58	-19.295	0.633
10/30/19	RWG-2-RW13B@67.asc	67	RWG-BF-2-4-B	Colonial spheroids (unnamed)	-23.0	1.9	-21.2	-42.3	2.3	8.0E+05	34%	0.40	0.9803	3.10	-19.466	1.549
AVERAGE					-26.2	1.5	-23.8	-45.3	2.7	5.2E+05	19%	0.45	0.9804	3.55	-19.305	0.687
Auburn Dolomite Member																
10/30/19	AUB-1-2@78.asc	78	AD-BF-1-1-D	Sheath-like filament	-23.1	0.7	-21.6	-42.7	1.1	2.6E+06	127%	0.18	0.9799	2.08	-19.838	0.368
10/30/19	AUB-1-2@79.asc	79	AD-BF-1-1-D	Sheath-like filament	-22.0	0.7	-20.7	-41.7	1.3	3.6E+06	175%	0.17	0.9799	2.08	-19.838	0.368
10/30/19	AUB-1-11bg@80.asc	80	AD-BF-1-1-D	Background fossil kerogen	-19.7	0.9	-18.8	-39.5	1.5	5.3E+05	26%	0.42	0.9799	2.08	-19.838	0.368
10/30/19	AUB-1-11A@81.asc	81	AD-BF-1-1-D	Sheath-like filament	-20.5	0.7	-19.4	-40.2	1.1	1.7E+06	85%	0.38	0.9799	2.08	-19.838	0.368
10/30/19	AUB-1-11A@82.asc	82	AD-BF-1-1-D	Sheath-like filament	-18.2	0.8	-17.6	-38.0	1.3	1.1E+06	53%	0.38	0.9799	2.08	-19.838	0.368
10/30/19	AUB-1-11B@83.asc	83	AD-BF-1-1-D	Sheath-like filament	-20.9	0.6	-19.8	-40.6	1.0	1.9E+06	95%	0.36	0.9799	2.08	-19.838	0.368
10/30/19	AUB-1-11B@84.asc	84	AD-BF-1-1-D	Sheath-like filament	-22.5	0.7	-21.1	-42.1	1.3	1.2E+06	58%	0.36	0.9799	2.08	-19.838	0.368
10/30/19	AUB-1-12@85.asc	85	AD-BF-1-1-D	Sheath-like filament	-24.4	1.2	-22.7	-44.0	2.2	5.3E+05	26%	0.16	0.9799	2.08	-19.838	0.368
10/30/19	AUB-1-13@86.asc	86	AD-BF-1-1-D	Sheath-like filament	-21.8	1.6	-20.6	-41.5	3.1	8.6E+05	42%	0.13	0.9799	2.08	-19.838	0.368
10/30/19	AUB-1-14@88.asc	88	AD-BF-1-1-D	Background kerogen (stromatolitic)	-20.5	0.6	-19.5	-40.2	0.9	2.4E+06	118%	0.18	0.9799	2.08	-19.838	0.368
10/30/19	AUB-1-14@90.asc	90	AD-BF-1-1-D	Background kerogen (stromatolitic)	-20.9	0.9	-19.8	-40.6	1.7	9.0E+05	44%	0.16	0.9799	2.08	-19.838	0.368
10/30/19	AUB-1-15@91.asc	91	AD-BF-1-1-D	Background kerogen (clast)	-17.0	1.2	-16.5	-36.8	2.2	5.9E+05	29%	0.28	0.9799	2.08	-19.838	0.368
10/30/19	AUB-1-15@92.asc	92	AD-BF-1-1-D	Background kerogen (clast)	-20.3	1.1	-19.3	-40.0	2.1	5.8E+05	29%	0.26	0.9799	2.08	-19.838	0.368
10/30/19	AUB-1-16@93.asc	93	AD-BF-1-1-D	Background kerogen (clast)	-18.5	0.9	-17.8	-38.3	1.6	5.7E+05	28%	0.49	0.9799	2.08	-19.838	0.368
10/30/19	AUB-1-16@94.asc	94	AD-BF-1-1-D	Background kerogen (clast)	-26.2	0.7	-24.3	-45.8	1.2	1.1E+06	53%	0.48	0.9799	2.08	-19.838	0.368
10/30/19	AUB-1-16@95.asc	95	AD-BF-1-1-D	Background kerogen (clast)	-22.2	1.3	-20.9	-41.9	2.5	2.8E+05	14%	0.47	0.9799	2.08	-19.838	0.368
10/30/19	AUB-1-16@96.asc	96	AD-BF-1-1-D	Background kerogen (clast)	-17.4	1.0	-16.9	-37.1	2.0	6.7E+05	33%	0.46	0.9799	2.08	-19.838	0.368
AVERAGE					-21.0	0.9	-19.8	-40.6	1.6	1.2E+06	61%	0.31	0.9799	2.08	-19.838	0.368
Beck Spring																
10/31/19	BkSpr-BGK1@108.asc	108	BK-Spr-4-B	Background kerogen	-23.0	1.1	-23.2	-44.6	1.9	4.4E+05	19%	0.04	0.9779	2.95	-21.829	0.522
10/31/19	BkSpr-BGF@109.asc	109	BK-Spr-4-B	Background fossil kerogen	-24.8	1.3	-24.7	-46.3	2.3	8.7E+05	37%	0.04	0.9779	2.95	-21.829	0.522
10/31/19	BkSpr-BECK2@110.asc	110	BK-Spr-4-B	*Beckspringia communis*	-25.6	0.9	-25.4	-47.2	1.4	1.5E+06	62%	0.03	0.9779	2.95	-21.829	0.522
10/31/19	BkSpr-BGK2@113.asc	113	BK-Spr-4-B	Background kerogen	-23.1	1.3	-23.3	-44.7	2.3	4.0E+05	17%	0.27	0.9779	2.95	-21.829	0.522
AVERAGE					-24.1	1.1	-24.2	-45.7	2.0	7.9E+05	34%	0.10	0.9779	2.95	-21.829	0.522
Kalkberg Formation																
10/31/19	KALK-13@114.asc	114	On-Dev-Kalk-2-C	*Multiplicisphaeridium*	-22.0	1.0	-22.4	-43.7	1.6	4.9E+05	21%	0.21	0.9779	2.95	-21.829	0.522
10/31/19	KALK-13@115.asc	115	On-Dev-Kalk-2-C	*Multiplicisphaeridium*	-20.9	0.6	-21.5	-42.6	0.7	4.7E+06	200%	0.21	0.9779	2.95	-21.829	0.522
10/31/19	KALK-13@116.asc	116	On-Dev-Kalk-2-C	*Multiplicisphaeridium*	-20.8	0.6	-21.4	-42.5	0.4	8.0E+06	342%	0.15	0.9779	2.95	-21.829	0.522
10/31/19	KALK-19@118.asc	118	On-Dev-Kalk-2-C	*Micrhystridium*	-24.2	1.5	-24.2	-45.7	2.8	4.1E+05	17%	0.28	0.9779	2.95	-21.829	0.522
10/31/19	KALK-19@119.asc	119	On-Dev-Kalk-2-C	*Micrhystridium*	-25.7	0.8	-25.4	-47.2	1.1	2.3E+06	100%	0.25	0.9779	2.95	-21.829	0.522
10/31/19	KALK-19@120.asc	120	On-Dev-Kalk-2-C	*Micrhystridium*	-29.0	0.8	-28.2	-50.5	1.2	1.1E+06	47%	0.23	0.9779	2.95	-21.829	0.522
10/31/19	KALK-20@121.asc	121	On-Dev-Kalk-2-C	*Micrhystridium*	-23.8	0.7	-23.9	-45.4	1.1	1.2E+06	50%	0.16	0.9779	2.95	-21.829	0.522
10/31/19	KALK-22B@124.asc	124	On-Dev-Kalk-2-C	Spheroidal unicell (unnamed)	-25.9	0.7	-25.7	-47.5	0.9	1.9E+06	81%	0.16	0.9779	2.95	-21.829	0.522
AVERAGE					-24.0	0.8	-24.1	-45.6	1.2	2.5E+06	107%	0.21	0.9779	2.95	-21.829	0.522

Table 3-5. SIMS $\delta^{13}C$ data from session 2 (10/29–10/31/2019).

FIGURES

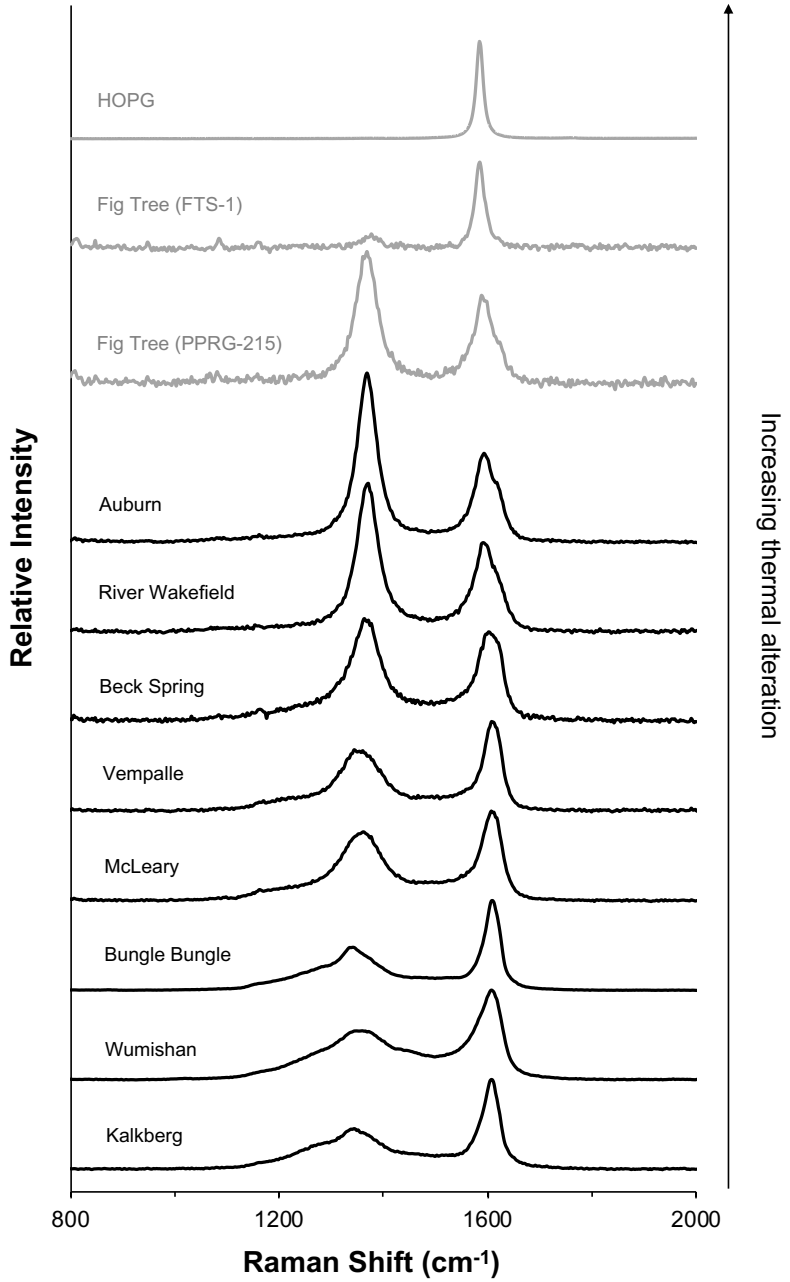

Figure 3-1. Raman spectra of kerogenous microfossils (black) for each of the geologic units studied. Offset at the top are Raman spectra of kerogen for the standards from the Fig Tree chert (PPRG-215 and FTS-1) and highly oriented pyrolytic graphite (HOPG) standard (gray).

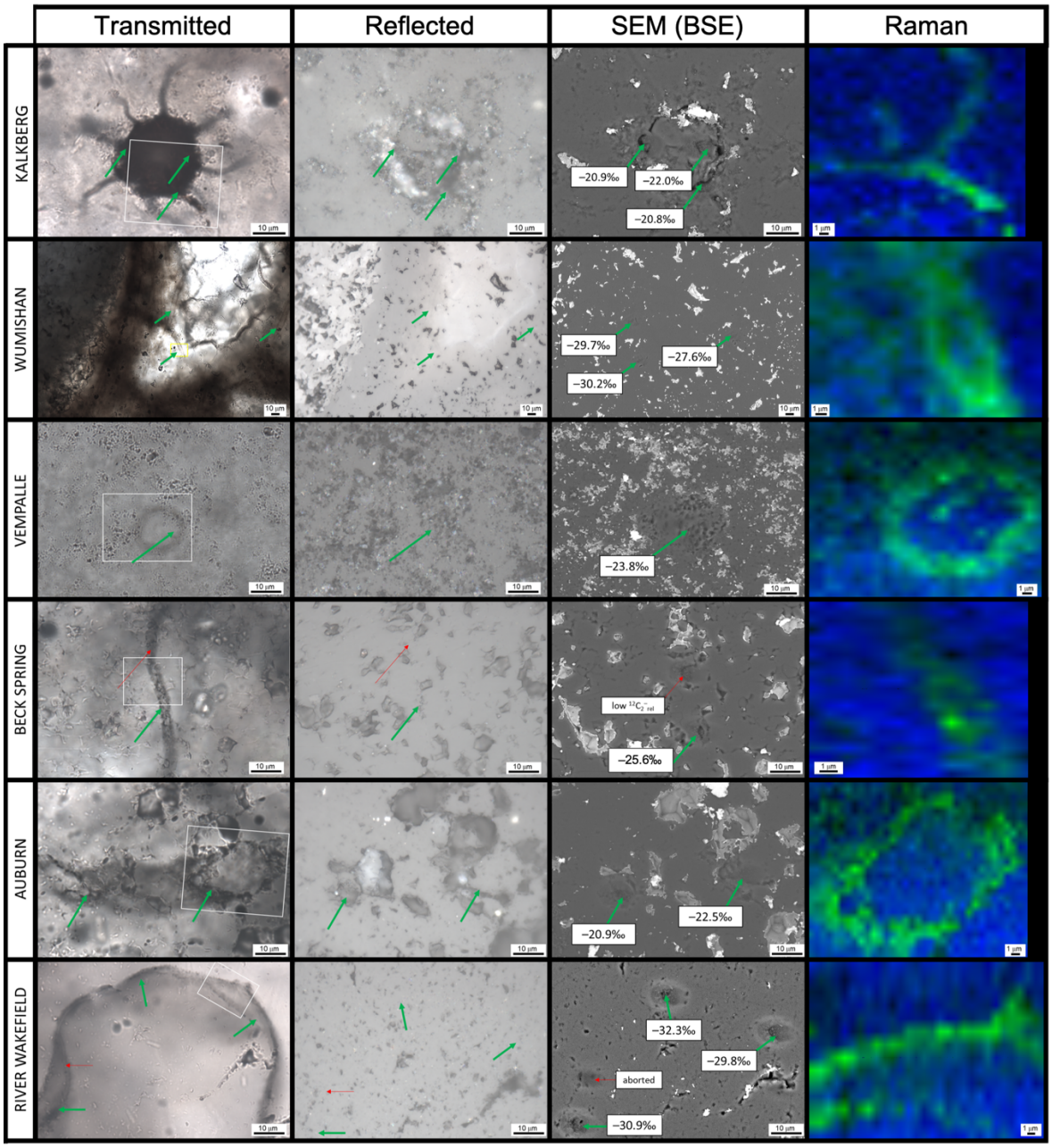

Figure 3-2. Images of analyzed kerogenous microfossils from several of the geologic units studied: the Kalkberg, Wumishan, Vempalle, Beck Spring, Auburn, and River Wakefield. Photomicrographs from optical microscopy using transmitted light, reflected light, and scanning electron microscopy (backscattered electrons; post-SIMS), and 2-D Raman imagery for area shown in corresponding transmitted light image (white box). Light colored areas on SEM images are from remaining gold coat left behind during polishing after SIMS analysis.

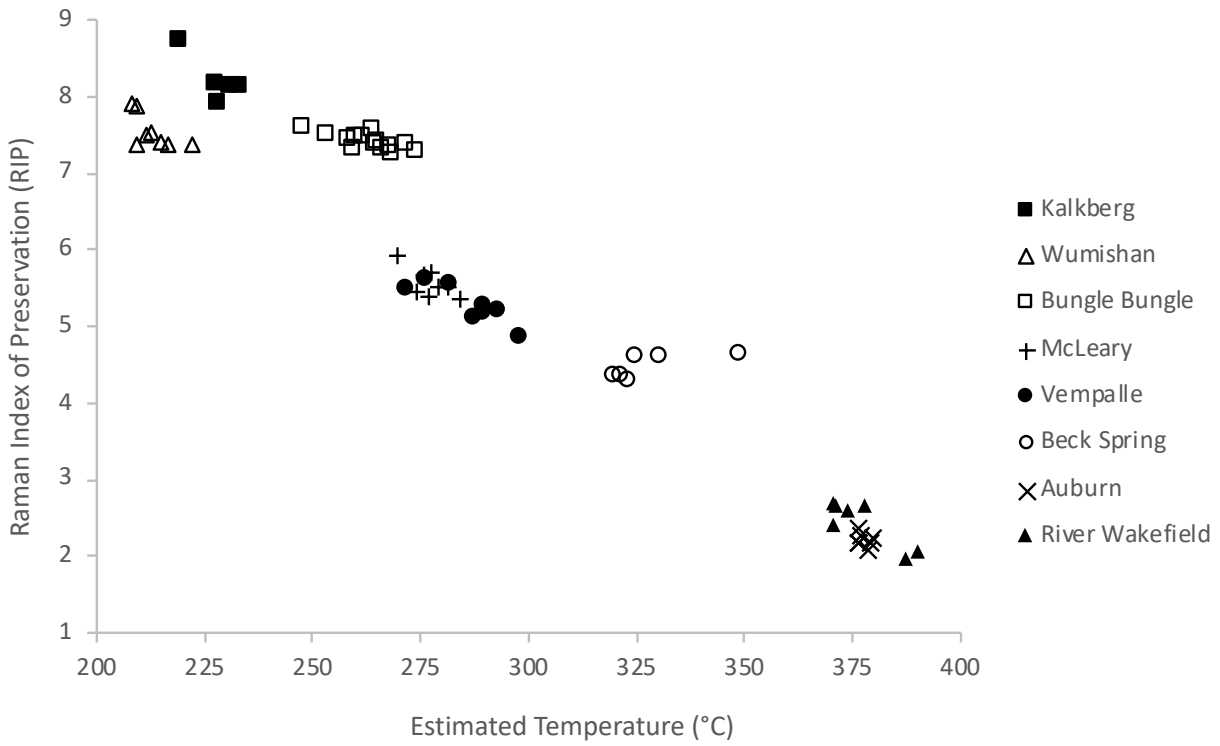

Figure 3-3. Calculations from Raman spectra of kerogen for the eight geologic units studied, comparing Raman Index of Preservation (RIP) values (Schopf et al., 2005) and Raman geothermometry measurements from the same spectra (Kouketsu et al., 2014). $R^2 = 0.916$.

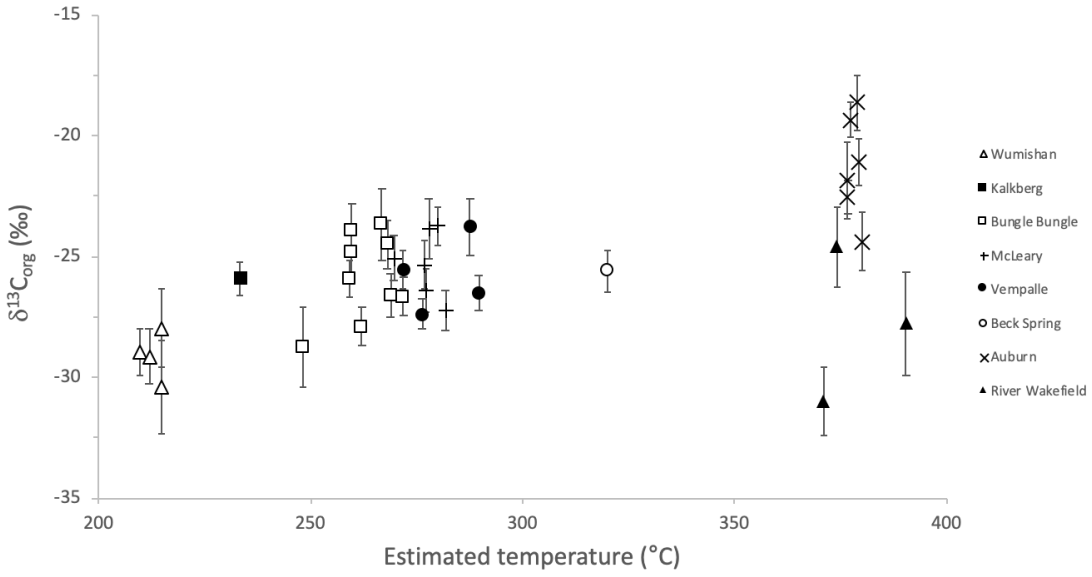

Figure 3-4. SIMS $\delta^{13}C_{org}$ values plotted against estimated peak metamorphic temperature of kerogenous microfossils analyzed from each of the eight geologic units studied. Error bars show calculated final error.

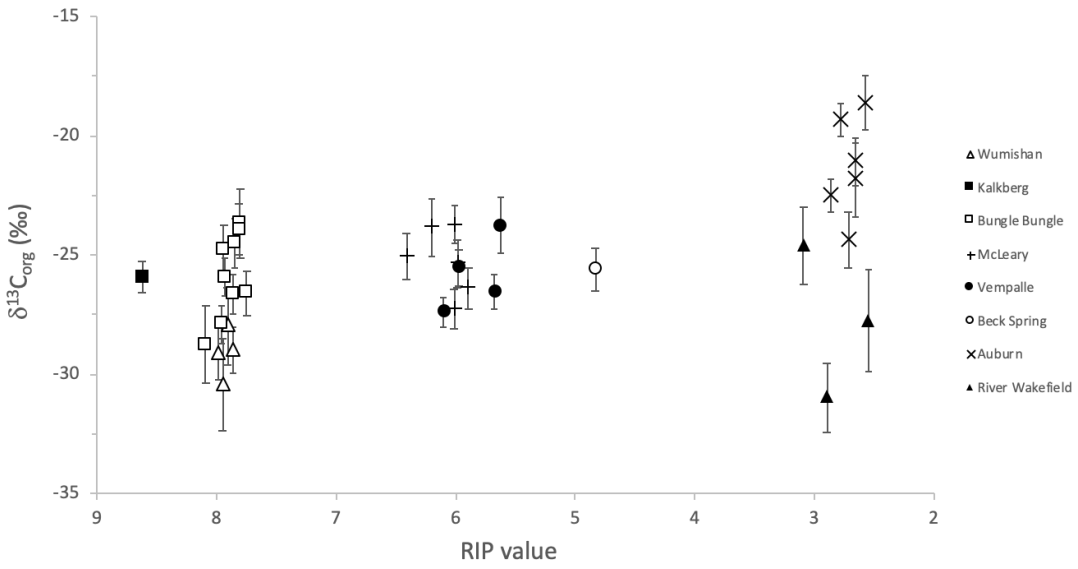

Figure 3-5. SIMS $\delta^{13}C_{org}$ and RIP values of kerogenous microfossils analyzed from each of the eight geologic units studied. Error bars show calculated final error.

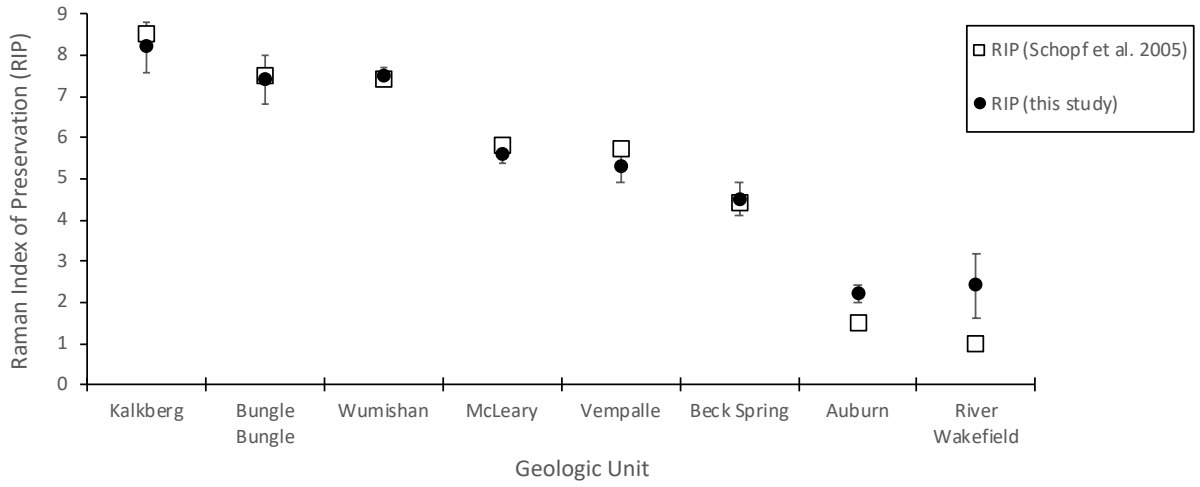

Figure 3-6. Summary of Raman Index of Preservation (RIP) values from eight geologic units studied here (black circles) compared to average RIP values reported from Schopf et al. (2005) (white squares). Error bars for RIP values represents two standard deviations (2SD). See Table 3-1 and text for description of RIP values and bulk geochemical data.

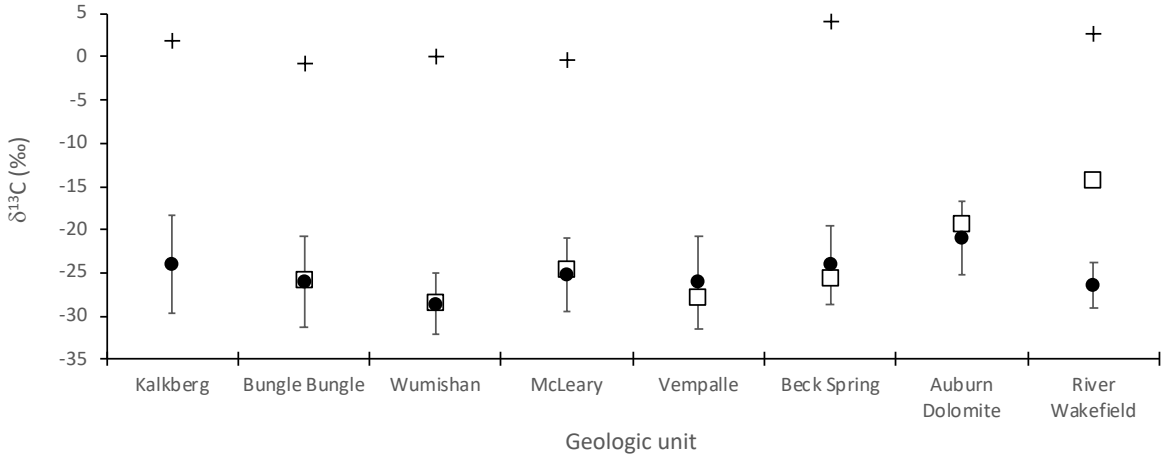

Figure 3-7. Summary of SIMS carbon isotope data from eight geologic units studied here (black circles) compared to average bulk organic carbon isotope data collected from previous studies (white squares). Error bars for SIMS $\delta^{13}C_{org}$ values represents two standard deviations (2SD). Average carbon isotope values for inorganic carbon are also provided for reference (crosses). See Table 3-1 and text for description of average bulk "whole-rock" analyses.

REFERENCES

Allwood, A. C., Walter, M. R., Kamber, B. S., Marshall, C. P., & Burch, I. W. (2006a). Stromatolite reef from the Early Archaean era of Australia. *Nature*, *441*(7094), 714–718.

Allwood, A. C., Walter, M. R., & Marshall, C. P. (2006b). Raman spectroscopy reveals thermal palaeoenvironments of c.3.5 billion-year-old organic matter. *Vibrational Spectroscopy*, *41*, 190–197.

Allwood, A. C., Rosing, M. T., Flannery, D. T., Hurowitz, J. A., & Heirwegh, C. M. (2018). Reassessing evidence of life in 3,700-million-year-old rocks of Greenland. *Nature*, *563*(7730), 241–244.

Aoya, M., Kouketsu, Y., Endo, S., Shimizu, H., Mizukami, T., Nakamura, D., & Wallis, S. (2010). Extending the applicability of the Raman carbonaceous-material geothermometer using data from contact metamorphic rocks. *Journal of Metamorphic Geology*, *28*(9), 895–914.

Barghoorn, E. S., & Schopf, J. W. (1965). Microorganisms from the Late Precambrian of Central Australia. *Science*, *150*, 337–339.

Barghoorn, E. S., & Tyler, S. A. (1965). Microorganisms from the Gunflint chert. *Science*, *197*, 563–576.

Bartley, J. K. (1996). Actualistic taphonomy of cyanobacteria; implications for the Precambrian fossil record. *Palaios*, *11*(6), 571–586.

Bell, E. A., Boehnke, P., Harrison, T. M., & Mao, W. L. (2015). Potentially biogenic carbon preserved in a 4.1 billion-year-old zircon. *Proceedings of the National Academy of Sciences USA*, *112*(47), 14518–14521.

Beyssac, O., Goffé, B., Chopin, C., & Rouzaud, J. N. (2002). Raman spectra of carbonaceous material in metasediments: A new geothermometer. *Journal of Metamorphic Geology*, *20*(9), 859–871.

Bottinga, Y. (1969). Calculated fractionation factors for carbon and hydrogen isotope exchange in the system calcite–carbon dioxide–graphite–methane–hydrogen–water vapor. *Geochimica et Cosmochimica Acta*, *33*, 49–64.

Bucher, K., & Grapes, R. (2011). *Petrogenesis of metamorphic rocks*. Springer Science & Business Media.

Buick, R. (1990). Microfossil recognition in Archean rocks: An appraisal of spheroids and filaments from a 3500 M.Y. old chert-barite unit at North Pole, Western Australia. *Palaios*, *5*(5), 441–459.

Byerly, R., G., Lower, R., D., & Walsh M., M. (1986). Stromatolites from the 3,300-3,500-Myr Swaziland Supergroup, Barberton Mountain Land, South Africa. *Nature*, *319*, 489–491.

Chakrabarti, G., Shome, D., Kumar, S., Armstrong-Altrin, J. S., & Sial, A. N. (2011). Carbon and oxygen isotopic variations in stromatolitic dolomites of Palaeoproterozoic Vempalle Formation, Cuddapah Basin, India. *Carbonates and Evaporites*, *26*(2), 181–191.

Demoulin, C. F., Lara, Y. J., Cornet, L., François, C., Baurain, D., Wilmotte, A., & Javaux, E. J. (2019). Cyanobacteria evolution: Insight from the fossil record. *Free Radical Biology and Medicine, 140,* 206–223.

Des Marais, D. J. (1997). Isotopic evolution of the biogeochemical carbon cycle during the Proterozoic Eon. *Organic Geochemistry*, *27*(5–6), 185–193.

Des Marais, D. J. (2001). Isotopic evolution of the biogeochemical carbon cycle during the Precambrian. *Reviews in Mineralogy and Geochemistry*, *43*, 555–578.

Diver, W. L. (1974). Precambrian microfossils of Carpentarian age from Bungle Bungle Dolomite of Western Australia. *Nature*, *247*(5440), 361–363.

Emrich, K., Ehhalt, D. H., & Vogel, J. C. (1970). Carbon isotope fractionation during precipitation of calcium carbonate. *Earth and Planetary Science Letters*, *8*, 363–371.

Flannery, D. T., Allwood, A. C., Summons, R. E., Williford, K. H., Abbey, W., Matys, E. D., & Ferralis, N. (2018). Spatially-resolved isotopic study of carbon trapped in ~3.43 Ga Strelley Pool Formation stromatolites. *Geochimica et Cosmochimica Acta*, *223*, 21–35.

Foucher, F., Ammar, M. R., & Westall, F. (2015). Revealing the biotic origin of silicified Precambrian carbonaceous microstructures using Raman spectroscopic mapping, a potential method for the detection of microfossils on Mars. *Journal of Raman Spectroscopy*, *46*(10), 873–879.

Freeman, K. H., & Hayes, J. M. (1992). Fractionation of carbon isotopes by phytoplankton and estimates of ancient CO_2 levels. *Global Biogeochemical Cycles*, *6*, 185–198.

Garrels, R. M., & McKenzie, F. T. (1971). *Evolution of Sedimentary Rocks*. W.W. Norton & Co.

Guo, H., Du, Y., Kah, L. C., Huang, J., Hu, C., Huang, H., & Yu, W. (2013). Isotopic composition of organic and inorganic carbon from the Mesoproterozoic Jixian Group, North China: Implications for biological and oceanic evolution. *Precambrian Research*, *224*, 169–183.

Hayes, J. M. (1993). Factors controlling ^{13}C contents of sedimentary organic compounds: Principles and evidence. *Marine Geology*, *113*(1–2), 111–125.

Hayes, J. M. (1994). Global methanotrophy at the Archean-Proterozoic transition. In S. Bengtson (Ed.), *Early Life on Earth, Nobel Symposium No. 84* (pp. 220-236). Columbia University Press.

Hayes, J. M., Kaplan, I. R., & Wedeking, K. W. (1983). Precambrian organic geochemistry: Preservation of the record. In J. W. Schopf (Ed.), *Earth's Earliest Biosphere: Its Origin and Evolution* (pp. 93-134). Princeton University Press.

Hayes, J. M., Strauss, H., & Kaufman, A. J. (1999). The abundance of ^{13}C in marine organic matter and isotopic fractionation in the global biogeochemical cycle of carbon during the past 800 Ma. *Chemical Geology*, *161*, 103–125.

Henry, D. G., Jarvis, I., Gillmore, G., & Stephenson, M. (2019). Raman spectroscopy as a tool to determine the thermal maturity of organic matter: Application to sedimentary, metamorphic and structural geology. *Earth-Science Reviews*, *198*(August), 102936.

Hess, A. V., & Trop, J. M. (2019). Sedimentology and carbon isotope ($\delta^{13}C$) stratigraphy of Silurian–Devonian boundary interval strata, Appalachian Basin (Pennsylvania, USA). *Palaios*, *34*(9), 405–423.

Hofmann, H. J. (1976). Precambrian microflora, Belcher Islands, Canada: significance and systematics. *Journal of Paleontology*, *50*, 1040–1073.

Hofmann, H. J., & Schopf, J. W. (1983). Early Proterozoic microfossils. In J. W. Schopf (Ed.), *Earth's Earliest Biosphere, Its Origin and Evolution* (pp. 321-360). Princeton University Press.

House, C. H. (2015). A synthetic standard for the analysis of carbon isotopes of carbon in silicates, and the observation of a significant water-associated matrix effect. *Geochemical Transactions*, *16*(14), 1–8.

House, C. H., Schopf, J. W., McKeegan, K. D., Coath, C. D., Harrison, T. M., & Stetter, K. O. (2000). Carbon isotopic composition of individual Precambrian microfossils. *Geology*, *8*, 707–710.

House, C. H., Oehler, D. Z., Sugitani K., & Mimura, K. (2013). Carbon isotopic analyses of ca. 3.0 Ga microstructures imply planktonic autotrophs inhabited Earth's early oceans. *Geology*, *41*, 651–654.

Husson, J. M., Schoene, B., Bluher, S., & Maloof, A. C. (2016). Chemostratigraphic and U–Pb geochronologic constraints on carbon cycling across the Silurian–Devonian boundary. *Earth and Planetary Science Letters*, *436*, 108–120.

Ishida, A., Kitajima, K., Williford, K. H., Tuite, M. L., Kakegawa, T., & Valley, J. W. (2018). Simultaneous in situ analysis of carbon and nitrogen isotope ratios in organic matter by secondary ion mass spectrometry. *Geostandards and Geoanalytical Research*, *42*(2), 189–203.

Jardine, T. D., & Cunjak, R. A. (2005). Analytical error in stable isotope ecology. *Oecologia, 144*, 528–533.

Javaux, E. J. (2019). Challenges in evidencing the earliest traces of life. *Nature*, *572*(7770), 451–460.

Kazmierczak, J., & Kremer, B. (2002). Thermal alteration of the Earth's oldest fossils. *Nature*, *420*(6915), 477-478.

Khelen, A. C., Manikyamba, C., Ganguly, S., Singh, T. D., Subramanyam, K. S. V., Ahmad, S. M., & Reddy, M. R. (2017). Geochemical and stable isotope signatures of Proterozoic stromatolitic carbonates from the Vempalle and Tadpatri Formations, Cuddapah Supergroup, India: Implications on paleoenvironment and depositional conditions. *Precambrian Research*, *298*, 365–384.

Kitchen, N. E., & Valley, J. W. (1995). Carbon isotope thermometry in marbles of the Adirondack Mountains, New York. *Journal of Metamorphic Geology*, *13*, 577–594.

Klein, C., & Hurlbut, C. S. Jr. (1985). *Manual of Mineralogy* (20th ed.). Wiley.

Knoll, A. H., Bergmann, K. D., & Strauss, J. V. (2016). Life: the first two billion years. *Philosophical Transactions of the Royal Society B: Biological Sciences*, *371*(1707), 20150493.

Kouketsu, Y., Mizukami, T., Mori, H., Endo, S., Aoya, M., Hara, H., Nakamura, D., & Wallis, S. (2014). A new approach to develop the Raman carbonaceous material geothermometer for low-grade metamorphism using peak width. *Island Arc*, *23*, 33–50.

Kremer, B., Kazmierczak, J., Łukomska-Kowalczyk, M., & Kempe, S. (2012). Calcification and silicification: Fossilization potential of cyanobacteria from stromatolites of Niuafo'ou's caldera lakes (Tonga) and implications for the early fossil record. *Astrobiology*, *12*(6), 535–548.

Kuang, H., Liu, Y., Li, J., Peng, N., Luo, S., & Cen, C. (2011). Carbon and oxygen isotopic stratigraphy of Mesoproterozoic carbonate sequences (1.6–1.4 Ga) from Yanshan in North China. *International Journal of Oceanography*, *2011*, 1–11.

Kuang, H. W., Liu, Y. Q., Peng, N., Lug, S. S., Li, J. H., Cen, C., Chen, M. P. (2012). Molar-tooth structure from the Mesoproterozoic Wumishan Formation in Lingyuan, Yanshan Region, North China, and geological implications. *Acta Geologica Sinica-English Edition*, *86*, 85–95.

Kudryavtsev, A. B., Schopf, J. W., Agresti, D. G., & Wdowiak, T. J. (2001). In situ laser-Raman imagery of Precambrian microscopic fossils. *Proceedings of the National Academy of Sciences USA*, *98*(3), 823–826.

Lee, C., Love, G. D., Jahnke, L. L., Kubo, M. D., & Des Marais, D. J. (2019). Early diagenetic sequestration of microbial mat lipid biomarkers through covalent binding into insoluble

macromolecular organic matter (IMOM) as revealed by sequential chemolysis and catalytic hydropyrolysis. *Organic Geochemistry*, *132*, 11–22.

Lepot, K., Williford, K. H., Ushikubo, T., Sugitani, K., Mimura, K., Spicuzza, M. J., & Valley, J. W. (2013). Texture-specific isotopic compositions in 3.4 Gyr old organic matter support selective preservation in cell-like structures. *Geochimica et Cosmochimica Acta*, *112*, 66–86.

Loeblich Jr., A. R. (1970). Morphology, ultrastructure and distribution of Paleozoic acritarchs. *Proceedings of the North American Paleontological Convention, G*, 705–788.

Licari, G. R. (1978). Biogeology of the late pre-Phanerozoic Beck Spring Dolomite of eastern California. *Journal of Paleontology, 52,* 767–792.

Maliva, R. G., Knoll, A. H., & Simonson, B. M. (2005). Secular change in the Precambrian silica cycle: Insights from chert petrology. *Bulletin of the Geological Society of America*, *117*(7–8), 835–845.

Manning-Berg, A., Wood, R., Williford, K., Czaja, A., & Kah, L. (2019). The taphonomy of Proterozoic microbial mats and implications for early diagenetic silicification. *Geosciences*, *9*(1), 40.

Marshall, C. P., Love, G. D., Snape, C. E., Hill, A. C., Allwood, A. C., Walter, M. R., Van Kranendonk, M. J., Bowden, S. A., Sylva, S. P., & Summons, R. E. (2007). Structural

characterization of kerogen in 3.4 Ga Archaean cherts from the Pilbara Craton, Western Australia. *Precambrian Research*, *155*(1–2), 1–23.

McCollom, T. M. (2011). What can carbon isotopes tell us about sources of reduced carbon in rocks from the early Earth?. In S. D. Golding & M. Glikson (Eds.), *Earliest life on Earth: Habitats, environments and methods of detection* (pp. 291-311). Springer.

McKirdy, D. M., & Hahn, J. H. (1982). The composition of kerogen and hydrocarbons in Precambrian rocks. In H. D. Holland & M. Schidlowski (Eds.), *Mineral Deposits and the Evolution of the Biosphere* (pp. 123–154). Springer.

Mojzsis, S. J., Arrhenius, G., McKeegan, K. D., Harrison, T. M., Nutman, A. P., & Friend, C. R. L. (1996). Evidence for life on Earth before 3,800 million years ago. *Nature*, *384*(6604), 55–59.

Morag, N., Williford, K. H., Kitajima, K., Philippot, P., Van Kranendonk, M. J., Lepot, K., Thomazo, C., & Valley, J. W. (2016). Microstructure-specific carbon isotopic signatures of organic matter from ~3.5 Ga cherts of the Pilbara Craton support a biologic origin. *Precambrian Research*, *275*, 429–449.

Oehler, D., & Cady, S. (2014). Biogenicity and syngeneity of organic matter in ancient sedimentary rocks: Recent advances in the search for evidence of past life. *Challenges*, *5*(2), 260–283.

Oehler, D. Z., Schopf, J. W., & Kvenvolden, K. A. (1972). Carbon isotopic studies of organic matter in Precambrian rocks. *Science, 175*(4027), 1246–1248.

Oehler, D. Z., Walsh, M. M., Sugitani, K., Liu, M. C., & House, C. H. (2017). Large and robust lenticular microorganisms on the young Earth. *Precambrian Research*, *296*, 112–119.

Orphan, V. J., & House, C. H. (2009). Geobiological investigations using secondary ion mass spectrometry: Microanalysis of extant and paleo-microbial processes. *Geobiology*, *7*, 360–372.

Osterhout, J. T., Czaja, A. D., Bartley, J. K., & Fralick, P. W. (2019). Preservation of carbon isotopes in kerogen from thermally altered Mesoproterozoic lacustrine microbialites. *Canadian Journal of Earth Sciences*, *56*(10), 1017–1026.

Ohtomo, Y., Kakegawa, T., Ishida, A., Nagase, T., & Rosing, M. T. (2014). Evidence for biogenic graphite in early Archaean Isua metasedimentary rocks. *Nature Geoscience*, *7*, 25–28.

Pasteris, J. D., & Wopenka, B. (1991). Raman spectra of graphite as indicators of degree of metamorphism. *The Canadian Mineralogist*, *29*(1), 1–9.

Peng, X., Guo, Z., House, C. H., Chen, S., & Ta, K. (2016). SIMS and NanoSIMS analyses of well-preserved microfossils imply oxygen-producing photosynthesis in the Mesoproterozoic anoxic ocean. *Chemical Geology*, *441*, 24–34.

Perry, E. C., & Lefticariu, L. (2014). Formation and geochemistry of Precambrian cherts. In H. D. Holland & K. K. Turekian (Eds.), *Treatise on Geochemistry* (2nd ed., Vol. 9). Elsevier.

Petrash, D. A., Robbins, L. J., Shapiro, R. S., Mojzsis, S. J., & Konhauser, K. O. (2016). Chemical and textural overprinting of ancient stromatolites: Timing, processes, and implications for their use as paleoenvironmental proxies. *Precambrian Research*, *278*, 145–160.

Popp, B. N., Laws, E. A., Bidigare, R. R., Dore, J. E., Hanson, K. L., & Wakeham, S. G. (1998). Effect of phytoplankton cell geometry on carbon isotopic fractionation. *Geochimica et Cosmochimica Acta*, *62*(1), 69–77.

Preiss, W. V. (2000). The Adelaide Geosyncline of South Australia and its significance in Neoproterozoic continental reconstruction. *Precambrian Research*, *100*(1-3), 21–63.

Preiss, W. V., & Cowley, W. M. (1999). Genetic stratigraphy and revised lithostratigraphic classification of the Burra Group in the Adelaide Geosyncline. *MESA Journal*, *14*, 30–40.

Rollinson, H. (2003). Metamorphic history suggested by garnet-growth chronologies in the Isua Greenstone Belt, West Greenland. *Precambrian Research*, *126*(3-4), 181–196.

Schidlowski, M., Appel, P. W. U., Eichmann, R., & Junge, C. E. (1979). Carbon isotope geochemistry of the 3.7×10^9 yr. old Isua sediments, West Greenland: Implications for the Archaean carbon and oxygen cycles. *Geochimica et Cosmochimica Acta*, *43*, 189–199.

Schidlowski, M., Hayes, J. M., & Kaplan, I. R. (1983). Isotopic inferences of ancient biochemistries: Carbon, sulfur, hydrogen and nitrogen. In J. W. Schopf (Ed.), *Earth's Earliest Biosphere: Its Origin and Evolution* (pp. 149–186). Princeton University Press.

Schidlowski, M. (2001). Carbon isotopes as biogeochemical recorders of life over 3.8 Ga of Earth history: evolution of a concept. *Precambrian Research*, *106*(1-2), 117–134.

Schopf, J. W. (1975). Precambrian paleobiology: Problems and perspectives. *Annual Review of Earth and Planetary Sciences*, 3, 213–249.

Schopf, J. W. (1992). Atlas of representative Proterozoic microfossils. In J. W. Schopf & C. Klein (Eds.), *The Proterozoic Biosphere: A Multidisciplinary Study* (pp. 1055–1117). Cambridge University Press.

Schopf, J. W., & Prasad, K. N. (1978). Microfossils in Collenia-like stromatolites from the Proterozoic Vempalle Formation of the Cuddapah basin, India. *Precambrian Research*, 6(3-4), 347–366.

Schopf, J. W., & Kudryavtsev, A. B. (2009). Confocal laser scanning microscopy and Raman imagery of ancient microscopic fossils. *Precambrian Research*, *173*(1–4), 39–49.

Schopf, J. W., Kudryavtsev, A. B., Agresti, D. G., Czaja, A. D., & Wdowiak, T. J. (2005). Raman imagery: a new approach to assess the geochemical maturity and biogenicity of permineralized Precambrian fossils. *Astrobiology*, *5*(3), 333–371.

Schopf, J. W., Kudryavtsev, A. B., Czaja, A. D., & Tripathi, A. B. (2007). Evidence of Archean life: stromatolites and microfossils. *Precambrian Research*, *158*(3-4), 141–155.

Schopf, J. W., Kitajima, K., Spicuzza, M. J., Kudryavtsev, A. B., & Valley, J. W. (2018). SIMS analyses of the oldest known assemblage of microfossils document their taxon-correlated carbon isotope compositions. *Proceedings of the National Academy of Sciences USA*, *115*(1), 53–58.

Simonet, B. R. T., Brenner, S., Peters, K. E., & Kaplan, I. R. (1981). Thermal alteration of Cretaceous black shale by diabase intrusions in the Eastern Atlantic-II. Effects on bitumen and kerogen. *Geochimica et Cosmochimica Acta*, *45*(9), 1581–1602.

Strauss, H., & Moore, T. B. (1992). Abundances and isotopic compositions of carbon and sulfur Species in Whole Rock and Kerogen Sample*s*. In J. W. Schopf & C. Klein (Eds.), *The Proterozoic Biosphere: A Multidisciplinary Study* (pp. 709-798). Cambridge University Press.

Strauss, H., Des Marais, D. J., Hayes, J. M., & Summons, R. E. (1992a). Proterozoic organic carbon—its preservation and isotopic record. In M. Schidlowski, S. Golubic, M. Kimberly, D. McKirdy, & P. A. Trudinger (Eds.), *Early Organic Evolution* (pp. 203-211). Springer.

Strauss H., Des Marais D. J., Hayes J. M. and Summons R. E. (1992b). The carbon-isotopic record. In J. W. Schopf & C. Klein (Eds.), *The Proterozoic Biosphere: A Multidisciplinary Study* (pp. 117-127). Cambridge University Press.

Sugitani, K., Lepot, K., Nagaoka, T., Mimura, K., Van Kranendonk, M., Oehler, D. Z., & Walter, M. R. (2010). Biogenicity of morphologically diverse carbonaceous microstructures from the ca. 3400 Ma Strelley Pool Formation, in the Pilbara Craton, Western Australia. *Astrobiology*, *10*(9), 899–920.

Summons, R. E., & Hayes, J. M. (1992). Principles of molecular and isotopic biogeochemistry. In J. W. Schopf & C. Klein (Eds.), *The Proterozoic Biosphere: A Multidisciplinary Study* (pp. 83-93). Cambridge University Press.

Tashiro, T., Ishida, A., Hori, M., Igisu, M., Koike, M., Méjean, P., Takahata, N., Sano, Y., & Komiya, T. (2017). Early trace of life from 3.95 Ga sedimentary rocks in Labrador, Canada. *Nature*, *549*(7673), 516–518.

Ueno, Y., Isozaki, Y., Yurimoto, H., & Maruyama, S. (2001). Carbon isotopic signatures of individual Archean microfossils(?) from Western Australia. *International Geology Review*, *43*(3), 196–212.

Ueno, Y., Yurimoto, H., Yoshioka, H., Komiya, T., & Maruyama, S. (2002). Ion microprobe analysis of graphite from ca. 3.8 Ga metasediments, Isua supracrustal belt, West Greenland: Relationship between metamorphism and carbon isotopic composition. *Geochimica et Cosmochimica Acta*, *66*(7), 1257–1268.

Valley, J. W., & O'Neil, J. R. (1981). $^{13}C/^{12}C$ exchange between calcite and graphite: A possible thermometer in Grenville marbles. *Geochimica et Cosmochimica Acta*, *45*, 411–419.

Van Zuilen, M. A., Lepland, A., & Arrhenius, G. (2002). Reassessing the evidence for the earliest traces of life. *Nature, 418*, 627–630.

Wacey, D., Menon, S., Green, L., Gerstmann, D., Kong, C., Mcloughlin, N., Saunders, M., & Brasier, M. (2012). Taphonomy of very ancient microfossils from the ~3400 Ma Strelley Pool Formation and ~1900 Ma Gunflint Formation: New insights using a focused ion beam. *Precambrian Research*, *220–221*, 234–250.

Wada, H., & Suzuki, K. (1983). Carbon isotopic thermometry calibrated by dolomite-calcite solvus temperatures. *Geochimica et Cosmochimica Acta*, *47*, 697–706.

Walsh, M. W. (1992). Microfossils and possible microfossils from the Early Archean Onverwacht Group, Barberton Mountain Land, South Africa. *Precambrian Research*, *54*(2–4), 271–293.

Walter, M. R., Hofmann, H. J., & Schopf, J. W. (1983). Geographic and geologic data for processed rock samples. In J. W. Schopf (Ed.), *Earth's Earliest Biosphere: Its Origin and Evolution* (p. 392). Princeton University Press.

Watanabe, Y., Naraoka, H., Wronkiewicz, D. J., Condie, K. C., & Ohmoto, H. (1997). Carbon, nitrogen, and sulfur geochemistry of Archean and Proterozoic shales from the Kaapvaal Craton, South Africa. *Geochimica et Cosmochimica Acta*, *61*(16), 3441–3459.

Westall, F. (2004). Early life on Earth: The ancient fossil record. In P. Ehrenfreund, W. Irvine, T. Owen, L. Becker, J. Blank, J. Brucato, L. Colangeli, S. Derenne, A. Dutrey, D. Despois, A. Lazcano, & F. Robert (Eds.), *Astrobiology: Future Perspectives* (pp. 287-316). Springer.

Westall, F., De Wit, M. J., Dann, J., Van der Gaast, S., De Ronde, C. E. J., & Gerneke, D. (2001). Early Archean fossil bacteria and biofilms in hydrothermally-influenced sediments from the Barberton greenstone belt, South Africa. *Precambrian Research*, *106*(1–2), 93–116.

Wicander, E. R., & Schopf, J. W. (1974). Microorganisms from the Kalkberg Limestone (Lower Devonian) of New York State. *Journal of Paleontology*, *48*, 74–77.

Williford, K. H., Ushikubo, T., Schopf, J. W., Lepot, K., Kitajima, K., & Valley, J. W. (2013). Preservation and detection of microstructural and taxonomic correlations in the carbon isotopic compositions of individual Precambrian microfossils. *Geochimica et Cosmochimica Acta*, *104*, 165–182.

Williford, K. H., Ushikubo, T., Lepot, K., Kitajima, K., Hallmann, C., Spicuzza, M. J., Kozdon, R., Eigenbrode, J. L., Summons, R. E., & Valley, J. W. (2016). Carbon and sulfur isotopic signatures of ancient life and environment at the microbial scale: Neoarchean shales and carbonates. *Geobiology*, *14*, 105–128.

Zhang, Y. (1985). Stromatolitic microbiota from the middle Proterozoic Wumishan Formation (Jixian Group) of the Ming Tombs, Beijing, China. *Precambrian Research*, *30*(3), 277–302.

Chapter 4

Deep-UV Raman spectroscopy of carbonaceous Precambrian microfossils: Insights into the search for past life on Mars

Jeffrey T. Osterhout, J. William Schopf, Anatoliy B. Kudryavtsev, Andrew D. Czaja, Kenneth H. Williford

1. INTRODUCTION

For more than 50 years the search for evidence of ancient microbial life on Mars has been the subject of serious astrobiological interest and planetary exploration, culminating in modern surface exploration missions by landers and rovers and the foundations of which are embedded in the pioneering studies of Precambrian life on the early Earth (Farmer and Des Marais, 1999). The fossil record of primitive microorganisms during the first ~4 billion years (Ga) of Earth history consists mainly of stromatolites and other microbially-influenced sedimentary structures, which occasionally preserve carbonaceous microfossils or other geochemical traces of life (Schopf, 2006; Knoll, 2012; Oehler and Cady, 2014). Precambrian microfossils are typically preserved as organic-walled microstructures permineralized in chemically precipitated sedimentary rocks which have undergone early diagenetic silicification. Virtually all such fossils exhibit relatively simple prokaryotic morphologies, typically including multicellular filamentous trichomes and their vacated tubular sheaths, and unicellular coccoids and ellipsoids and their commonly sheath-encompassed colonial aggregates (Westall, 1999; Schopf, 2006; Sergeev, 2009). In addition, and more commonly preserved in coeval shales rather than silicified stromatolites, larger, more

complex, primarily eukaryotic forms occur dating back to at least ~1.8 Ga (Zhang, 1997; Knoll et al., 2006; Javaux, 2007; Lamb et al., 2009; Knoll, 2014; Butterfield, 2015).

The carbonaceous matter of which most Precambrian microfossils are composed is amorphous macromolecular kerogen, preserved in rocks of varying thermal maturities, ranging from unmetamorphosed (<150 °C) to greenschist facies (~200–400 °C). With increasing burial temperatures (and pressures) morphological biosignatures can be altered, degraded, and eventually destroyed. During this process the molecular structure of kerogen changes as its component organic compounds are transformed over time from the biomolecules present in living systems to amorphous kerogen with its characteristic polycyclic aromatic hydrocarbon (PAH) composition. With increasing geochemical alteration, the graphene layers thus produced become increasingly more regularly ordered, the process ultimately resulting in the formation of crystalline graphite in highly metamorphosed deposits (e.g., Durand, 1980; Wopenka and Pasteris, 1993; Beyssac et al., 2002; Schopf et al., 2005).

Because the spectroscopic properties of such organic matter have also been shown to change during this metamorphic sequence, Raman spectroscopy and imagery have been routinely performed on Precambrian microfossils to document their organic composition and degree of thermal maturity, and to thereby assess their biogenicity (e.g., Kudryavtsev et al., 2001; Schopf et al., 2002, 2005, 2017; Allwood et al., 2006; Marshall et al., 2007; Sugitani et al., 2007). Nevertheless, and despite the value of such analyses, it is worth noting that Raman spectroscopy by itself is incapable of establishing the biological origin of fossilized organic matter or putative microfossils in the absence of supporting morphological and geochemical (e.g., isotopic) data (Pasteris and Wopenka, 2003; Schopf et al., 2005; Bower et al., 2013; Flannery et al., 2018). On Earth, kerogen comprises the largest pool of organic matter preserved in the sedimentary rock

record and most of the reduced organic carbon within Precambrian rocks is therefore attributed to a primary biological origin (Durand, 1980; Schidlowski, 2001; Vandenbroucke and Largeau, 2007). Sedimentary rocks containing kerogen and other more mobile organic compounds are thus regarded as primary astrobiological targets in the search for evidence of past life on Mars (Farmer and Des Marais, 1999; Marshall et al., 2010; Foucher et al., 2015; Shkolyar et al., 2018; McMahon et al., 2018).

Neither stromatolites nor microfossils have yet been detected by in situ analyses of Mars rocks, although potentially habitable environments and minerals relevant to microbial preservation have been directly identified from orbit (e.g., Mustard et al., 2008; Wray et al., 2008; Ehlmann et al., 2008; Ehlmann and Edwards, 2014; Bishop, 2018; Tarnas et al., 2019) and interpreted from studies of sedimentary rocks at the Martian surface (e.g., Arvidson et al., 2008; Stoker et al., 2010; Grotzinger and Milliken, 2012; Grotzinger et al., 2014). Moreover, such in situ studies have also yielded evidence of refractory organic carbon in lacustrine mudstones that resembles macromolecular kerogen formed by ancient life on Earth (Eigenbrode et al., 2018). Such findings have further motivated the astrobiological exploration of early Mars and have helped guide the Mars 2020 mission to explore Jezero Crater, due in part to the relatively high preservation-potential for organic matter within its paleolake sediments (Ehlmann et al., 2008; Goudge et al., 2017; Grant et al., 2018; Mangold et al., 2020). The Mars 2020 rover mission continues to build on these earlier developments, and samples containing high amounts of carbonaceous matter will be considered prime astrobiological targets for in situ analyses and subsequent sample caching as part of the planned Mars Sample Return mission (Mustard et al., 2013; Williford et al., 2018).

Given the ongoing Mars 2020 mission – including the detailed analyses of the rock samples then cached and brought to Earth for study – it is imperative to characterize the molecular

signatures of kerogenous Precambrian microfossils from sedimentary rocks of varying thermal maturities on Earth using analytical capabilities similar to those to be employed by these endeavors. On Earth, organic compounds produced by microorganisms may become buried and preserved in sedimentary rocks and subsequently altered during diagenesis to form complex networks of degraded biomolecules and amorphous carbonaceous matter resulting in the production of mainly interlinked PAHs. Among the various techniques available for such analyses, Raman spectroscopy is widely considered essential, a tool capable of detecting signs of past life by its unambiguous identification of kerogenous carbonaceous matter, though requiring additional forms of evidence (e.g., morphological, molecular, isotopic) to fully evaluate potential biogenicity (Ellery and Wynn-Williams, 2003; Pasteris and Wopenka, 2003; Marshall et al., 2010; Foucher et al., 2015). Thus, a Raman spectrometer has been included as one of the key astrobiological instruments on the payload of the Mars 2020 rover, *Perseverance*.

The carbonaceous composition of rock-embedded organic matter can be readily determined by the characteristic kerogen peaks in its Raman spectrum (e.g., Kudryavtsev et al., 2001; Schopf et al., 2002, 2005; Marshall et al., 2010). In addition to providing diagnostic molecular information, Raman spectroscopy is also useful for measuring the thermal maturity of ancient organic matter (e.g., Beyssac et al., 2002; Pasteris and Wopenka, 2003; Schopf et al., 2005). As sediments undergo diagenesis and lithification, organic biomolecules (e.g., lipids, carbohydrates, proteins, DNA, etc.), if preserved, experience transformation processes resulting in polymerization and formation of thermally immature macromolecular kerogen (Durand, 1980). As a result, further geochemical maturation of kerogen produces a set of stable compounds containing numerous interlinked PAHs, which become increasingly carbon-rich and graphitized under high pressure and temperature conditions as the kerogen becomes more regularly ordered. These

changes in the geochemical structure of organic matter can be readily detected and differentiated using Raman spectroscopy (e.g., Beyssac et al., 2002; Schopf et al., 2005; Kouketsu et al., 2014).

Microfossils with unequivocal cellular morphologies shown to be composed of such organic carbon therefore represent direct, primary evidence of microbial life in ancient sedimentary rocks, which makes such features among the most sought biosignatures in samples of Mars rocks (e.g., Walter and Des Marais, 1993; Summons et al., 2011; Schopf et al., 2012; Mustard et al., 2013; Westall et al., 2015; Hays et al., 2017). Based on analyses of Raman spectra for kerogenous microfossils from 22 Precambrian units, Schopf et al. (2005) developed a numerical metric for quantifying the relative degree of thermal alteration, known as the Raman Index of Preservation (RIP), which includes geologic units ranging in metamorphic grade from unmetamorphosed to greenschist facies. The RIP value allows for comparisons of relative geothermal maturity for kerogen from different rocks and fossils. The study here presented repeats the Raman measurements of these and other kerogenous microfossils (and associated organic detritus), but in contrast uses deep-UV laser excitation wavelengths (λ_{ex}), the technique employed by the current Mars 2020 mission to search for promising samples by which to establish the existence of past life on Mars.

To date, the search for evidence of ancient microbial life on Mars has focused primarily on the exploration of exposed sedimentary rocks, the identification of potentially habitable environments, and the possible detection of preserved organic carbon (Farmer and Des Marais, 1999; Des Marais, 2010; Summons et al., 2011; Hays et al., 2017; McMahon et al., 2018). One of the primary science goals of the current Mars 2020 mission is to explore the ancient sedimentary rocks of Jezero Crater in an effort to determine whether life ever arose on Mars (Mustard et al., 2013; Williford et al., 2018). To resolve this quandary, the search for evidence of preserved

microbial life will be conducted in situ on the surface of Mars using sensitive analytical equipment onboard the rover, such as the Scanning Habitable Environments with Raman and Luminescence for Organics and Chemicals (SHERLOC) instrument, which includes a specialized deep-UV Raman spectrometer capable of detecting and characterizing various classes of naturally occurring organic compounds (Abbey et al., 2017), including kerogen (Shkolyar et al., 2018).

Additionally, a limited number of samples will be cached on the surface to be collected and brought back to Earth for further analysis as part of the planned Mars Sample Return mission (Williford et al., 2018). The current strategy for exploring and identifying the presence of fossilized microorganisms (and biogenic textures) in ancient Martian sedimentary rocks is based almost entirely on knowledge of Precambrian life and microbial evolution on Earth, and of its preservation in the early rock record. However, in contrast to most Raman studies of Precambrian microfossils on Earth, which typically utilize laser excitation wavelengths in the visible region (~380–700 nm) (e.g., Kudryavtsev et al., 2001; Schopf and Kudryavtsev, 2005; Schopf et al., 2002, 2005; Guo et al., 2018), the Raman spectrometer of the SHERLOC instrument will feature a deep-UV (248.6 nm) laser excitation wavelength to map and characterize various minerals, organic molecules, and potential biosignatures detected in Martian rocks and regolith (Beegle et al., 2015; Abbey et al., 2017). Thus, the findings from previous Raman studies of Precambrian microfossils and kerogen, which have used visible laser wavelengths, are therefore not directly applicable to the spectra which might be encountered by Mars 2020, as the relative intensity and peak center positions change with the laser excitation wavelength as a result of the Raman resonance effect (Wang et al., 1990; Matthews et al., 1999; Sato et al., 2006).

Moreover, deep-UV Raman analyses provide data and insight not available from use of standard visible Raman spectroscopy. Use of such deep laser wavelengths can create resonance effects within certain groups of organic compounds (Marshall et al., 2010; Abbey et al., 2017) and

kerogens (Czaja et al., 2009; Shkolyar et al., 2018) that provide several unique advantages such as identification of compounds relevant to biological systems including nucleic acids, proteins, and carbohydrates, among others (Marshall et al., 2010).

To date, Precambrian kerogenous microfossils have been studied using visible laser wavelengths (e.g., ~457–532 nm), the use of deep-UV Raman spectroscopy largely limited to studies of terrestrial organic compounds (Eshelman et al., 2014; Abbey et al., 2017), amorphous kerogen of unknown biological affinity in Mars-relevant lithologies (Beegle et al., 2014; Shkolyar et al., 2018; Williford et al., 2018), and, in paleobiology, to studies of Eocene fossil ferns (Czaja et al., 2009). This study further expands these data to include deep-UV Raman spectra and imagery of variably altered Precambrian microfossils and detrital kerogen, and builds on previous studies through the direct characterization of deep-UV Raman spectra for kerogenous microfossils of well-established biogenicity and from a variety of thermally altered units, thereby constraining the diversity of possible spectra which might be detected in organic-rich sediments on the surface of Mars.

2. MATERIALS AND METHODS

2.1. Materials studied

As summarized in Table 4-1, the rock samples used in this study come from 14 geologic units and that contain previously identified kerogenous microfossils and organic matter (Schopf et al., 2005) preserved both in bedded and stromatolitic cherts ranging in age from ~2,520 Ma to ~740 Ma (and one Cambrian-age unit ~400 Ma). Microfossils are identified here on the basis of optically discernable morphologies that seemingly correspond with a kerogenous composition and

have been established as biogenic on the evaluation of numerous metrics, including a three-dimensional (3-D) morphology as documented by optical microscopy, confocal laser scanning microscopy (CLSM), or 3-D visible-Raman imagery (e.g., Schopf and Kudryavtsev, 2005; Schopf and Kudryavtsev, 2009), in addition to characterizations of the depositional environment and various geochemical parameters (e.g., isotopes), where possible (see Schopf et al., 2005 and references therein). The majority of the samples have experienced only minor thermal metamorphism, the most thermally altered having been subjected to temperatures associated with greenschist facies metamorphism (~200–450 °C). The samples studied are mostly fine-grained silicified stromatolites, the silica evidently emplaced during early diagenetic replacement of primary carbonates in shallow-marine phototrophic environments (Perry and Lefticariu, 2013). The thin section-embedded microfossils here analyzed, all interpreted to be benthic or planktonic photoautotrophs, are predominantly prokaryotic microorganisms of relatively simple morphologies (e.g., filaments and spheroids), augmented by a few larger and more complex eukaryotic spheroidal to ellipsoidal acritarchs present within the Kalkberg Formation (Table 4-1).

2.2. Sample preparation and optical microscopy

Fossiliferous samples of Precambrian cherts were prepared as polished ~50- to 150 μm-thick petrographic thin sections and surveyed using transmitted light optical microscopy using 10x, 25x and 40X microscope objectives to locate preserved microfossils and associated detrital kerogen appropriate for Raman spectroscopic analysis. Thin sections were cleaned and sonicated multiple times in deionized (DI) water and ethanol for up to 1 min., then rinsed in DI water after each treatment and dried overnight in a vacuum oven at 50 °C. After cleaning the upper surface of each thin section, the microfossils and associated kerogen selected for Raman analysis were

photographed with transmitted and reflected light at multiple magnifications (up to 150X) using a Leica DM6000 photomicroscope housed at the NASA Jet Propulsion Laboratory (JPL) Astrobiogeochemistry Laboratory (the abcLab).

2.3. Deep-UV Raman spectroscopy

Deep-UV Raman point spectra and two-dimensional Raman images were acquired and used to characterize the variably altered carbonaceous microfossils and associated detrital kerogen embedded in the chert matrices. These Raman data were acquired at the Raman Laboratory of UCLA's Center for the Study of Evolution and the Origin of Life using a T64000 Coherent Innova 90C FreD argon ion laser (Schopf and Kudryavtsev, 2005), a triple-stage confocal laser-Raman system configured with a laser excitation wavelength of 257.25 nm, a spectral window centered at ~1,450 cm^{-1} and a ~1-μm spot size. Sample targets (microfossils and background kerogen) were located for analysis using an Olympus BX41 microscope equipped with a 40x UV objective (NA = 0.50), and Raman point spectra were collected for 100 s and processed using the software LabSpec (v.5; Horiba Instruments Inc.). Two-dimensional Raman geochemical maps obtained for kerogenous microfossils and stromatolitic laminae were typically acquired across a ~20×20-μm area at ~1–15 μm depth within the thin section, with each individual spectrum measured for 3 s and having a vertical resolution of ~3 μm. The deep-UV Raman maps thus collected document the spatial distribution of fossil and detrital kerogen within the encompassing chert matrix, and occasional presence of carbonate mineral grains (Fig. 4-5).

Deep-UV Raman analyses were calibrated relative to a highly ordered pyrolytic graphite standard (HOPG SPI–3, Structure Probe, Inc., West Chester, PA) with a characteristic Raman shift of 1,583 cm^{-1}, the same standard used by Czaja et al. (2009), and spectra of kerogen reported here

are normalized to the intensity of the G-band (~1,600 cm^{-1}) for direct comparison. Laser power at the specimen did not exceed 1 mW.

Background noise for each spectrum was subtracted using a linear baseline between 950 and 1800 cm^{-1}, and processed kerogen spectra were deconvoluted using the software package PeakFit (v.4.12; SeaSolve Software Inc., Massachusetts, U.S.A.) with a Gaussian-Lorentzian function, following protocols of previous Raman geothermometry studies (e.g., Beyssac et al., 2002; Kouketsu et al., 2014). Carbonaceous materials preserved in ancient sedimentary rocks typically exhibit two main Raman bands in the first-order region (~1000–1800 cm^{-1}) of the spectrum: the "disordered" (D) band at ~1350 cm^{-1}, and the "graphitic" (G) band at ~1600 cm^{-1} (Tuinstra and Koenig, 1970; Nemanich and Solin, 1979; Pasteris and Wopenka, 1991). Deconvolution of Raman spectra for kerogen incorporates multiple D-bands in addition to one peak (G) at ~1580 cm^{-1}, including the D1-band (1350 cm^{-1}), D2-band (1620 cm^{-1}), D3-band (1510 cm^{-1}), and D4-band (1245 cm^{-1}) (e.g., Kouketsu et al., 2014), and occasionally several other such bands between ~1200–1500 cm^{-1} (Schopf et al., 2005; Czaja et al., 2009; Henry et al., 2019). The present study assesses the peak center positions and relative intensities of these individual kerogen bands and their variation among the samples as a function of their increasing thermal maturity.

2.4. Deconvolution of deep-UV Raman spectra

This study performed multiple deconvolutions using the Raman bands for kerogen invoked in previous studies, namely that of the Raman geothermometer described by Kouketsu et al. (2014). Thus, the three main bands of the disordered D band (D1, D3, D4) were included at fixed peak positions, whereas the G-band was treated as one band (i.e., including the G- and D2-bands) with an unfixed (~1580–1620 cm^{-1}) position to document the relative shift in band width (FWHM)

and peak position with increasing thermal maturity. Kerogen spectra lacking a visible D-band (~1350 cm^{-1}) were fitted directly with a single G-band (~1600 cm^{-1}). Quartz peaks were also included in the deconvolutions, in order to provide a direct comparison with changes in the Raman spectra of thermally altered kerogen.

3. RESULTS

3.1. Optical microscopy

Microfossils exhibiting distinctive morphologies and varying states of morphological decomposition are present in 11 of the 14 carbonaceous thin section samples studied here, nearly all of which contain finely dispersed particulate "background" kerogen from unknown biological sources (i.e., allochthonous or autochthonous). Spheroidal, filamentous, and colonial microfossils of unequivocal cellular origin and associated detrital kerogen (see Schopf et al., 2005 and references therein) are preserved three-dimensionally throughout the various thin sections, permitting them to be analyzed at depth using the confocal laser Raman system employed here.

3.2. Deep-UV Raman spectroscopy

The deep-UV Raman point spectra of all kerogenous microfossils and detrital kerogen obtained here exhibit two first-order kerogen bands in the ~1200–1800 cm^{-1} region. Second-order bands (2200–3400 cm^{-1}) typically observed in Raman analyses using visible laser wavelengths are markedly subdued or absent from the kerogen spectra obtained using deep-UV laser wavelengths (c.f. Czaja et al., 2009; Fig. 4-4). In such spectra, the principal kerogen band at ~1600 cm^{-1} is the G-band, and the secondary band at ~1350 cm^{-1} represents the D-band. However, both of these first-

order bands are relatively broad and consist of multiple subsidiary bands, the presence of which can be documented through deconvolution. The data obtained from deconvolution of such deep-UV Raman kerogen spectra, summarized in Table 4-2, yield four distinct and related parameters for evaluation and comparison with the thermal maturity of the geologic units from which the samples were derived (Table 4-3). These patterns, ordered by their prominence in the spectra obtained, are (1) the presence and intensity of the D-band(s); (2) the peak center position of the G-band; (3) the breadth (i.e., full width at half maximum; FWHM) of the G-band; and (4) the difference in peak center positions between the G-band and associated quartz ($\Delta_{G\text{-}qtz}$). For kerogen samples of varying thermal maturity, the peak center position and breadth of the G-band (G-FWHM) show characteristic geochemical maturity-correlated spectral changes, low maturity samples having peaks progressively shifted closer to ~1610 cm^{-1} and increasingly higher G-FWHM values, changes reflecting a gradual broadening of their component G-band (Tables 4-2 and 4-3; Fig. 4-3). In contrast, higher maturity samples exhibit G-band peaks shifted closer to ~1580 cm^{-1} and lower G-FWHM values indicating the relative narrowing and sharpening of the spectral peaks.

4. DISCUSSION

The direct detection of organic-rich sedimentary rocks, stromatolites, or microfossils on Mars or in Mars rocks brought to Earth for detailed study would represent the most promising astrobiological biosignature yet discovered, a possibility that has spurred the currently ongoing (since July 30, 2020) Mars 2020 rover mission. Indeed, *Perseverance*, the Mars 2020 rover is tasked with identifying such samples – the first-order focus of the mission being the detection and

in situ study of Martian sedimentary rocks – the samples thus identified to be cached and brought to Earth in the early 2030s which would enable their detailed geochemical and paleobiological analysis. If potential signs of ancient life are detected in rock samples from Jezero crater, and if in situ measurements indicate that they are most likely indigenous rather than spurious signals from terrestrial contaminants, the primary question will be: "How do these putative biosignatures compare to demonstrably biogenic organic matter and fossils from the early Earth?".

To provide firm data by which to address this question, this study has examined a suite of unquestionably biogenic *bona fide* carbonaceous Precambrian microfossils and associated detrital kerogens preserved in cherts from 14 geologic units of varying thermal maturities that collectively span more than 1 billion years of Earth history. Particularly relevant to a comparison of the results here reported with those to be obtained by Mars 2020 is the fact that the present study has employed deep-UV Raman spectroscopy analyses designed to be comparable to those of the SHERLOC instrument on the Mars 2020 rover. Moreover, and to assure that the results here reported are appropriate for such comparison, all of the samples examined using deep-UV laser excitation wavelengths have previously also been measured via Raman spectroscopy with visible laser wavelengths (Schopf et al., 2005; Czaja et al., 2016), data that establish the efficacy of this now newly applied technique to determination of the geothermal maturity of the analyzed kerogens.

4.1. Deep-UV Raman spectroscopy

The deep-UV Raman spectra of the kerogens studied here are similar to those measured in samples from previous studies using similar laser excitation wavelengths (Ferrari and Robertson, 2001, 2004; Casiraghi et al., 2005; Czaja et al., 2006, 2009; Shkolyar et al., 2018), with two first-order Raman bands present (D-band ~1350 cm^{-1}; G-band ~1600 cm^{-1}). In comparison to Raman

measurements using visible laser wavelengths, deep-UV analyses induce a pronounced Raman resonance effect which yields an enhanced G-band intensity relative to that of the D-band (Fig. 4-1). These first-order bands are composed of multiple subsidiary peaks which can be deconvoluted. The G-band is composed of two "peaks", herein referred to as the G peak (also known as the G-function or ordered "O" peak; see Henry et al., 2019 for a recent review) at ~1580 cm^{-1} and the D2 peak at ~1610–1620 cm^{-1}, peaks thus defined to differentiate them from the more broadly termed G- and D-bands (Beyssac et al., 2002; Aoya et al., 2010; Kouketsu et al., 2014; Henry et al., 2019). Although these peaks can often be differentiated and decomposed in Raman spectra of kerogen measured using visible laser wavelengths, when using deep-UV laser wavelength settings the G-band cannot be so clearly separated into its component G- and D2-peaks (Wopenka & Pasteris 1993; Beyssac et al. 2003). Though both peaks are present in thermally immature kerogens, the G-band does not exhibit any apparent bifurcation with increasing thermal maturity in deep-UV, as is observed in the visible-laser Raman spectra of kerogen (Fig. 4-1; cf. Beyssac et al., 2002; Schopf et al., 2005; Czaja et al., 2009; Kouketsu et al., 2014). Instead, the G-band features one broad "peak" that shifts prominently from a center position of ~1611 cm^{-1} to ~1588 cm^{-1} with the increasing geochemical maturity of the samples studied here, and ultimately results in lower G-FWHM values as the thermal maturation of kerogen results in a single graphitic (G) peak at 1583 cm^{-1} (Tables 4-2 and 4-3; Figs. 4-1–4-3).

For deep-UV Raman measurements, the D-band (~1350 cm^{-1}) is highly reduced in its relative intensity to the G-band compared to measurements made using visible laser wavelengths, yet the D-band nevertheless occurs in kerogens of relatively low thermal maturity (i.e., RIP < ~5.0; Fig. 4-1) and thus represents a promising signature for the detection of well-preserved organic matter using the SHERLOC deep-UV Raman system onboard the Mars 2020 rover. The D-band

of kerogen is composed of multiple subsidiary peaks, and several possible fittings have been proposed for its deconvolution, most of which contain the D1 (~1350 cm^{-1}), D3 (~1510 cm^{-1}), and D4 (~1245 cm^{-1}) bands (e.g., Beyssac et al., 2002; Kouketsu et al., 2014). In addition, some workers have proposed and sometimes included other peaks such as the D5 (~1260 cm^{-1}) and D6 (~1440 cm^{-1}) bands (Henry et al., 2019). The D1 band has also been split into multiple peaks at ~1335 cm^{-1}, ~1380 cm^{-1}, and 1435 cm^{-1}, and other "unnamed" peaks at ~1170 cm^{-1} and ~1697 cm^{-1} have been attributed to non-aromatic components (e.g., Schopf et al., 2005; Czaja et al., 2009), although these minor bands are rarely fitted in Raman deconvolutions (Henry et al., 2019). Kerogen-rich samples analyzed on Mars which contain a prominent D-band in addition to the resonance-enhanced G-band may contain useful paleobiological information, and should be considered high priority targets for sample caching and future return to Earth as part of the planned Mars Sample Return mission.

Raman spectroscopy has long been heralded for its non-destructive nature (Ferralis et al., 2016; Marshall et al., 2010; Pasteris and Wopenka, 2003; Schopf et al., 2005). Nevertheless, it has also been suspected that shorter laser excitation wavelengths (i.e., deep-UV) and/or higher laser power analyses (>15 mW over a ~1-μm spot) may alter preserved carbonaceous material (Schopf et al., 2002; Czaja et al., 2009), which would be highly undesirable for analyses of pristine extraterrestrial organic matter. The typical laser power for studies of kerogenous microfossils using visible laser wavelengths is <15 mW over a ~1-μm spot, preventing any potential radiation damage to such specimens; however, deep-UV Raman analyses using similar laser power settings are still thought to have destructive effects on macromolecular kerogen (Schopf et al., 2002; Czaja et al., 2006, 2009). For these reasons, it has been proposed that measuring kerogens using deep-UV laser wavelengths can cause sample heating or chemical alteration, effects that might be avoided by use

of fused quartz microscope slides which are transparent to UV light (Czaja et al., 2009). However, no such alteration was observed in the kerogen samples studied here and there was no discernable difference in the spectra of kerogen measured on glass slides compared to those made of quartz, although there are noticeable differences between the spectra of the glass and quartz-fused slides themselves (Fig. 4-6).

Other vibrational bands documented in this study include those of specific standards and minerals. Typical standards used for Raman spectroscopy, such as the silicon (Si) wafer having a peak center of ~520 cm^{-1} when measured using visible laser wavelengths (e.g., Allwood et al., 2006; Marshall et al., 2007; Henry et al., 2018), is not usable for deep-UV measurements as its prominent first-order band has very weak Raman scattering efficiency at such excitation wavelengths. This study thus employed a different calibration standard, a highly ordered pyrolytic graphite (HOPG) standard with a first-order peak center of ~1583 cm^{-1} that is present using both visible and deep-UV laser excitation wavelengths (Fig. 4-4). Other standards have been used, including organic compounds such as cyclohexane for visible wavelengths and alanine for deep-UV Raman measurements (Shkolyar et al., 2018). The mineral quartz (SiO_2), which dominates the chert matrix of the thin section samples studied here, produces a strong first-order peak at ~465 cm^{-1} (second-order peaks at ~700 cm^{-1}, ~810 cm^{-1}, ~1080 cm^{-1}, and ~1160 cm^{-1}) and provides an indirect ("internal") standard from within the sample spectra by which to evaluate the relative changes in peak positions ($\Delta_{G\text{-}qtz}$) due to changes resulting from the thermal maturation of fossil kerogen (Tables 4-2 and 2-3; Fig. 4-3).

4.2. Deep-UV Raman spectra of Precambrian kerogens

The macromolecular structure of kerogen changes with increasing thermal maturity – as evidenced by Raman spectroscopy – becoming increasingly ordered as kerogen is transformed to graphite in metasedimentary rocks. Graphite is composed of pure carbon graphene layers arranged in a planar crystal lattice, the single first-order Raman peak (G) at ~1580 cm^{-1} corresponding to the Raman active E_{2G2} vibration mode of graphite with D^4_{6h} symmetry (i.e., in-plane vibrations of aromatic carbons) (e.g., Song et al., 1976; Wang et al., 1990; Beyssac et al., 2002; Ferrari and Robertson, 2000).

Additional first-order bands (D-bands) appear in fossilized, less ordered (i.e., low maturity), carbonaceous matter arising from "defects" in the graphitic structure. For example, the prominent and broad D1-band at ~1350 cm^{-1} is often attributed to disorder in the graphitic structure due to the presence of such heteroatoms as hydrogen, oxygen and nitrogen (Beyssac et al., 2002). Similarly, the D2-band (~1620 cm^{-1}) is related to the aromatic ring-stretching vibration (i.e., the "Я" motion) of PAHs, whereas the D3-band (~1510 cm^{-1}) and D4-band (1245 cm^{-1}) are ascribed to aromatic ring deformation and total symmetric breathing (i.e., the "A" motion) of PAHs (Mapelli et al., 1999) and interlinking polyene chains in unaltered kerogens (Czaja et al., 2009).

For sedimentary organic matter, Raman analyses using a laser excitation wavelength in the deep-UV can induce specific resonance effects within bands of various organic compounds, including macromolecular kerogen (Barańska et al., 1987; Marshall et al., 2010). Such resonance effects drastically increase the Raman scattering efficiency of certain organics (e.g., Beegle et al., 2015; Abbey et al., 2017), for kerogen, the G-band (~1600 cm^{-1}) in particular (Fig. 4-1; Czaja et al., 2009; Shkolyar et al., 2018). Such enhancement of the G-band relative to the D-band in kerogen is thought to be due to the aromatic rings and conjugated C=C bonds being preferentially enhanced

relative to the bonds of the saturated hydrocarbons co-occurring in thermally immature kerogens. However, the exact nature and origin of these vibrational modes remains unresolved (e.g., Tuinstra and Koenig, 1970; Robertson, 1986; Wang et al., 1990; Cuesta et al., 1994; Jawhari et al., 1995; Escribano et al., 2001; Kouketsu et al., 2014), and the peak center positions and relative intensities of these individual kerogen bands are also known to shift with varying laser excitation wavelengths, an alternative result of the Raman resonance effect (e.g., Vidano et al., 1981; Wang et al., 1990; Matthews et al., 1999; Sato et al., 2006).

4.3. Applications to the Mars 2020 mission and SHERLOC instrument

Although more than 99% of biologically fixed carbon is ultimately recycled prior to being incorporated in the rock record (Holland, 1984), sedimentary reduced organic carbon (kerogen) still represents the "largest pool of organic matter on Earth" (Farmer and Des Marais, 1999) constituting more than 95% of all sediment- and ultimately rock-deposited organic matter. From this it follows that such complex macromolecular carbon-based structures can be expected to be encountered on Mars in association with other organic compounds (Kanavarioti and Mancinelli, 1990; Zolotov and Shock, 1999; Benner et al., 2000). Eigenbrode et al. (2018) reported the detection of "geologically refractory organic macromolecules" from ~3.5 billion-year-old lacustrine mudstones in Gale crater, which closely resemble complex organic matter found within carbonaceous chondrites (e.g., Cronin et al., 1988; Pizzarello and Shock, 2010) and, as well, biologically derived kerogens on Earth (McKirdy and Hahn, 1982; Vandenbroucke and Largeau, 2007).

The Mars 2020 mission – scheduled to land in February 2021 – continues to build on the findings of previous Mars missions and seeks to explore the potential preservation of organic

matter within ancient sedimentary rocks and regolith in Jezero crater. The Mars 2020 rover, *Perseverance*, is equipped with the SHERLOC Raman instrument using a deep-UV laser excitation wavelength of 248.6 nm, a configuration selected to avoid complications due to overlapping fluorescence signals, Raman scattering and fluorescence becoming energetically separated in UV (Tarcea et al., 2007), and to make use of resonance enhancements from organic compounds and certain minerals which aid in their detection (e.g., Beegle et al., 2015; Abbey et al., 2017).

The SHERLOC Raman laser has a ~50 μm spot size and emits 400 laser pulses over 10 seconds for each spot, rastered over a 1x1 mm Region of Interest (ROI), which produces Raman (and fluorescence) "micro-maps" (see Beegle et al., 2015). For comparison, the Raman maps acquired in the present study used a ~1 μm laser spot rastered over a ~20x20 μm area (i.e., much higher spatial resolution than the SHERLOC instrument), with the Precambrian microfossils analyzed here ranging in size from ~1–50 μm. Thus, it appears unlikely that the deep-UV Raman analyses to be performed during the Mars 2020 mission will be capable of resolving individual kerogenous microfossils in situ on Mars. Despite this, the possibility of discerning organic-rich stromatolitic laminae and textures or larger kerogenous structures (e.g., biofilms) remains feasible, which may logically inform sample priority for those to be cached on the surface and returned to Earth during the Mars Sample Return mission.

Any prominent Raman bands exhibited between ~1580 cm^{-1} (graphite) and ~1620 cm^{-1} (kerogen) should be considered high-priority targets, particularly if accompanied by a corresponding broad band in the ~1100–1500 cm^{-1} region, which might indicate the existence of well-preserved organic matter that could contain compounds of astrobiological interest, such as molecular biomarkers (e.g., lipids, pigments, etc.). Other biologically produced organic

compounds (e.g., lignin, β-carotene) can also yield Raman spectra comparable to that of thermally immature kerogen, having a band at ~1600 cm^{-1} and, most notably, a bifurcated D-band with two resolvable peaks (Czaja et al., 2009). Additional astrobiologically-relevant organic compounds (and minerals) not yet studied by use of deep-UV Raman spectroscopy may produce spectral features similar to the kerogens studied here and therefore warrant further consideration and analysis (Abbey et al., 2017).

Data acquired by Mars-orbiting satellites indicate that minerals commonly occurring in geochemically altered sedimentary rocks are present in Jezero crater near the landing site of the Mars 2020 rover, including clays and carbonates of possible lacustrine origins (e.g., Ehlmann et al., 2008a, 2008b; Horgan et al., 2020). Recent evidence for hydrated silica (Tarnas et al., 2019) is relevant to the chert-permineralized microfossils studied here and represents another promising lithology and astrobiological target worth exploring by both in situ investigation and potential sample return to Earth.

The stratigraphic record of Jezero crater dates back to the Noachian ~4.1–3.7 Ga with possible fluvial activity extending into the ~3.7–2.9 Ga Hesperian (e.g., Mangold et al., 2020), coinciding with periods of extensive aqueous activity on Mars and the origin of life on Earth prior to ~3.5 Ga. The preservation of fossil microorganisms from these early periods of Mars history is dependent on diverse physical, chemical, and biological factors. Rapid entombment of microbial communities by permineralization in aqueous (i.e., marine, lacustrine) chemical sediments – most commonly chert (microcrystalline SiO_2) – is typically required for the cellular preservation of "life-like" prokaryotic microfossils, whether benthic or planktonic (Farmer and Des Marais, 1999; Kremer et al., 2012). Moreover, such early diagenetic silicification may also help prevent morphological or geochemical alteration over geological timescales (Oehler and Schopf, 1971;

Oehler, 1976; Bartley, 1996; Alleon et al., 2016; Manning-Berg et al., 2019; Osterhout et al., 2019).

The combined effects of these processes – known as the "armoring effect" (Wada and Suzuki, 1983) – could potentially shield preserved biosignatures from destructive effects on the surface (or subsurface) of Mars, including oxidation, cosmic irradiation, or thermal maturation. Interactions between ionizing radiation (e.g., UV- and gamma-rays) and organic matter on Mars would almost certainly lead to the breakdown of macromolecular organic compounds (Benner et al., 2000; Court et al., 2006; Pavlov et al., 2012;), the UV-flux at the Mars surface (45 W/m^2) being some nine times greater than that at the surface of the Earth. Such breakdown would necessarily result in the alteration or degradation of Raman biosignatures (Court et al., 2007; Dartnell et al., 2011, 2012), or conversely, to the buildup of macromolecular kerogen-like structures from smaller organic compounds (e.g., Cataldo et al., 2004). Because Mars has evidently lacked plate tectonics for most or all of its history, ancient sedimentary rocks are likely to have experienced lower thermal alteration overall compared to coeval rocks on the early Earth. Such factors further support the high scientific demand and priority for the detection of kerogenous, silicified sedimentary rocks on Mars by the *Perseverance* rover, and the return of promising astrobiological specimens to Earth for more rigorous paleobiological analyses, including the microscopic search for fossilized microorganisms and preserved evidence of extraterrestrial biological evolution.

TABLES

Geologic unit	Locality	Estimated age (Ma)	Metamorphic grade	RIP	H/C	Fossil specimens analyzed	Background kerogen?
Gunflint	Ontario, Canada	2,090	Subgreenschist	8.8	Unknown	*Gunflintia*, *Huroniospora*	✓
Gaoyuzhuang	Jixian, China	1,425	Essentially unmetamorphosed	8.5	0.45	*Eomycetopsis, Lyngbya*-like sheath	✓
Kalkberg	New York, USA	395[a]	"Low grade"	8.5	Unknown	*Multiplicisphaeridium*, *Micrhystridium*, spheroidal unicell (unnamed)	✓
Bungle Bungle	Dixon Range, Western Australia	1,364	Unknown	7.5	0.37	Large sheath (oscillatoriacean)	n.d.
Wumishan	Jixian, China	1,500[b]	Essentially unmetamorphosed	7.4	0.54	*Eomycetopsis*	✓
Dismal Lakes	Northwest Territories, Canada	1,400	Unknown	7.4	0.67	n.d.	✓
Kwagunt	Arizona, USA	850	"Unmetamorphosed"	7.3	0.81	*Eomycetopsis*	✓
Vempalle	Andhra Pradesh, India	1,700	Subgreenschist	5.7	Unknown	Spheroidal unicells (unnamed), cellular filament (unnamed), tubular sheaths (oscillatoriacean)	✓
Paradise Creek	Queensland, Australia	1,650	Unknown	5.3	0.20	n.d.	✓
Beck Spring	California, USA	850	"Slightly to moderately metamorphosed"	4.4	0.14	*Beckspringia communis, Conglobocella troxelii*	✓
Gamohaan	Northern Cape Province, South Africa	2,521[c]	"Below zeolite facies"[c]	4.0[d]	Unknown	*Thiomargarita*-like[d], spheroidal unicell (unnamed)	✓
Skillogalee	Lake Eyre North, South Australia	770	Lower greenschist	3.9	0.22	n.d.	✓
Auburn	Leasingham, South Australia	740[e]	Lower greenschist	1.5	0.17	"Sheath-like filaments"	✓
River Wakefield	Carrieton, South Australia	775	Lower greenschist	1.0	0.44	*Polybessurus,* colonial spheroids (unnamed)	✓

[a] Husson et al. (2016)
[b] Guo et al. (2016)
[c] Sumner and Bowring (1996)
[d] Czaja et al. (2016)
[e] Preiss (2000)

Table 4-1. List of geologic units studied using deep-UV Raman spectroscopy, ordered according to their Raman Index of Preservation (RIP) values. Estimated ages of the geologic units and their geochemical data are from Schopf et al. (2005) and references therein, except where otherwise noted. n.d.; not determined.

Geologic unit	Peak center (G-band, cm^{-1})	σ	G-FWHM (cm^{-1})	σ	Peak center difference (Δ_{G-qtz}, cm^{-1})	σ	r^2	n
Gunflint	1606.8	3.8	56.6	5.0	1140.7	1.6	0.9900	14
Gaoyuzhuang	1611.4	1.5	52.6	3.9	1141.3	1.0	0.9837	24
Kalkberg	1607.5	1.0	57.2	1.5	1140.6	0.5	0.9884	16
Bungle Bungle	1608.8	-	45.3	-	1141.1	-	0.9903	1
Wumishan	1607.4	1.5	63.2	3.9	1138.1	1.4	0.9898	7
Dismal Lakes	1607.2	1.2	67.0	15.5	1138.9	1.1	0.9935	2
Kwagunt	1610.5	1.2	67.0	3.8	1140.6	0.8	0.9912	16
Vempalle	1602.9	1.4	46.4	1.2	1132.1	1.1	0.9791	7
Paradise Creek	1599.1	0.7	44.9	1.8	1129.8	0.4	0.9900	4
Beck Spring	1595.5	1.2	44.1	2.7	1127.1	2.7	0.9638	6
Gamohaan	1591.8	1.6	42.6	0.7	1127.3	1.3	0.9906	9
Skillogalee	1590.6	0.7	43.5	2.0	1127.7	0.4	0.9939	2
Auburn	1587.9	1.2	39.4	2.7	1122.9	0.5	0.9914	8
River Wakefield	1595.1	2.1	44.7	2.8	1129.5	2.5	0.9426	6

Table 4-2. Results of deep-UV Raman measurements for microfossils and detrital kerogen for geologic units studied, ordered according to their RIP values listed in Table 1. For the kerogen G-band, the average peak center position, full width at half maximum (G-FWHM), and peak center difference between the G-band and quartz peak (Δ_{G-qtz}) are listed alongside the standard deviation (σ; 1SD), average r-squared values (r^2) representing average goodness of fit for the deconvolutions, and number of Raman spectra analyzed (n).

Geologic unit	Sample	Analysis ID	Description	Peak center (quartz, cm^{-1})	Peak center (G-band, cm^{-1})	G-FWHM (cm^{-1})	r^2	Peak center difference ($\Delta_{G\text{-}qtz}$, cm^{-1})
Auburn								
	AD-BF-1-1-A	10257	"Sheath-like filament"	463.52	1585.83	33.11	0.9817	1122.31
	AD-BF-1-1-A	10259	"Sheath-like filament"	463.18	1586.23	40.44	0.9957	1123.05
	AD-BF-1-1-D	10263	Background kerogen	465.57	1588.13	38.32	0.9938	1122.56
	AD-BF-1-1-D	10265	"Sheath-like filament"	465.13	1588.31	41.24	0.9882	1123.18
	AD-BF-1-1-D	10267	"Sheath-like filament"	466.12	1588.34	40.99	0.9939	1122.22
	AD-BF-1-1-D	10269	Background kerogen	465.37	1588.70	39.89	0.9941	1123.33
	AD-BF-1-1-D	10273	Background kerogen	465.14	1588.79	41.00	0.9914	1123.65
	AD-BF-1-1-D	10275	Background kerogen	466.42	1589.26	39.90	0.9925	1122.84
		Average		**465.06**	**1587.95**	**39.36**	**0.9914**	**1122.89**
		St. dev.		1.15	1.24	2.69	0.0045	0.50
Beck Spring								
	BeckSpring-4-B	10351	*Beckspringia communis*	469.25	1594.12	41.44	0.9926	1124.87
	BeckSpring-4-B	10353	*Beckspringia communis*	467.50	1596.98	45.80	0.9337	1129.48
	BeckSpring-4-B	10355	*Beckspringia communis*	466.82	1596.34	47.74	0.9417	1129.52
	BeckSpring-4-B	10357	*Conglobocella troxelii*	470.31	1594.07	42.34	0.9908	1123.76
	BeckSpring-4-B	10359	*Conglobocella troxelii*	466.79	1596.34	45.93	0.9386	1129.55
	BeckSpring-4-B	10362	Background kerogen	469.96	1595.08	41.37	0.9856	1125.12
		Average		**468.44**	**1595.49**	**44.10**	**0.9638**	**1127.05**
		St. dev.		1.59	1.24	2.72	0.0285	2.74
Bungle Bungle								
	BUNG-159-1A	10391	Large sheath (oscillatoriacean)	467.77	1608.84	45.34	0.9903	1141.07
Dismal Lakes								
	A-42-h-1	10388	Background kerogen	468.24	1606.36	77.89	0.9958	1138.12
	A-42-h-1	10389	Background kerogen	468.35	1608.05	56.02	0.9911	1139.70

		Average		**468.30**	**1607.21**	**66.96**	**0.9935**	**1138.91**
		St. dev.		0.08	1.20	15.46	0.0033	1.12
Gamohaan								
	GCB-13-1-2F	10227	Background kerogen	463.31	1590.59	42.43	0.9894	1127.28
	GCB-13-1-2F	10228	Background kerogen	463.41	1590.71	42.41	0.9865	1127.30
	GCB-13-1-2F	10233	Background kerogen	463.68	1592.56	42.45	0.9810	1128.88
	GCB-13-1-2F	10235	Spheroidal unicell (unnamed)	463.59	1593.41	42.19	0.9929	1129.82
	GCB-13-3-1Db	10393	Background kerogen	466.79	1594.02	41.58	0.9927	1127.23
	GCB-13-3-1Db	10394	*Thiomargarita*-like	467.94	1593.90	43.69	0.9942	1125.96
	GCB-13-3-1Db	10396	*Thiomargarita*-like	464.74	1590.75	42.90	0.9939	1126.01
	GCB-13-3-1Db	10397	*Thiomargarita*-like	463.07	1590.12	41.90	0.9923	1127.05
	GCB-13-3-1Db	10398	*Thiomargarita*-like	463.75	1590.32	43.57	0.9926	1126.57
		Average		**464.48**	**1591.82**	**42.57**	**0.9906**	**1127.34**
		St. dev.		1.73	1.63	0.71	0.0043	1.27
Gaoyuzhuang								
	GAO-1A-2	10084	*Eomycetopsis*	471.13	1612.13	53.13	0.9917	1141.00
	GAO-1A-2	10086	Background kerogen	471.53	1611.57	52.69	0.9917	1140.04
	GAO-1A-2	10088	*Eomycetopsis*	470.96	1611.04	50.20	0.9917	1140.08
	GAO-1A-2	10090	Background kerogen	470.74	1611.21	51.84	0.9905	1140.47
	GAO-1A-2	10093	Background kerogen	470.08	1611.30	52.37	0.9929	1141.22
	GAO-1A-2	10094	*Eomycetopsis*	468.51	1609.79	61.33	0.9884	1141.28
	GAO-1A-2	10096	Background kerogen	466.83	1605.36	50.43	0.9138	1138.53
	GAO-1A-2	10097	*Eomycetopsis*	469.66	1612.59	56.29	0.9901	1142.93
	GAO-1A-2	10098	*Eomycetopsis*	470.15	1610.35	66.77	0.9585	1140.20
	GAO-1A-2	10099	Background kerogen	470.42	1612.91	52.24	0.9487	1142.49
	GAO-1A-2	10100	Background kerogen	470.48	1612.63	51.09	0.9793	1142.15
	GAO-1A-2	10101	Background kerogen	470.74	1612.60	52.68	0.9907	1141.86
	GAO-1A-1	10103	Background kerogen	471.36	1612.11	50.82	0.9916	1140.75
	GAO-1A-1	10104	*Eomycetopsis*	469.74	1612.26	50.29	0.9898	1142.52
	GAO-1A-1	10105	*Eomycetopsis*	470.32	1611.38	50.94	0.9906	1141.06
	GAO-1A-1	10107	*Eomycetopsis*	470.29	1611.87	50.48	0.9892	1141.58

	GAO-1A-1	10109	Background kerogen	470.70	1611.48	51.11	0.9906	1140.78
	GAO-1A-1	10110	*Eomycetopsis*	470.33	1612.75	50.83	0.9893	1142.42
	GAO-1A-1	10112	Background kerogen	469.40	1611.17	53.60	0.9909	1141.77
	GAO-1A-1	10113	*Lyngbya*-like	468.39	1610.06	50.85	0.9882	1141.67
	GAO-1A-1	10116	*Eomycetopsis*	470.20	1612.08	52.34	0.9889	1141.88
	GAO-1A-1	10118	Background kerogen	471.25	1611.49	51.11	0.9927	1140.24
	GAO-1A-1	10120	*Eomycetopsis*	469.93	1611.28	50.65	0.9903	1141.35
	GAO-1A-1	10124	*Eomycetopsis*	468.90	1611.21	48.83	0.9892	1142.31
		Average		**470.09**	**1611.36**	**52.62**	**0.9837**	**1141.27**
		St. dev.		1.08	1.52	3.90	0.0183	1.02
Gunflint								
	GF-Sch-4B	10195	*Gunflintia*	470.61	1611.54	55.97	0.9922	1140.93
	GF-Sch-4B	10197	*Huroniospora*	470.48	1611.74	57.01	0.9899	1141.26
	GF-Sch-4B	10199	*Huroniospora*	470.86	1611.25	54.71	0.9922	1140.39
	GF-Sch-4B	10201	*Huroniospora*	470.58	1611.00	55.08	0.9923	1140.42
	GF-Sch-4B	10203	*Huroniospora*	470.65	1611.20	56.49	0.9939	1140.55
	GF-Sch-4B	10207	Filament (unnamed)	464.14	1606.25	52.17	0.9905	1142.11
	GF-Sch-4B	10209	Filament (unnamed)	464.03	1605.69	51.91	0.9873	1141.66
	GF-Sch-4B	10211	*Huroniospora*	463.72	1605.25	55.17	0.9916	1141.53
	GF-Sch-4B	10213	*Huroniospora*	463.08	1604.67	59.01	0.9851	1141.59
	GF-Sch-4B	10215	*Gunflintia*	463.27	1603.92	57.31	0.9925	1140.65
	GF-Sch-1A	10218	Background kerogen	462.37	1605.02	72.64	0.9931	1142.65
	GF-Sch-1A	10219	Background kerogen	463.67	1604.26	55.05	0.9809	1140.59
	GF-Sch-1A	10220	Background kerogen	464.05	1603.90	53.70	0.9838	1139.85
	GF-Sch-1A	10223	Background kerogen	464.26	1600.00	56.22	0.9948	1135.74
		Average		**466.13**	**1606.84**	**56.60**	**0.9900**	**1140.71**
		St. dev.		3.52	3.77	5.00	0.0042	1.62
Kalkberg								
	KALK-2-C	10294	Background kerogen	467.12	1608.88	56.96	0.9906	1141.76
	KALK-2-C	10295	Acritarch (unnamed)	467.68	1607.31	59.79	0.9946	1139.63

	KALK-2-C	10298	Acritarch (unnamed)	466.83	1607.85	55.64	0.9479	1141.02
	KALK-2-C	10300	*Multiplicisphaeridium*	466.48	1607.21	57.06	0.9933	1140.73
	KALK-2-C	10302	Acritarch (unnamed)	466.48	1606.48	60.22	0.9886	1140.00
	KALK-2-C	10306	Acritarch (unnamed)	467.53	1608.16	58.60	0.9907	1140.63
	KALK-2-C	10310	*Multiplicisphaeridium*	467.64	1608.43	55.51	0.9879	1140.79
	KALK-2-C	10312	*Multiplicisphaeridium*	467.65	1607.68	55.79	0.9914	1140.03
	KALK-2-C	10314	*Multiplicisphaeridium*	468.40	1608.75	58.05	0.9910	1140.35
	KALK-2-C	10316	*Micrhystridium*	468.39	1608.39	56.76	0.9931	1140.00
	KALK-2-C	10318	Acritarch (unnamed)	467.25	1607.78	56.81	0.9918	1140.53
	KALK-2-C	10320	Spheroidal unicell (unnamed)	467.59	1608.32	55.39	0.9871	1140.73
	KALK-2-C	10323	Spheroidal unicell (unnamed)	464.63	1605.85	56.63	0.9911	1141.22
	KALK-2-C	10326	*Multiplicisphaeridium*	466.02	1606.56	57.77	0.9922	1140.54
	KALK-2-C	10328	*Multiplicisphaeridium*	465.64	1605.76	56.07	0.9901	1140.12
	KALK-2-C	10329	Acritarch (unnamed)	465.26	1606.13	57.60	0.9923	1140.87
		Average		**466.91**	**1607.47**	**57.17**	**0.9884**	**1140.56**
		St. dev.		1.09	1.04	1.45	0.0110	0.54
Kwagunt								
	C-W-1-B	10139	Background kerogen	471.34	1611.91	69.79	0.9977	1140.57
	C-W-1-B	10140	*Eomycetopsis*	470.74	1612.12	67.73	0.9909	1141.38
	C-W-1-B	10142	*Eomycetopsis*	470.67	1612.37	68.20	0.9911	1141.70
	C-W-1-B	10145	*Eomycetopsis*	469.37	1610.87	67.78	0.9914	1141.50
	C-W-1-B	10147	*Eomycetopsis*	470.19	1611.08	69.42	0.9900	1140.89
	C-W-1-B	10149	*Eomycetopsis*	470.11	1611.00	68.60	0.9925	1140.89
	C-W-1-B	10151	Background kerogen	468.78	1608.46	56.57	0.9809	1139.68
	C-W-1-B	10156	Background kerogen	469.51	1609.22	67.98	0.9951	1139.71
	C-W-1-B	10158	Filament (pyritized)	469.11	1608.97	58.85	0.9876	1139.86
	C-W-1-B	10160	Filament (pyritized)	470.14	1609.30	68.29	0.9954	1139.16
	C-W-1-B	10163	*Eomycetopsis*	469.62	1610.53	69.49	0.9938	1140.91
	C-W-1-B	10166	Filament (pyritized)	470.51	1610.73	68.37	0.9947	1140.22
	C-W-1-B	10169	Filament (pyritized)	470.20	1610.76	68.07	0.9897	1140.56

	C-W-1-B	10170a	Filament (pyritized)	469.76	1611.55	66.46	0.9897	1141.79
	C-W-1-B	10170b	Filament (pyritized)	469.47	1610.00	66.40	0.9890	1140.53
	C-W-1-B	10172	Filament (pyritized)	469.38	1609.17	70.52	0.9897	1139.79
		Average		**469.93**	**1610.50**	**67.03**	**0.9912**	**1140.57**
		St. dev.		0.68	1.20	3.82	0.0039	0.79
Paradise Creek								
	PC-29-6-B	10382	Background kerogen	468.29	1598.54	42.86	0.9909	1130.25
	PC-29-6-B	10384	Background kerogen	468.56	1598.47	44.22	0.9913	1129.91
	PC-29-6-B	10385	Background kerogen	470.44	1599.79	45.32	0.9890	1129.35
	PC-29-6-B	10386	Background kerogen	469.89	1599.61	47.17	0.9889	1129.72
		Average		**469.30**	**1599.10**	**44.89**	**0.9900**	**1129.81**
		St. dev.		1.04	0.69	1.82	0.0013	0.38
River Wakefield								
	RWG-BF-2-4-B	10278	Background kerogen	465.74	1596.04	45.65	0.9392	1130.30
	RWG-BF-2-4-B	10280	*Polybessurus*	465.53	1595.95	45.69	0.9351	1130.42
	RWG-BF-2-4-B	10282	*Polybessurus*	465.37	1596.30	45.43	0.9290	1130.93
	RWG-BF-2-4-B	10284	Colonial spheroids (unnamed)	464.91	1595.11	46.65	0.9313	1130.20
	RWG-BF-2-4-B	10288	Colonial spheroids (unnamed)	465.37	1596.16	45.92	0.9401	1130.79
	RWG-BF-2-4-B	10291	Colonial spheroids (unnamed)	466.42	1590.86	39.12	0.9806	1124.44
		Average		**465.56**	**1595.07**	**44.74**	**0.9426**	**1129.51**
		St. dev.		0.50	2.10	2.79	0.0191	2.50
Skillogalee								
	BOOR-2-2-D1	10241	Background kerogen	463.19	1591.16	44.91	0.9955	1127.97
	BOOR-2-2-A	10248	Background kerogen	462.75	1590.10	42.14	0.9922	1127.35
		Average		**462.97**	**1590.63**	**43.53**	**0.9939**	**1127.66**
		St. dev.		0.31	0.75	1.96	0.0023	0.44

Vempalle								
	CUD-4-B	10364	Oscillatoriacean sheath	470.50	1601.02	48.31	0.9754	1130.52
	CUD-4-B	10366	Cellular filament (unnamed)	472.05	1603.63	47.78	0.9887	1131.58
	CUD-4-B	10368	Oscillatoriacean sheath	470.63	1603.49	46.49	0.9865	1132.86
	CUD-4-B	10370	Oscillatoriacean sheath	469.34	1601.09	45.24	0.9440	1131.75
	CUD-4-B	10372	Background kerogen	469.21	1602.88	45.41	0.9837	1133.67
	CUD-9-A	10378	Background kerogen	472.01	1604.99	46.10	0.9879	1132.98
	CUD-9-A	10379	Spheroidal unicell (unnamed)	471.83	1603.35	45.55	0.9873	1131.52
		Average		**470.80**	**1602.92**	**46.41**	**0.9791**	**1132.13**
		St. dev.		1.22	1.43	1.20	0.0161	1.08
Wumishan								
	WUM-001-a-A2	10332	Background kerogen	468.83	1607.01	65.22	0.9921	1138.18
	WUM-001-a-A2	10333	*Eomycetopsis*	469.64	1607.48	65.08	0.9908	1137.84
	WUM-001-a-A2	10335	*Eomycetopsis*	470.78	1607.44	66.83	0.9916	1136.66
	WUM-001-a-A2	10337	*Eomycetopsis*	469.11	1607.73	65.10	0.9923	1138.62
	WUM-001-a-A2	10342	*Eomycetopsis*	468.31	1604.41	55.28	0.9790	1136.10
	WUM-001-a-A2	10344	Background kerogen	469.63	1609.35	63.94	0.9915	1139.72
	WUM-001-a-A2	10346	Background kerogen	468.80	1608.55	61.22	0.9911	1139.75
		Average		**469.30**	**1607.42**	**63.24**	**0.9898**	**1138.12**
		St. dev.		0.81	1.55	3.91	0.0048	1.40

Table 4-3. Raw data from deconvolutions of deep-UV Raman kerogen spectra for Precambrian microfossils and background detrital kerogen of the 14 geologic units studied.

FIGURES

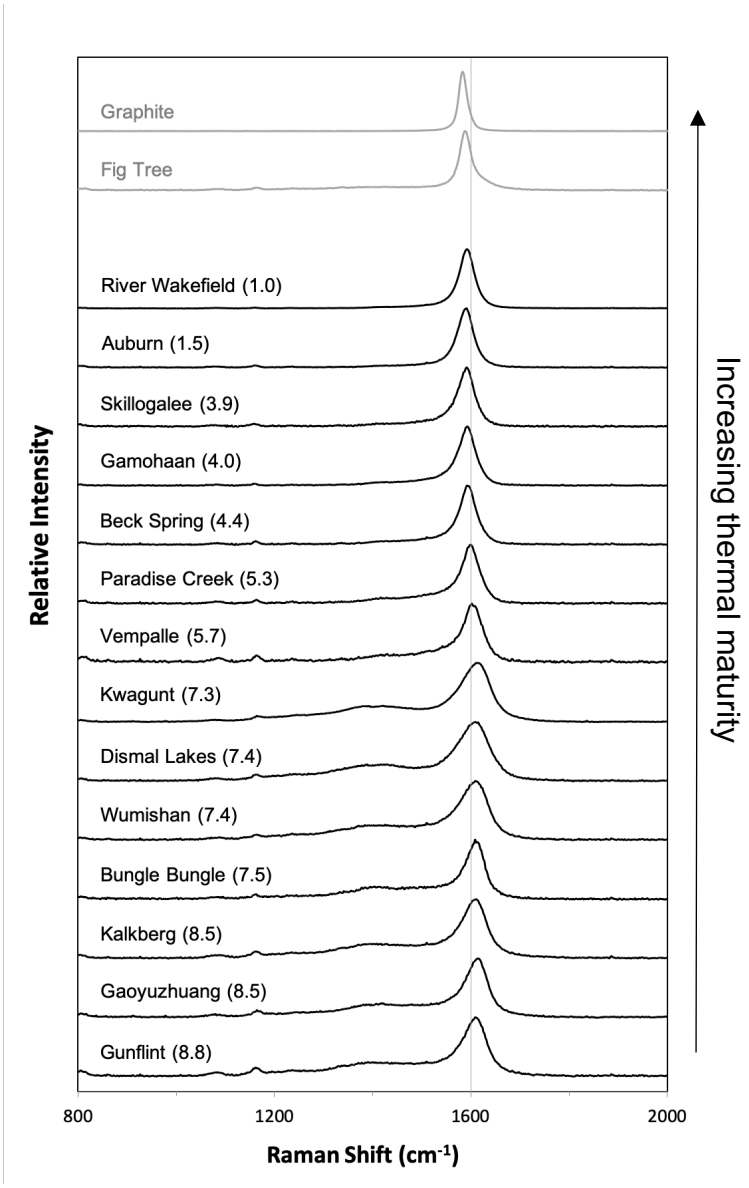

Figure 4-1. Representative Deep-UV Raman spectra of kerogenous microfossils and detrital kerogen for the 14 geologic units studied here (black), and for two analytical standards (gray). Raman Index of Preservation (RIP) values from Schopf et al. (2005) are listed in parentheses for each of the geologic units, with high values (bottom) indicating relatively low thermal maturity and low values (top) representing more thermally altered samples. The vertical gray line at 1600 cm^{-1} helps demonstrate the apparent shift in the peak center of the G-band with increasing maturity.

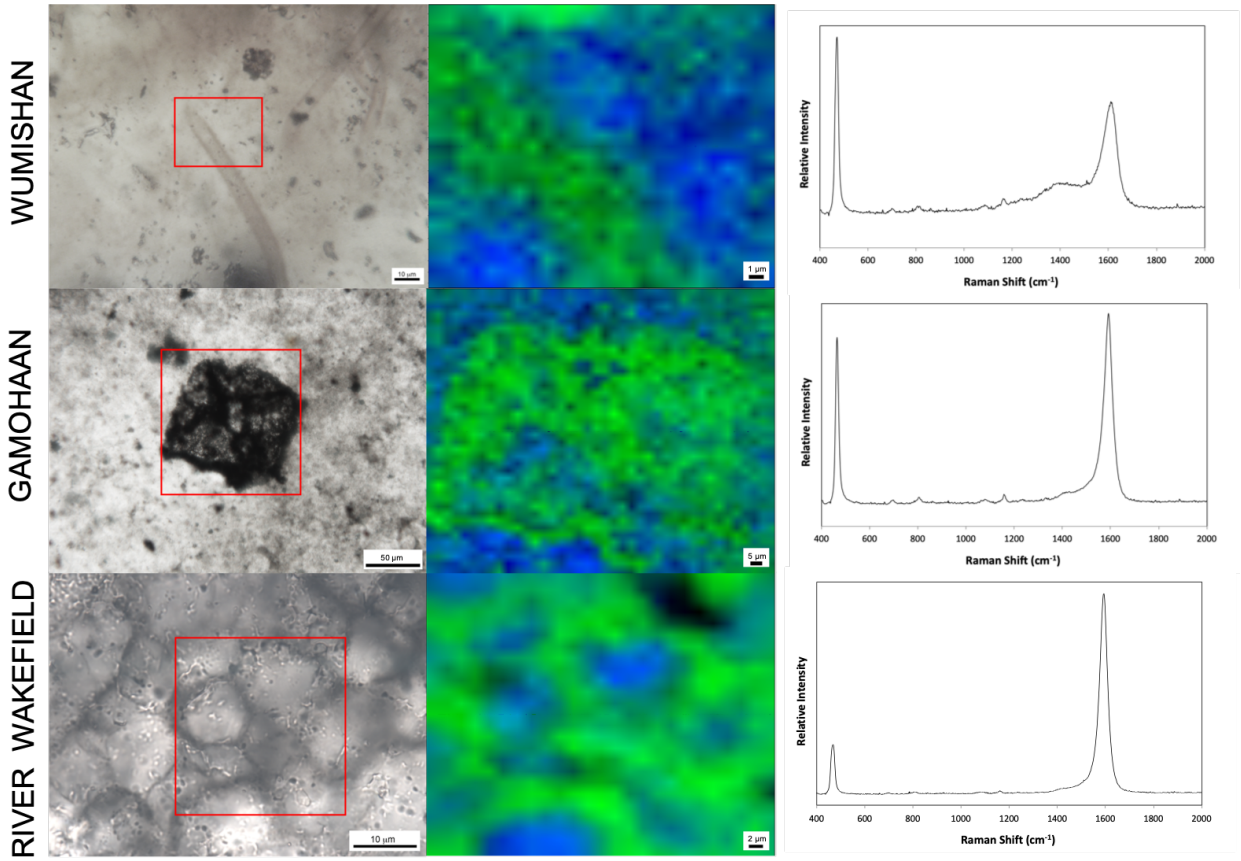

Figure 4-2. Optical photomicrographs (left), 2-D Raman geochemical maps (middle), and corresponding spectra of Raman maps (right) showing kerogen (green, ~1600 cm^{-1}) preserved within chert (i.e., quartz; blue, ~465 cm^{-1}) for a variety of Precambrian microfossils studied here, including filamentous (Wumishan Fm.), coccoidal/colonial (River Wakefield Fm.), and large spherical (Gamohaan Fm.) morphologies. Note differing scale bars (1–50 µm) for each of the images, and no processing was performed on the Raman spectra presented here.

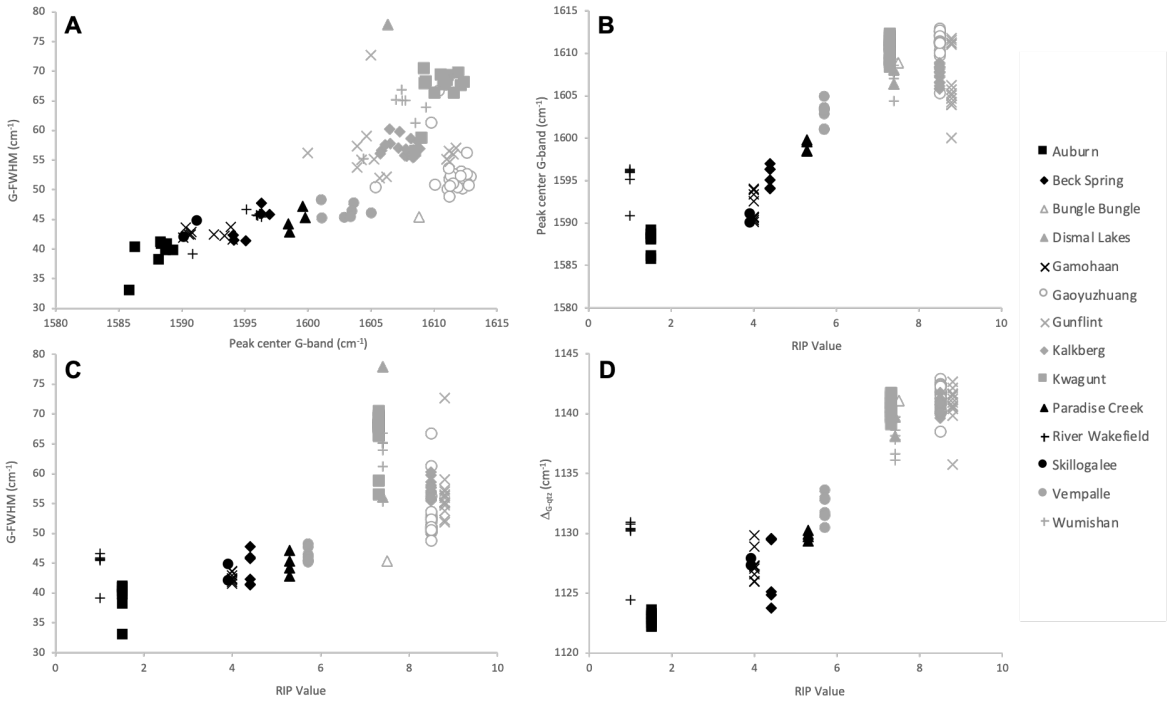

Figure 4-3. Raman data measured for carbonaceous microfossils and detrital kerogen using a deep-UV laser excitation wavelength (257.25 nm). Various metrics show a close relationship with increasing thermal maturity (gray symbols: lower maturity, high RIP; black symbols: higher maturity, low RIP), including (A) peak center position and full width at half maximum (G-FWHM) of the G-band, and the Raman Index of Preservation (RIP) value for each unit compared to (B) the G-band peak center, (C) G-FWHM, and (D) the difference between the peak center positions of the G-band and quartz (Δ_{G-qtz}).

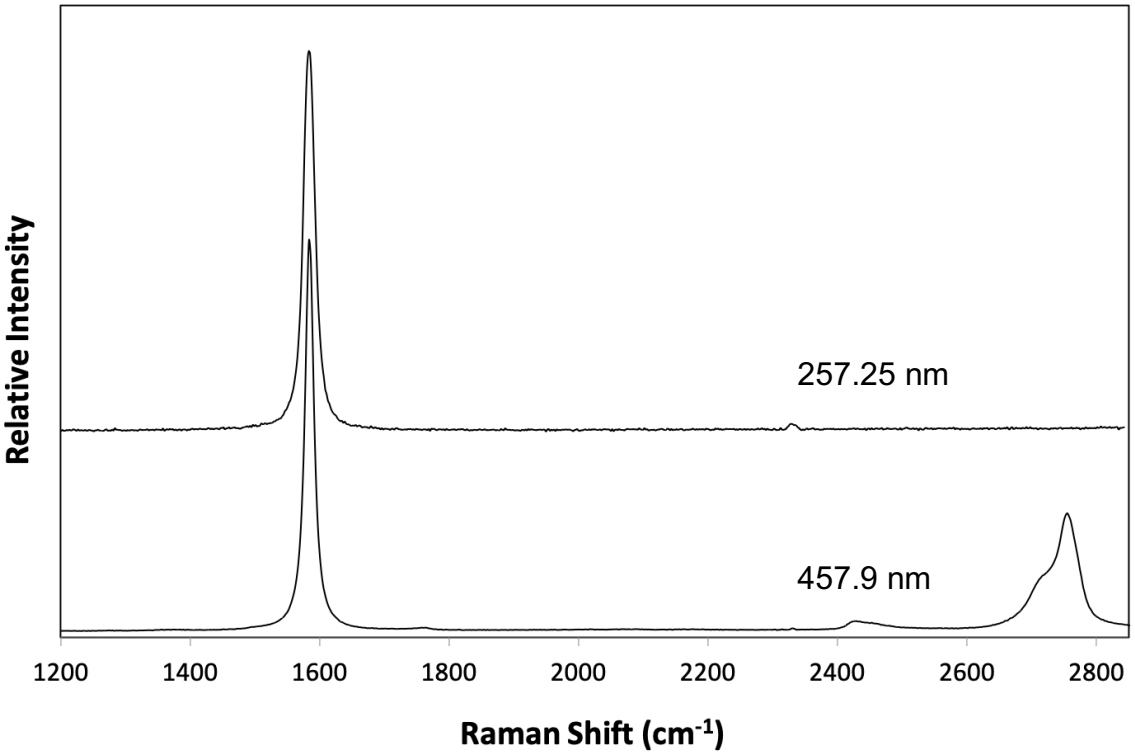

Figure 4-4. Raman spectra of highly oriented pyrolytic graphite (HOPG; ~1583 cm^{-1}) standard measured via Raman spectroscopy using visible (457.9 nm, bottom) and deep-UV (257.25 nm, top) laser excitation wavelengths, demonstrating the presence of second-order bands (~2400–2800 cm^{-1}) observed using visible laser wavelengths, and their absence in deep-UV Raman spectra.

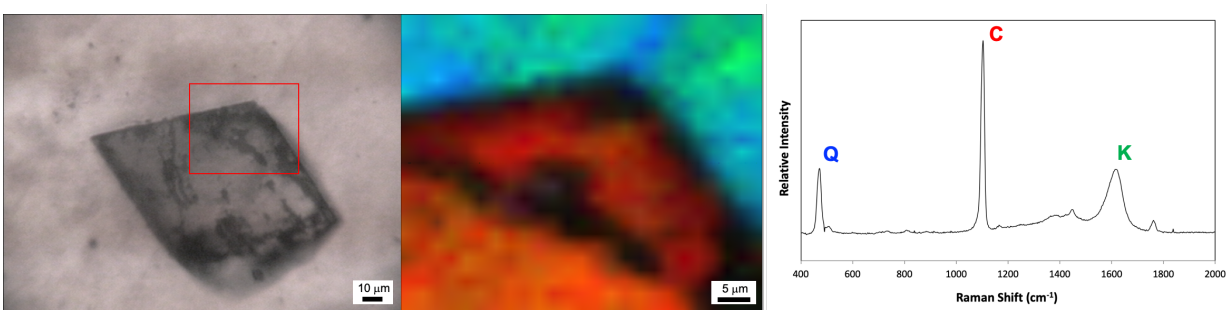

Figure 4-5. Transmitted light, two-dimensional (2-D) Raman image, and corresponding Raman spectrum of carbonate grain within thin section of kerogenous chert from the ~850 Ma Kwagunt Formation. Transmitted light image (left) shows area selected for analysis, with 2-D Raman geochemical map (center), and deep-UV Raman spectrum of map (right) showing map colors for quartz (~465 cm^{-1}; blue), carbonate (~1100 cm^{-1}; red), and kerogen G-band (~1600 cm^{-1}; green) peaks.

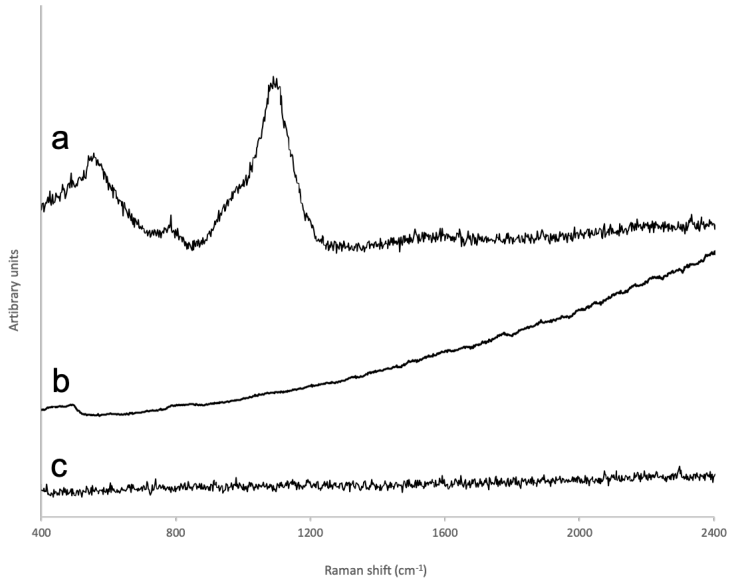

Figure 4-6. Deep-UV Raman spectra (uncorrected) of various materials, including glass microscope slide (a) and quartz-fused microscope slide (b), and the background spectrum of the charge-coupled device (CCD) detector of the Raman instrument used in this study (c).

REFERENCES

Abbey, W. J., Bhartia, R., Beegle, L. W., DeFlores, L., Paez, V., Sijapati, K., Williford, K., Tuite, M., Hug, W., & Reid, R. (2017). Deep UV Raman spectroscopy for planetary exploration: The search for in situ organics. *Icarus*, *290*, 201–214.

Alleon, J., Bernard, S., Le Guillou, C., Daval, D., Skouri-Panet, F., Pont, S., Beyssac, O., McKeegan, K., & Robert, F. (2016). Early entombment within silica minimizes the molecular degradation of microorganisms during advanced diagenesis. *Chemical Geology*, *437*, 98–108.

Allwood, A. C., Walter, M. R., & Marshall, C. P. (2006). Raman spectroscopy reveals thermal palaeoenvironments of c. 3.5 billion-year-old organic matter, *41*, 190–197.

Aoya, M., Kouketsu, Y., Endo, S., Shimizu, H., Mizukami, T., Nakamura, D., & Wallis, S. (2010). Extending the applicability of the Raman carbonaceous-material geothermometer using data from contact metamorphic rocks. *Journal of Metamorphic Geology*, *28*(9), 895–914.

Arvidson, R. E., Ruff, S. W., Morris, R. V., Ming, D. W., Crumpler, L. S., Yen, A. S., Squyres, S. W., Sullivan, R. J., Bell III, J. F., Cabrol, N. A., Clark, B. C., Farrand, W. H., Gellert, R., Greenberger, R., Grant, J. A., Guinness, E. A., Herkenhoff, K. E., Hurowitz, J. A., Johnson, J. R., Klingelhöfer, G., Lewis, K. W., Li, R., McCoy, T. J., Moersch, J., McSween, H. Y., Murchie, S. L., Schmidt, M., Schröder, C., Wang, A., Wiseman, S., Madsen, M. B., Goetz, W., & McLennan, S. M. (2008). Spirit Mars rover mission to the Columbia Hills, Gusev Crater: Mission overview

and selected results from the Cumberland Ridge to Home Plate. *Journal of Geophysical Research: Planets*, *113*(E12), 1–35.

Barańska, H., Łabudzińska, A., & Terpiński, J. (1987). *Laser Raman spectrometry: Analytical applications*. Ellis Horwood Ltd.

Bartley, J. K. (1996). Actualistic taphonomy of cyanobacteria; implications for the Precambrian fossil record. *Palaios*, *11*(6), 571–586.

Beegle, L., Bhartia, R., White, M., Deflores, L., Abbey, W., Wu, B. Y.-H., Fries, M., Burton, A., Edgett, K. S., Ravine, M. A., Hug, W., Reid, R., Nelson, T., Clegg, S., Wiens, R., Asher, S., & Sobron, P. (2015). SHERLOC: Scanning habitable environments with Raman & luminescence for organics & chemicals. *IEEE Aerospace Conference Proceedings*, *2015-June*.

Benner, S. A., Devine, K. G., Matveeva, L. N., & Powell, D. H. (2000). The missing organic molecules on Mars. *Proceedings of the National Academy of Sciences USA*, *97*(6), 2425–2430.

Beyssac, O., Goffé, B., Chopin, C., & Rouzaud, J. N. (2002). Raman spectra of carbonaceous material in metasediments: A new geothermometer. *Journal of Metamorphic Geology*, *20*(9), 859–871.

Beyssac, O., Brunet, F., Petitet, J., Goffé, B. & Rozaud, J.-N. (2003). Experimental study of the microtextural and structural transformations of carbonaceous materials under pressure and temperature. *European Journal of Mineralogy*, *15*, 937–951.

Bishop, J. L. (2018). Remote detection of phyllosilicates on Mars and implications for climate and habitability. In N. A. Cabrol & E. A. Grin (Eds.), *From habitability to life on Mars* (pp. 37-75). Elsevier.

Bower, D. M., Steele, a, Fries, M. D., & Kater, L. (2013). Micro Raman spectroscopy of carbonaceous material in microfossils and meteorites: improving a method for life detection. *Astrobiology*, *13*(1), 103–113.

Butterfield, N. J. (2015). Early evolution of the Eukaryota. *Palaeontology*, *58*(1), 5–17.

Casiraghi, C., Piazza, F., Ferrari, A. C., Grambole, D., & Robertson, J. (2005). Bonding in hydrogenated diamond-like carbon by Raman spectroscopy. *Diamond and Related Materials*, *14*(3–7), 1098–1102.

Cataldo, F., Keheyan, Y., & Baccaro, S. (2004). The effect of gamma-irradiation of anthracite coal and oil bitumen. *Journal of Radioanalytical and Nuclear Chemistry*, *262*, 443–450.

Court, R. W., Sephton, M. A., Parnell, J., & Gilmour, I. (2006). The alteration of organic matter in response to ionising irradiation: Chemical trends and implications for extraterrestrial sample analysis. *Geochimica et Cosmochimica Acta*, *70*(4), 1020–1039.

Court, R. W., Sephton, M. A., Parnell, J., & Gilmour, I. (2007). Raman spectroscopy of irradiated organic matter. *Geochimica et Cosmochimica Acta*, *71*(10), 2547–2568.

Cronin, J. R., Pizzarello, S., & Cruikshank, D. P. (1988). Organic matter in carbonaceous chondrites, planetary satellites, asteroids and comets. In J. F. Kerridge & M. S. Matthews (Eds.), *Meteorites and the early Solar System* (pp. 819-857). University of Arizona Press.

Cuesta, A., Dhamelincourt, P., Laureyns, J., Martinez-Alonso, A., & Tascón, J. D. (1994). Raman microprobe studies on carbon materials. *Carbon*, *32*(8), 1523–1532.

Czaja, A. D., Kudryavtsev, A. B., & Schopf, J. W. (2006). New method for the microscopic, nondestructive acquisition of ultraviolet resonance Raman spectra from plant cell walls. *Applied Spectroscopy*, *60*(4), 352–355.

Czaja, A. D., Kudryavtsev, A. B., Cody, G. D., & Schopf, J. W. (2009). Characterization of permineralized kerogen from an Eocene fossil fern. *Organic Geochemistry*, *40*(3), 353–364.

Czaja, A. D., Beukes, N. J., & Osterhout, J. T. (2016). Sulfur-oxidizing bacteria prior to the Great Oxidation Event from the 2.52 Ga Gamohaan Formation of South Africa. *Geology*, *44*(12), 983–986.

Dartnell, L. R., Storrie-Lombardi, M. C., Mullineaux, C. W., Ruban, A. V., Wright, G., Griffiths, A. D., Muller, J. P., & Ward, J. M. (2011). Degradation of cyanobacterial biosignatures by ionizing radiation. *Astrobiology*, *11*, 997–1016.

Dartnell, L. R., Page, K., Jorge-Villar, S. E., Wright, G., Munshi, T., Scowen, I. J., Ward, J. M., Edwards, H. G. (2012). Destruction of Raman biosignatures by ionizing radiation and the implications for life detection on Mars. *Analytical and Bioanalytical Chemistry*, *403*, 131–144.

Des Marais, D. J. (2010). Exploring Mars for evidence of habitable environments and life. *Proceedings of the American Philosophical Society*, *154*(4), 402–421.

Durand, B. (1980). *Kerogen: Insoluble organic matter from sedimentary rocks*. Editions Technip.

Ehlmann, B. L., & Edwards, C. S. (2014). Mineralogy of the Martian surface. *Annual Review of Earth and Planetary Sciences*, *42*(1), 291–315.

Ehlmann, B. L., Mustard, J. F., Fassett, C. I., Schon, S. C., Head III, J. W., Des Marais, D. J., Grant, J. A., & Murchie, S. L. (2008a). Clay minerals in delta deposits and organic preservation potential on Mars. *Nature Geoscience*, *1*(6), 355–358.

Ehlmann, B. L., Mustard, J. F., Murchie, S. L., Poulet, F., Bishop, J. L., Brown, A. J., Calvin, W. M., Clark, R. N., Des Marais, D. J., Milliken, R. E., Roach, L. H., Roush, T. L., Swayze, G. A., Wray, J. J. (2008b). Orbital identification of carbonate-bearing rocks on Mars. *Science*, *322*(5909), 1828–1832.

Ellery, A., & Wynn-Williams, D. (2003). Why Raman spectroscopy on Mars?—A case of the right tool for the right job. *Astrobiology*, *3*(3), 565–579.

Escribano, R., Sloan, J. J., Siddique, N., Sze, N., & Dudev, T. (2001). Raman spectroscopy of carbon-containing particles. *Vibrational Spectroscopy*, *26*(2), 179–186.

Farmer, J. D., & Des Marais, D. J. (1999). Exploring for a record of ancient Martian life. *Journal of Geophysical Research: Planets*, *104*(E11), 26977–26995.

Ferralis, N., Matys, E. D., Knoll, A. H., Hallmann, C., & Summons, R. E. (2016). Rapid, direct and non-destructive assessment of fossil organic matter via microRaman spectroscopy. *Carbon*, *108*, 440–449.

Ferrari, A. C., & Robertson, J. (2000). Interpretation of Raman spectra of disordered and amorphous carbon. *Physical Review B*, *61*, 95–107.

Ferrari, A. C., & Robertson, J. (2001). Resonant Raman spectroscopy of disordered, amorphous, and diamondlike carbon. *Physical Review B - Condensed Matter and Materials Physics*, *64*(7), 1–13.

Ferrari, A. C., & Robertson, J. (2004). Raman spectroscopy of amorphous, nanostructured, diamond-like carbon, and nanodiamond. *Philosophical Transactions of the Royal Society A: Mathematical, Physical and Engineering Sciences*, *362*(1824), 2477–2512.

Flannery, D. T., Allwood, A. C., Summons, R. E., Williford, K. H., Abbey, W., Matys, E. D., & Ferralis, N. (2018). Spatially-resolved isotopic study of carbon trapped in ~3.43 Ga Strelley Pool Formation stromatolites. *Geochimica et Cosmochimica Acta*, *223*, 21–35.

Foucher, F., Ammar, M. R., & Westall, F. (2015). Revealing the biotic origin of silicified Precambrian carbonaceous microstructures using Raman spectroscopic mapping, a potential method for the detection of microfossils on Mars. *Journal of Raman Spectroscopy*, *46*(10), 873–879.

Goudge, T. A., Milliken, R. E., Head, J. W., Mustard, J. F., & Fassett, C. I. (2017). Sedimentological evidence for a deltaic origin of the western fan deposit in Jezero crater, Mars and implications for future exploration. *Earth and Planetary Science Letters*, 458, 357–365.

Grant, J. A., Golombek, M. P., Wilson, S. A., Farley, K. A., Williford, K. H., & Chen, A. (2018). The science process for selecting the landing site for the 2020 Mars rover. *Planetary and Space Science*, *164*, 106–126.

Grotzinger, J. P., & Milliken, R. E. (2012). The sedimentary rock record of Mars: Distribution, origins, and global stratigraphy. *Sedimentary Geology of Mars*, *102*, 1–48.

Grotzinger, J. P., Sumner, D. Y., Kah, L. C., Stack, K., Gupta, S., Edgar, L., Rubin, D., Lewis, K., Schieber, J., Mangold, N., Milliken, R., Conrad, P. G., DesMarais, D., Farmer, J., Siebach, K., Calef, F., Hurowitz, J., McLennan, S. M., Ming, D., Vaniman, D., Crisp, J., Vasavada, A., Edgett, K. S., Malin, M., Blake, D., Gellert, R., Mahaffy, P., Wiens, R. C., Maurice, S., Grant, J. A., Wilson, S., Anderson, R. C., Beegle, L., Arvidson, R., Hallet, B., Sletten, R. S., Rice, M., Bell, J., Griffes, J., Ehlmann, B., Anderson, R. B., Bristow, T. F., Dietrich, W. E., Dromart, G., Eigenbrode, J., Fraeman, A., Hardgrove, C., Herkenhoff, K., Jandura, L., Kocurek, G., Lee, S., Leshin, L. A., Leveille, R., Limonadi, D., Maki, J., McCloskey, S., Meyer, M., Minitti, M., Newsom, H., Oehler, D., Okon, A., Palucis, M., Parker, T., Rowland, S., Schmidt, M., Squyres, S., Steele, A., Stolper, E., Summons, R., Treiman, A., Williams, R., & Yingst, A. (2014). A habitable fluvio-lacustrine environment at Yellowknife Bay, Gale crater, Mars. *Science*, *343*(6169), 1242777.

Hays, L. E., Graham, H. V., Des Marais, D. J., Hausrath, E. M., Horgan, B., McCollom, T. M., Parenteau, M. N., Potter-McIntyre, S. L., Williams, A. J., & Lynch, K. L. (2017). Biosignature Preservation and Detection in Mars Analog Environments. *Astrobiology*, *17*(4), 363–400.

Henry, D. G., Jarvis, I., Gillmore, G., Stephenson, M., & Emmings, J. F. (2018). Assessing low-maturity organic matter in shales using Raman spectroscopy: Effects of sample preparation and operating procedure. *International Journal of Coal Geology*, *191*(February), 135–151.

Henry, D. G., Jarvis, I., Gillmore, G., & Stephenson, M. (2019). Raman spectroscopy as a tool to determine the thermal maturity of organic matter: Application to sedimentary, metamorphic and structural geology. *Earth-Science Reviews*, *198*(August), 102936.

Holland, H. D. (1984). *The chemical evolution of the atmosphere and oceans*. Princeton University Press.

Horgan, B. H., Anderson, R. B., Dromart, G., Amador, E. S., & Rice, M. S. (2020). The mineral diversity of Jezero crater: Evidence for possible lacustrine carbonates on Mars. *Icarus*, *339*, 113526.

Javaux, E. J. (2007). The early eukaryotic fossil record. *Advances in Experimental Medicine and Biology*, *607*, 1–19.

Jawhari, T., Roid, A., & Casado, J. (1995). Raman spectroscopic characterization of some commercially available carbon black materials. *Carbon*, *33*(11), 1561–1565.

Kanavarioti, A., & Mancinelli, R. L. (1990). Could organic matter have been preserved on Mars for 3.5 billion years?. *Icarus*, *84*(1), 196–202.

Knoll, A. H. (2012). The fossil record of microbial life. In A. H. Knoll, D. E. Canfield, & K. O. Konhauser (Eds.), *Fundamentals of geobiology* (pp. 297-314). Wiley-Blackwell.

Kouketsu, Y., Mizukami, T., Mori, H., Endo, S., Aoya, M., Hara, H., Nakamura, D., & Wallis, S. (2014). A new approach to develop the Raman carbonaceous material geothermometer for low-grade metamorphism using peak width. *Island Arc*, *23*(1), 33–50.

Kremer, B., Kazmierczak, J., Łukomska-Kowalczyk, M., & Kempe, S. (2012). Calcification and Silicification: Fossilization Potential of Cyanobacteria from Stromatolites of Niuafo'ou's Caldera Lakes (Tonga) and Implications for the Early Fossil Record. *Astrobiology*, *12*(6), 535–548.

Kudryavtsev, A. B., Schopf, J. W., Agresti, D. G., & Wdowiak, T. J. (2001). In situ laser-Raman imagery of precambrian microscopic fossils. *Proceedings of the National Academy of Sciences USA*, *98*(3), 823–826.

Lamb D. M., Awramik S. M., Chapman D. J., Zhu S. (2009). Evidence for eukaryotic diversification in the ~1800 million-year-old Changzhougou Formation, North China. *Precambrian Research*, *173*, 93–104.

Mangold, N., Dromart, G., Ansan, V., Salese, F., Kleinhans, M. G., Massé, M., Quantin-Nataf, C. & Stack, K. M. (2020). Fluvial regimes, morphometry, and age of Jezero crater paleolake inlet

valleys and their exobiological significance for the 2020 Rover Mission Landing Site. *Astrobiology*, 20(8), 994–1013.

Manning-Berg, A., Wood, R., Williford, K., Czaja, A., & Kah, L. (2019). The taphonomy of Proterozoic microbial mats and implications for early diagenetic silicification. *Geosciences*, *9*(40), 1–31.

Mapelli, C., Castiglioni, C., Zerbi, G., & Müllen, K. (1999). Common force field for graphite and polycyclic aromatic hydrocarbons. *Physical Review B, 60*, 12710–12725.

Marshall, C. P., Love, G. D., Snape, C. E., Hill, A. C., Allwood, A. C., Walter, M. R., Van Kranendonk, M. J., Bowden, S. A., Sylva, S. P., & Summons, R. E. (2007). Structural characterization of kerogen in 3.4 Ga Archaean cherts from the Pilbara Craton, Western Australia. *Precambrian Research*, *155*(1–2), 1–23.

Marshall, C. P., Edwards, H. G. M., & Jehlicka, J. (2010). Understanding the application of Raman spectroscopy to the detection of traces of life. *Astrobiology*, *10*, 229–243.

Matthews, M. J., Pimenta, M. A., Dresselhaus, G., Dresselhaus, M. S., & Endo, M. (1999). Origin of dispersive effects of the Raman D-band in disordered carbon materials. *Physical Review B*, *59*(10), R6585.

McKirdy, D. M., & Hahn, J. H. (1982). The composition of kerogen and hydrocarbons in Precambrian rocks. In H. D. Holland & M. Schidlowski (Eds.), *Mineral Deposits and the Evolution of the Biosphere* (pp. 123-154). Springer.

McMahon, S., Bosak, T., Grotzinger, J. P., Milliken, R. E., Summons, R. E., Daye, M., Newman, S. A., Fraeman, A., Williford, K. H., & Briggs, D. E. G. (2018). A Field Guide to Finding Fossils on Mars. *Journal of Geophysical Research: Planets*, *123*(5), 1012–1040.

Mustard, J. F., Murchie, S. L., Pelkey, S. M., Ehlmann, B. L., Milliken, R. E., Grant, J. A., Bibring, J.-P., Poulet, F., Bishop, J., Noe Dobrea, E., Roach, L., Seelos, F., Arvidson, R. E., Wiseman, S., Green, R., Hash, C., Humm, D., Malaret, E., McGovern, J. A., Seelos, K., Clancy, T., Clark, R., Des Marais, D., Izenberg, N., Knudson, A., Langevin, Y., Martin, T., McGuire, P., Morris, R., Robinson, M., Roush, T., Smith, M., Swayze, G., Taylor, H., Titus, T., & Wolff, M. (2008). Hydrated silicate minerals on Mars observed by the Mars Reconnaissance Orbiter CRISM instrument. *Nature*, *454*(7202), 305–309.

Mustard, J., Adler, M., Allwood, A., Bass, D., Beaty, D., Bell, J., Brinckerhoff, W. B., Carr, M., Des Marais, D. J., Drake, B., Edgett, K. S., Eigenbrode, J., Elkins-Tanton, L. T., Grant, J. A., Milkovich, S. M., Ming, D., Moore, C., Murchie, S., Onstott, T. C., Ruff, S. W., Sephton, M. A., Steele, A., & Treiman A. (2013). Report of the Mars 2020 Science Definition Team. *Mars Exploration Program Analysis Group (MEPAG)*, (Cl), 155–205.

Nemanich, R. J., & Solin, S. A. (1979). First- and second- order Raman scattering from finite-size crystals of graphite. *Physical Review B*, *20*, 392–401.

Oehler, J. H. (1976). Experimental studies in Precambrian paleontology: Structural and chemical changes in blue-green algae during simulated fossilization in synthetic chert. *Bulletin of the Geological Society of America*, *87*(1), 117–129.

Oehler, J. H., & Schopf, J. W. (1971). Artificial microfossils: experimental studies of permineralization of blue-green algae in silica. *Science*, *174*(4015), 1229–1231.

Oehler, D., & Cady, S. (2014). Biogenicity and Syngeneity of Organic Matter in Ancient Sedimentary Rocks: Recent Advances in the Search for Evidence of Past Life. *Challenges*, *5*(2), 260–283.

Osterhout, J. T., Czaja, A. D., Bartley, J. K., & Fralick, P. W. (2019). Preservation of carbon isotopes in kerogen from thermally altered Mesoproterozoic lacustrine microbialites. *Canadian Journal of Earth Sciences*, *56*(10), 1017–1026.

Pasteris, J. D., & Wopenka, B. (1991). Raman spectra of graphite as indicates of degree of metamorphism. *Canadian Mineralogist*, *29*, 1–9.

Pasteris, J. D., & Wopenka, B. (2003). Necessary, but not sufficient: Raman identification of disordered carbon as a signature of ancient life. *Astrobiology*, *3*(4), 727–738.

Pavlov, A. A., Vasilyev, G., Ostryakov, V. M., Pavlov, A. K., & Mahaffy, P. (2012). Degradation of the organic molecules in the shallow subsurface of Mars due to irradiation by cosmic rays. *Geophysical Research Letters*, *39*, 1–5.

Perry, E. C., & Lefticariu, L. (2013). Formation and geochemistry of Precambrian cherts. In H. D. Holland & K. K. Turekian (Eds.), *Treatise on geochemistry: Second edition* (9th ed., Vol. 9). Elsevier.

Pizzarello, S., & Shock, E. (2010). The organic composition of carbonaceous meteorites: the evolutionary story ahead of biochemistry. *Cold Spring Harbor Perspectives in Biology*, *2*, 1–19.

Robertson, J. (1986). Amorphous carbon. *Advances in Physics*, *35*(4), 317–374.

Sato, K., Saito, R., Oyama, Y., Jiang, J., Cancado, L. G., Pimenta, M. A., Jorio, A., Samsonidze, Ge. G., Dresselhaus, G., & Dresselhaus, M. S. (2006). D-band Raman intensity of graphitic materials as a function of laser energy and crystallite size. *Chemical Physics Letters*, *427*(1-3), 117–121.

Schidlowski, M. (2001). Carbon isotopes as biogeochemical recorders of life over 3.8 Ga of Earth history: evolution of a concept. *Precambrian Research*, *106*(1–2), 117–134.

Schopf, J. W. (2006). Fossil evidence of Archaean life. *Philosophical Transactions of the Royal Society B: Biological Sciences*, *361*(1470), 869–885.

Schopf, J. W., & Kudryavtsev, A. B. (2005). Three-dimensional Raman imagery of precambrian microscopic organisms. *Geobiology*, *3*(1), 1–12.

Schopf, J. W., & Kudryavtsev, A. B. (2009). Confocal laser scanning microscopy and Raman imagery of ancient microscopic fossils. *Precambrian Research*, *173*(1–4), 39–49.

Schopf, J. W., Kudryavtsev, A. B., Agresti, D. G., Wdowiak, T. J., & Czaja, A. D. (2002). Laser-Raman imagery of Earth's earliest fossils. *Nature*, *416*, 73–76.

Schopf, J. W., Kudryavtsev, A. B., Agresti, D. G., Czaja, A. D., & Wdowiak, T. J. (2005). Raman imagery: a new approach to assess the geochemical maturity and biogenicity of permineralized Precambrian fossils. *Astrobiology*, *5*(3), 333–371.

Schopf, J. W., Farmer, J. D., Foster, I. S., Kudryavtsev, A. B., Gallardo, V. A., & Espinoza, C. (2012). Gypsum-permineralized microfossils and their relevance to the search for life on Mars. *Astrobiology*, *12*(7), 619–633.

Shkolyar, S., Eshelman, E. J., Farmer, J. D., Hamilton, D., Daly, M. G., & Youngbull, C. (2018). Detecting kerogen as a biosignature using colocated UV time-gated Raman and fluorescence spectroscopy. *Astrobiology*, *18*(4), 431–453.

Song, J. J., Chung, D. D. L., Eklund, P. C., & Dresselhaus, M. S. (1976). Raman scattering in graphite intercalation compounds. *Solid State Communications*, *20*, 1111–1115.

Stoker, C. R., Zent, A., Catling, D. C., Douglas, S., Marshall, J. R., Archer Jr., D., Clark, B., Kounaves, S. P., Lemmon, M. T., Quinn, R., Renno, N., Smith, P. H., & Young, S. M. M. (2010). Habitability of the Phoenix landing site. *Journal of Geophysical Research: Planets*, *115*(E6), 1–24.

Sugitani, K., Grey, K., Allwood, A., Nagaoka, T., Mimura, K., Minami, M., Marshall, C. P., Van Kranendonk, M. J., Walter, M. R. (2007). Diverse microstructures from Archaean chert from the Mount Goldsworthy-Mount Grant area, Pilbara Craton, Western Australia: Microfossils, dubiofossils, or pseudofossils? *Precambrian Research*, *158*(3–4), 228–262.

Summons, R. E., Amend, J. P., Bish, D., Buick, R., Cody, G. D., Des Marais, D. J., Dromart, G., Eigenbrode, J. L., Knoll, A. H., & Sumner, D. Y. (2011). Preservation of Martian organic and environmental records: Final report of the Mars biosignature working group. *Astrobiology*, *11*(2), 157–181.

Tarcea, N., Harz, M., Rösch, P., Frosch, T., Schmitt, M., Thiele, H., Hochleitner, R., & Popp, J. (2007). UV Raman spectroscopy—a technique for biological and mineralogical in situ planetary studies. *Spectrochimica Acta Part A: Molecular and Biomolecular Spectroscopy*, *68*(4), 1029–1035.

Tarnas, J. D., Mustard, J. F., Lin, H., Goudge, T. A., Amador, E. S., Bramble, M. S., Kremer, C. H., Zhang, X., Itoh, Y. & Parente, M. (2019). Orbital identification of hydrated silica in Jezero crater, Mars. *Geophysical Research Letters*, *46*(22), 12771–12782.

Tuinstra, F., & Koenig, J. L. (1970). Raman spectrum of graphite. *Journal of Chemical Physics*, *53*, 1126–1130.

Vandenbroucke, M., & Largeau, C. (2007). Kerogen origin, evolution and structure. *Organic Geochemistry*, *38*(5), 719–833.

Vidano, R. P., Fischbach, D. B., Willis, L. J., & Loehr, T. M. (1981). Observation of Raman band shifting with excitation wavelength for carbons and graphites. *Solid State Communications*, *39*(2), 341–344.

Wada, H., & Suzuki, K. (1983). Carbon isotopic thermometry calibrated by dolomite-calcite solvus temperatures. *Geochimica et Cosmochimica Acta*, *47*(4), 697–706.

Walter, M. R., & Des Marais, D. J. (1993). Preservation of biological information in thermal spring deposits: developing a strategy for the search for fossil life on Mars. *Icarus*, *101*(1), 129–143.

Wang, Y., Alsmeyer, D. C., & McCreery, R. L. (1990). Raman spectroscopy of carbon materials: Structural basis of observed spectra. *Chemistry of Materials*, 2, 557–563.

Westall, F. (1999). The nature of fossil bacteria: a guide to the search for extraterrestrial life. *Journal of Geophysical Research: Planets*, *104*(E7), 16437–16451.

Westall, F., Foucher, F., Bost, N., Bertrand, M., Loizeau, D., Vago, J. L., Kminek, G., Gaboyer, F., Campbell, K. A., Bréhéret, J.-G., Gautret, P., Cockell, C. S. (2015). Biosignatures on Mars: what, where, and how? Implications for the search for Martian life. *Astrobiology*, *15*(11), 998–1029.

Williford, K. H., Farley, K. A., Stack, K. M., Allwood, A. C., Beaty, D., Beegle, L. W., Bhartia, R., Brown, A. J., Juarez, M. T., Hamran, S. E., Hecht, M. H., Hurowitz, J. A., Rodriguez-Manfredi, J. A., Maurice, S., Milkovich, S., & Wiens, R. C. (2018). The NASA Mars 2020 Rover Mission and the Search for Extraterrestrial Life. In N. A. Cabrol & E. A. Grin (Eds.), *From habitability to life on Mars* (pp. 275-308). Elsevier.

Wopenka, B., & Pasteris, J. D. (1993). Structural characterization of kerogens to granulite-facies graphite: applicability of Raman microprobe spectroscopy. *American Mineralogist*, *78*(5-6), 533–557.

Zhang, Z. (1997). A new Palaeoproterozoic clastic-facies microbiota from the Changzhougou Formation, Changcheng Group Jixian, north China. *Geological Magazine*, *134*(2), 145–150.

Chapter 5

Conclusions

Taken collectively, the studies which comprise this dissertation serve to advance knowledge in the fields of Precambrian paleobiology, organic and stable isotope geochemistry, and astrobiology. In terms of the search for ancient biosignatures on Earth, this research has expanded our understanding of microfossil preservation, and more specifically, the documentation of changes in geochemical signatures as revealed by Raman spectroscopy and secondary ion mass spectrometry (SIMS). Analyses of Precambrian microfossils and associated detrital kerogen from several distinct shallow-marine chert deposits have provided firm data by which to compare and evaluate the morphology, molecular structure, and isotopic composition of samples from units of varying thermal maturities. The findings reported here have thus contributed to the further development of these techniques for studying Earth's early fossil record, and have also revealed new insights into the modern search for evidence of past microbial life on Mars.

The results of this research have provided at least three new valuable insights: 1) that $\delta^{13}C_{org}$ values of kerogenous Precambrian microfossils may be similarly preserved (i.e., indistinguishable to a few ‰) among morphologically-defined fossil taxa from slightly differing depositional environments (e.g., stromatolites, pisolites) and separated in age by >500 Ma; 2) the preservation of $\delta^{13}C_{org}$ values among permineralized (silicified) kerogenous microfossils appears to be well constrained for cherts experiencing lower greenschist facies metamorphism (~200–350 °C), but there is some evidence suggesting that the onset of thermal alteration of such $\delta^{13}C_{org}$ values may begin as early as mid- to upper-greenschist facies (~300–400 °C); and, 3) the documentation of deep-UV Raman spectra for kerogenous microfossils of varying thermal maturities, and the application of these findings to the search for fossil kerogen on Mars by the

Perseverance rover, which will also cache those samples containing promising paleobiological signatures such as kerogen for future sample return to Earth.

New questions will undoubtedly arise as SIMS and Raman analyses of biogenic kerogen are further investigated. Such studies will require comparisons of isotopic and Raman spectroscopic data, including the values and spectra detailed here, with those from analyses of carbonaceous samples having differing physical and chemical compositions, including older and/or more altered Archean chert samples, organic-rich sedimentary rocks of varying lithologies (e.g., shales, carbonates, evaporites, etc.) and thermal alteration regimes (Osterhout et al., 2019), and those derived from analyses of carbonaceous materials of established abiotic origin (i.e., "negative controls") such as the kerogen-like components (abiotic macromolecular carbon) of carbonaceous chondrites or in meteorites from Mars (e.g., Steele et al., 2012, 2016), specimens which are currently available for such analyses. Additional studies of variably altered Precambrian kerogens would also provide a more robust quantitative dataset for the potential establishment of a deep-UV Raman-based geothermometer. In addition to this research, previous studies have demonstrated that the resonance-enhanced Raman signatures of kerogen are still detectable in some relatively highly altered lithologies, such as ancient carbonates (Shkolyar et al., 2018) and potentially microfossiliferous gypsum deposits (Schopf et al., 2012). Such samples represent promising targets for future deep-UV Raman spectroscopy measurements.

Ultimately, it is my hope that the research presented in this dissertation is of value to current and future scholars, scientists, and students who express shared interest in these subjects. The ambitious pursuit of new knowledge in studies of early life on Earth, and of understanding the potential for life on Mars, is a lasting and profound endeavor for which I am forever grateful to have contributed an incremental but dedicated effort.

REFERENCES

Osterhout, J. T., Czaja, A. D., Bartley, J. K., & Fralick, P. W. (2019). Preservation of carbon isotopes in kerogen from thermally altered Mesoproterozoic lacustrine microbialites. *Canadian Journal of Earth Sciences*, *56*(10), 1017–1026.

Schopf, J. W., Farmer, J. D., Foster, I. S., Kudryavtsev, A. B., Gallardo, V. A., & Espinoza, C. (2012). Gypsum-permineralized microfossils and their relevance to the search for life on Mars. *Astrobiology*, *12*(7), 619–633.

Shkolyar, S., Eshelman, E. J., Farmer, J. D., Hamilton, D., Daly, M. G., & Youngbull, C. (2018). Detecting kerogen as a biosignature using colocated UV time-gated Raman and fluorescence spectroscopy. *Astrobiology*, *18*(4), 431–453.

Steele, A., McCubbin, F. M., Fries, M., Kater, L., Boctor, N. Z., Fogel, M. L., Conrad, P. G., Glamoclija, M., Spencer, M., Morrow, A. L., Hammond, M. R., Zare, R. N., Vicenzi, E. P., Siljeström, S., Bowden, R., Herd, C. D. K., Mysen, B. O., Shirey, S. B., Amundsen, H. E. F., Treiman, A. H., Bullock, E. S., & Jull, A. J. T. (2012). A reduced organic carbon component in martian basalts. *Science*, *337*(6091), 212–215.

Steele, A., McCubbin, F. M., & Fries, M. D. (2016). The provenance, formation, and implications of reduced carbon phases in Martian meteorites. *Meteoritics and Planetary Science*, *51*(11), 2203–2225.